



**UNIVERSIDAD NACIONAL AUTÓNOMA DE MÉXICO**  
**POSGRADO EN CIENCIA E INGENIERÍA DE MATERIALES**  
**INSTITUTO DE INVESTIGACIONES EN MATERIALES**

**POST-SYNTHESIS MODIFICATION OF  
HEXACYANOCOBALTATES WITH OZONE**

**THESIS**

IN ORDER TO OBTAIN THE DEGREE OF:  
DOCTORADO EN CIENCIA E INGENIERIA DE MATERIALES

**PRESENTER**

M.Sc. María Laura Ríos Gómez

**SUPERVISOR**

Dr. Jorge Balmaseda Era  
Instituto de Investigaciones en Materiales

**TUTOR COMMITTEE**

Dr. Luis Felipe Del Castillo Dávila  
Instituto de Investigaciones en Materiales

Dra. María del Pilar Carreón Castro  
Instituto de Ciencias Nucleares

Ciudad Universitaria, Cd. Mx. Agosto 2017



Universidad Nacional  
Autónoma de México

Dirección General de Bibliotecas de la UNAM

**Biblioteca Central**



**UNAM – Dirección General de Bibliotecas**  
**Tesis Digitales**  
**Restricciones de uso**

**DERECHOS RESERVADOS ©**  
**PROHIBIDA SU REPRODUCCIÓN TOTAL O PARCIAL**

Todo el material contenido en esta tesis esta protegido por la Ley Federal del Derecho de Autor (LFDA) de los Estados Unidos Mexicanos (México).

El uso de imágenes, fragmentos de videos, y demás material que sea objeto de protección de los derechos de autor, será exclusivamente para fines educativos e informativos y deberá citar la fuente donde la obtuvo mencionando el autor o autores. Cualquier uso distinto como el lucro, reproducción, edición o modificación, será perseguido y sancionado por el respectivo titular de los Derechos de Autor.



## **JURY ASSIGNED**

**President:** Dr. Vojtech Jancik

**First Vocal:** Dr. Jorge Balmaseda Era

**Second Vocal:** Dr. Juan Carlos Ruiz Bucio

**Third Vocal:** Dr. Alfonso Ramón García Márquez

**Secretary:** Dr. Argel Ilich Ibarra Alvarado

## **PLACE WERE THE THESIS WAS CONDUCTED**

Instituto de Investigaciones en Materiales  
Universidad Nacional Autónoma de México

---

Dr. Jorge Balmaseda Era  
Thesis Supervisor

# Acknowledgements

To all the people that made this work possible:

1. To my husband Ariel for his emotional support and continuous criticism towards my work.
2. To my sister Mariana for her unconditional support and her never ending faith in me, that kept me going when I needed most.
3. To my best friend Majo, for listening to me with patience and affection, for her help with frequent and keen advices and for her company, of course.
4. To my mum for her continuous care about both my physical and emotional health.
5. To my supervisor...for far too many things.
6. To Jaquebet, for her affection and help at work.
7. To Arkadiy Simonov, Joshua Hill, Amber L. Thomson, Lázaro Huerta Arcos and Karla Eriseth Reyes Morales; for their help with the experimental work.
8. To the CONACyT scholarship and to the projects: DGAPA IG-100315, CONACYT 250848 and CIQA (intern project 6317).

This work was presented at the following conferences:

1. Séptimo congreso Nacional de la Sociedad Mexicana de Cristalografía/ July 4<sup>th</sup>-8<sup>th</sup> of 2014 in Villa Hermosa, Tabasco. México. Effect of ozone treatment in structure and stability of porous cobaltcyanides.
2. The 6 International FEZA Conference/ September 8<sup>th</sup>-11<sup>th</sup> of 2014 in Leipzig, Germany. Title: “Effect of ozone treatment in fuel gas adsorption of porous transition metal hexacyanides”.
3. ISIS Crystallography User Group Meeting PCG-SCMP Winter Meeting/ October 19<sup>th</sup>-20<sup>th</sup> of 2015 in Abingdom, England. “Effect of oxidation on structure and stability of porous transition metal hexacyanides”.

## This work is dedicated to:

All the people I care for. To my granddad Otto, for being the source of my inspiration. To all the people that can be eventually benefit with a cleaner and better life derived from this work.

*“One thing I have learned in a long life: that all our science, measured against reality, is primitive and childlike and yet, the most precious thing we have.”*

---

*Albert Einstein*

# Contents

<b>Acknowledgements</b>	<b>I</b>
<b>List of figures</b>	<b>VIII</b>
<b>List of tables</b>	<b>X</b>
<b>Abstract</b>	<b>XI</b>
<b>Introduction</b>	<b>1</b>
<b>I State of the art</b>	<b>5</b>
<b>1 Background</b>	<b>6</b>
1.1 Average <i>vs.</i> local structure in crystallography . . . . .	6
1.2 Thermal expansion of crystals . . . . .	10
1.3 Structure of transition metals hexacyanometallates . . . . .	12
1.3.1 Review of MnHCC and CoHCC structures . . . . .	16
1.4 Hydrogen and carbon dioxide adsorption in porous materials .	18
1.4.1 Interaction of H <sub>2</sub> and CO <sub>2</sub> with porous solids . . . . .	18
1.4.2 Adsorption applications in hexacyanocobaltates . . . . .	21
1.5 Reactions of ozone with transition metals . . . . .	22
1.5.1 Physical and chemical properties of ozone molecule . .	22
1.5.2 Ozone as oxidizing agent . . . . .	24
1.6 Post-synthesis modification of hexacyanometallates with ozone.	24
1.6.1 Oxidation of ferrocyanides . . . . .	24
1.6.2 Ozonization of Mn and Co ferricyanides . . . . .	27
1.7 X-ray photoelectron spectroscopy (XPS) analysis . . . . .	28
1.7.1 Basic physical principles . . . . .	29

1.7.2	Qualitative analysis of the XPS spectra . . . . .	30
1.7.3	Quantitative analysis of XPS spectra . . . . .	37
<b>II</b>	<b>Methodology</b>	<b>38</b>
<b>2</b>	<b>Materials and Methods</b>	<b>39</b>
2.1	Synthesis . . . . .	39
2.2	Post-synthesis modification . . . . .	41
2.3	Structural characterization . . . . .	43
2.4	Adsorption . . . . .	47
<b>III</b>	<b>Results</b>	<b>49</b>
<b>3</b>	<b>Structural analysis of Manganese Hexacyanocobaltate</b>	<b>50</b>
3.1	Thermal Expansion Coefficient of MnHCC . . . . .	51
3.1.1	Problem definition . . . . .	51
3.1.2	Thermodynamic formulation . . . . .	51
3.1.3	Linear thermal expansion coefficient calculations . . . . .	54
3.2	Local structure observations: Diffuse scattering . . . . .	64
<b>4</b>	<b>Langmuir-Freundlich Adsorption Model</b>	<b>70</b>
4.1	About the need for this model . . . . .	70
4.2	Langmuir-Freundlich isotherm . . . . .	71
4.3	Temperature dependence of parameter $g$ . . . . .	74
4.4	Temperature dependence of parameter $p_{1/2}$ . . . . .	75
4.5	Molar enthalpy of adsorption . . . . .	75
<b>5</b>	<b>Post-synthesis modification</b>	<b>77</b>
5.1	Infrared and Raman spectroscopy . . . . .	78
5.2	X-ray diffraction . . . . .	81
5.3	Thermogravimetric analysis . . . . .	83
5.4	Gas adsorption . . . . .	85
<b>6</b>	<b>X-ray photoelectron spectroscopy</b>	<b>90</b>
6.1	Elemental composition . . . . .	91
6.2	MnHCC as-synthesized and ozonized . . . . .	91
6.3	CoHCC as-synthesized and ozonized samples . . . . .	96

<b>Conclusions</b>	<b>100</b>
<b>Bibliography</b>	<b>102</b>
<b>Appendix</b>	<b>119</b>
<b>A MnHCC Single Crystals Diffraction</b>	<b>120</b>
<b>B Post-synthesis modification with ozone</b>	<b>124</b>
B.1 FTIR spectra of samples . . . . .	125
B.2 Raman spectra of samples . . . . .	127
B.3 X-ray diffraction powder patterns of samples . . . . .	128
B.4 Hydrogen and carbon dioxide adsorption . . . . .	129
B.5 Thermogravimetric analysis . . . . .	131
<b>C Photoelectron spectroscopy</b>	<b>139</b>

# List of Figures

1.1	Correlated disorder in crystal water . . . . .	8
1.2	Spatial arrangement of atoms for hexacyanides. . . . .	13
1.3	Structure of CuHCC ( $Pm\bar{3}m$ , ordered vacancies). . . . .	14
1.4	Structure of MnHCC ( $Fm\bar{3}m$ , disordered vacancies). . . . .	15
1.5	Canonical forms of ozone molecule . . . . .	22
2.1	General experimental strategy . . . . .	40
2.2	SC synthesis methods . . . . .	41
2.3	Experimental set-up for ozonization . . . . .	42
2.4	Cell parameter <i>vs.</i> temperature in MnHCC . . . . .	48
3.1	Plotting $\ln V$ <i>vs.</i> T on MnHCC single crystals . . . . .	57
3.2	MnHCC semidehydrated state. . . . .	60
3.3	X-ray diffraction patterns of MnHCC single crystals . . . . .	65
3.4	Monte Carlo simulations for diffuse scattering in MnHCC single crystals . . . . .	68
5.1	Ozone concentration <i>vs.</i> time for MnHCC . . . . .	77
5.2	FTIR spectra for MnHCC and CoHCC samples . . . . .	79
5.3	Differential correlation function for MnHCC and CoHCC samples . . . . .	82
5.4	Thermogravimetric curves of MnHCC samples . . . . .	84
5.5	Thermogravimetric curves of CoHCC samples . . . . .	84
5.6	Calculated isosteric heat of adsorption for all samples. . . . .	87
5.7	FTIR $\nu_{CN}$ bands of CoHCC . . . . .	88
6.1	Valence band for MnHCC . . . . .	92
6.2	Total and partial DOS plot for MnHCC and CoHCC . . . . .	93
6.3	XPS spectra for MnHCC . . . . .	95
6.4	XPS spectra for CoHCC . . . . .	97

A.1	Different fittings for $d\ln(V)/dT$ . . . . .	123
B.1	Section of the $\nu_{CN}$ bands of the CuHCC FTIR spectra. . . . .	125
B.2	FTIR spectra of MnHCC and CoHCC . . . . .	126
B.3	Full Raman spectra of MnHCC and CoHCC samples . . . . .	127
B.4	X-ray diffraction of MnHCC and CoHCC. . . . .	128
B.5	Adsorption isotherms of H <sub>2</sub> at 77 K and CO <sub>2</sub> at 273.15 K. . . . .	129
B.6	Langmuir–Freundlich isotherm fit to experimental isotherms. . . . .	130
B.7	TGA curves for as-synthesized MnHCC and CoHCC. . . . .	133
B.8	TGA experimental curves for MnHCC original and ozonized. . . . .	135
B.9	TGA experimental curves for CoHCC original and ozonized. . . . .	137
B.10	TGA for MnHCCOz and CoHCCOz, saturated with methanol. . . . .	138
C.1	XPS spectra for K <sub>3</sub> [Co(CN) <sub>6</sub> ] . . . . .	139
C.2	XPS spectra for MnHCC and CoHCC . . . . .	140
C.3	The XPS deconvolution for Mn 2p and O 2p core levels. . . . .	142
C.4	The XPS deconvolution for Co 2p core levels. . . . .	143
C.5	The XPS deconvolution for C 1s core levels. . . . .	144
C.6	The XPS deconvolution for N 1s core levels. . . . .	145

# List of Tables

1.1	Redox potentials for transition metal cations . . . . .	25
1.2	Mn chemical state identification: Multiplet splitting . . . . .	34
1.3	Co chemical state identification: Multiplet splitting . . . . .	36
3.1	Experimental data SCD . . . . .	55
3.2	Linear fitting slopes . . . . .	56
3.3	Interpolation results. . . . .	58
5.1	Observed Raman modes for original and ozonized MnHCC. . .	81
5.2	H <sub>2</sub> and CO <sub>2</sub> volumetric changes and cell parameters for MnHCC.	83
5.3	H <sub>2</sub> and CO <sub>2</sub> adsorption data for all samples . . . . .	87
6.1	Binding Energies . . . . .	94
6.2	Binding Energies . . . . .	98
A.1	Experimental data SC X-ray diffraction . . . . .	121
A.2	Fittings for lnV <i>vs.</i> T in MnHCC SC . . . . .	122
B.1	Molar mass of decomposition reaction components . . . . .	132
C.1	Elemental composition . . . . .	141

# Abstract

Transition metal hexacyanocobaltates are porous materials with open metal sites and a wide variety of pores. In this work, manganese(II) and cobalt(II) hexacyanocobaltates(III) have been selected to explore the interactions between the open metal sites located in their pores and guest molecules: hydrogen, carbon dioxide, water and methanol. An experimental setup was designed and implemented to conduct post-synthesis modification of the solids with ozone. Samples were dehydrated, ozonized and saturated with methanol in situ. Ozone molecules acted on the open metal sites changing their oxidation state, causing a contraction of the unit cell, and inducing a stronger interaction of the molecules of water and methanol with the lattice. This strengthening prevented the lattice from being evacuated without compromising its framework stability. The decomposition temperature decreased in all ozonized samples as a consequence of the elongation and weakening of the cobalt-carbon bond. Active Infrared and Raman bands were used to monitor the interaction between the open metal sites at the framework surface and the guest molecules. Electronic density changes due to ozonization were determined by photoelectron spectroscopy analysis. The cell contraction and the presence of residual methanol molecules in the porosity reduced the hydrogen and carbon dioxide retention capacity of the samples. Changes in bond strengths were corroborated by binding energy shifts of atoms core levels after ozonization. Additionally, a structural study of hydrated and dehydrated phases of manganese(II) hexacyanocobaltate(III) was conducted using single crystals diffraction experiments to describe the nature of its structural disorder. Results showed a correlation between vacancies, which implies that vacancy distribution is not random, as was previously assumed. Also the thermal expansion coefficient of each phase using single crystals X-ray diffraction data was determined in order to analyse the interaction of water molecules with the framework.

# Introduction

Adsorption, separation and catalysis are key processes in the modern global economy [1–3]. A primary concern in the implementation of technological solutions for these processes is tailoring porous materials with specific storage capacity, pore size distribution (PSD) and adsorption energy distribution (AED) [4–7]. Hydrogen storage and carbon dioxide capture are major areas of interest within the field of porous materials science [8–12] because hydrogen molecule is a sustainable energy carrier [13] and anthropogenic carbon dioxide has high environmental impact [14]. However, a transition to a hydrogen-based economy or a significant reduction in anthropogenic carbon dioxide emissions are not currently viable [15,16]. Therefore further studies regarding the effect of the adsorbents properties on hydrogen and carbon dioxide adsorption is needed.

To be able to perform such adsorption studies in porous materials it is imperative to first determine adsorbent structure, specifically their pore size distribution [17]. This PSD changes with temperature, also changing the AED. Therefore, determination of the isobaric thermal expansion coefficient on porous materials provides useful information about structural changes related with temperature. Structural determination in material science is commonly achieved using X-ray diffraction techniques. Traditional X-ray diffraction analysis only provides information about the average crystal structure. However, some properties of materials cannot be explained from the average structure as these depend on local deviations from this average [18]. In disordered porous materials (crystalline materials with vacancies), these deviations are essential to describe their chemical and physical properties. Recent tools like the pair distribution function (PDF) have been developed to analyze X-ray diffraction data in crystalline materials with structural disorder. This function includes both long range structural correlations (Bragg peaks) to determine average structure and short range (diffuse scattering) to

determine local structure; providing a more complete information to build structural models for a great variety of materials. For disordered porous materials the average structure is unable to provide all the necessary information to determine both PSD and AED [19] The framework can not be reproduced based on a unit cell because pore sizes are irregular and as a result, also are their adsorption energies. For this reason local structure data is of a vital importance to describe their adsorption properties.

Within this group, porous materials with exposed metal sites are of particular interest for adsorption applications [20]. An interesting subset, transition metal hexacyanometallates, represent an attractive family with a great diversity of topologies and pore sizes [21–30]. Some members of this family also have a high density of open metal sites on their pores walls [22] and other members, have exchangeable metal cations [31–33]. Open metal sites and exchangeable metal cations are specific adsorption centres with intense field gradients, which are able to interact with molecules with a quadrupolar moment of great technological interest, such as: H<sub>2</sub> [20], CO<sub>2</sub> [34], O<sub>2</sub> [32], and N<sub>2</sub> [32]. These electrical features have proven to be useful in combustion exhaust gas purification processes [35] and in oxygen and nitrogen air enrichment [32]. The same characteristics have guaranteed the adsorption and separation of light n-alkane hydrocarbons [36]. Compounds with exchangeable cations have also found application in sodium-ion rechargeable batteries development [33].

The use of transition metal hexacyanometallates in the aforementioned applications requires a framework degassing process to remove the solvents used during the synthesis or to remove other molecules previously exchanged with the original solvents. This is a common step for most molecular sieves application [37, and references therein]. The transition metal hexacyanometallates precursors are salts soluble in polar solvents such as water. This is why the vast majority of them are obtained with polar molecules in their frameworks. Polar solvents interact strongly with the framework which is beneficial for the retention of some gases as ammonia at trace level [38]. However, it becomes a high energy consuming process when framework degassing is required. A systematic studies of solvent-framework interactions in transition metal hexacyanometallates are rare [33,39] so, further research on the subject is required.

Transition metal hexacyanometallates are also excellent research candidates because the active vibrational modes are sensitive to the presence of guest molecules [40,41]. This feature allows monitoring the adsorption

process inside the pores.

A few decades ago, Reguera *et al.* demonstrated that oxidation states of open metal sites in some porous cyanometallates can be modified through a reaction with ozone [42–45]. These reactions were conducted without dehydrating the material and therefore, water molecules were involved in the reaction. No attempt was made to conduct the experiment on dehydrated frameworks neither to show the effect of oxidation states in gas adsorption properties. However, the possibility of modifying post-synthesis the oxidation states of metals with open coordination sites allows to explore the effect of the metals oxidation state on the adsorbate–adsorbent interactions.

The modification of metals oxidation states induce changes on this materials electronic density, directly modifying AED, and also PSD through bond distances modification. Both changes, the ones in oxidation states and in bonds strengths, after ozonization can be quantified by X-ray photoelectron spectroscopy (XPS) analysis.

In this work, we have designed and implemented an experimental setup to conduct post-synthesis modification of oxidation states of open metal sites in manganese(II) hexacyanocobalte(III) (MnHCC) and cobalt(II) hexacyanocobalte(III) (CoHCC) frameworks. Modification were performed with ozone in an environment free of solvents. Experimental details are described in Chapter 2. This experimental system was built in order to explore the effect of open metal sites oxidation states on  $H_2$ ,  $CO_2$ ,  $H_2O$  and  $CH_3OH$  interactions with MnHCC and CoHCC frameworks.

In Chapter 3, the isobaric thermal expansion coefficient for MnHCC is calculated in hydrated, dehydrated and partially dehydrated states. Local structure information is discussed from diffuse scattering experimental data. In Chapter 4, a variation of Langmuir-Freundlich adsorption model to improve data interpretation is discussed. Ozonization effect on both materials frameworks is presented in Chapter 5 with a discussion of the impact in reversibility of  $H_2O$  and  $CH_3OH$  adsorption. The adsorption of  $H_2$ ,  $CO_2$  in MnHCC and CoHCC partially desolvated frameworks is also discussed. Finally, changes in oxidation states, structural order and bond lengths are studied in Chapter 6.

## **Hypothesis**

By using post-synthesis modification of the oxidation states of metals coordinated to nitrogen in transition metals hexacyanometallates, it is possible to shift the partial enthalpy of adsorption distribution to higher values.

## **Aim**

To implement a methodology for post-synthesis modification in manganese and cobalt hexacyanocobaltates (MnHCC and CoHCC, respectively) to modify their retention capacities and distribution functions of adsorbate-adsorbent interaction energies for hydrogen and carbon dioxide adsorption.

## **Research Objectives**

1. To design and implement an ozonization system to conduct post-synthesis modification of oxidation states of open metal sites at manganese hexacyanocobaltate (MnHCC) and cobalt hexacyanocobaltate (CoHCC) frameworks in an environment free of solvents.
2. To determine structural changes induced by solvents evolution on both materials before and after the post-synthesis modification with ozone.
3. To determine temperature evolution of both materials frameworks before and after post-synthesis modification with ozone.
4. To propose a theoretical isotherm equation based on Vacancy Solution Theory to describe carbon dioxide and hydrogen adsorption on the molecular sieves studied.
5. To determine the effect of the manganese and cobalt oxidation states in the retention capacity and the partial enthalpy of adsorption for hydrogen and carbon dioxide.

# Part I

## State of the art

# Chapter 1

## Background

### 1.1 Average *vs.* local structure in crystallography

Since the first discovery of the diffraction of X-rays by crystals, crystallography has grown into a very precise and widely applicable tool [46,47]. The success of conventional crystallography (crystal structure determination) is due to the same basic method being applied to materials as diverse as a simple salt which contains only a few atoms per unit cell or to a macromolecular crystals which may contain thousands of atoms per unit cell [47]. The basic assumption in all cases is that the crystal consists of a three dimensional array of identical units, and this gives rise to a diffraction pattern consisting of discrete diffraction peaks (Bragg reflections). Those discrete peaks describe just the ideal structure.

However real materials only approximate this ideal. The diffraction patterns of most materials contain, in addition to sharp Bragg peaks, a weak continuous background known as *diffuse scattering* [19]. This scattering necessarily arises whenever there are deviations from the ideal of a perfectly regular array of identical units. Such deviations from the ideal state may arise in a whole variety of ways and to different extents, but all of these effects may be brought together under the definition of *structural disorder*. Although much of present day knowledge of solid-state has been derived from crystallographic studies using Bragg diffraction, the properties of many important materials are dependent not simply on the average crystal structure but are often crucially dependent on the deviation from the ideal state

that are present. For example, the useful mechanical properties of many alloys and ceramics, the opto-electronic properties of many materials, many electrical properties of semiconductors, high-temperature superconductivity, etc., depend upon the presence of various types of disorder [17, 48].

For X-rays, the basic scattering event of a photon interacting with a crystal lattice occurs on a time scale of approximately  $1 \times 10^{-16}$  s [47]. This is several orders of magnitude faster than typical thermal vibration frequencies, so to a good approximation the X-ray diffraction experiment describes atoms or molecules that are statically displaced from their average positions as a result of such thermal motion. The scattering associated with this thermal motion is known as *Thermal Diffuse Scattering* or TDS. Disorder may also arise as a result of mixing different atomic or molecular species (solid solutions) or where a molecular species can pack into the basic crystal lattice in two (or more) quite different orientations [17]. Such structural defects may occur as isolated point substitutional defects, clusters of such defects, or as interstitials where the defect atoms occur on sites not normally occupied in the average lattice. The scattering associated with this so-called occupational or chemical disorder is often termed *Short-Range Order* (SRO) diffuse scattering. Occupational disorder will normally be accompanied by (static) atomic distortions that help mitigating local stresses and these distortions also give rise to diffuse scattering. In most real materials thermal, substitutional, and static displacement diffuse scattering will be present to varying degrees and instances can be found where any one of these dominates the diffraction pattern [19].

Whereas the conventional analysis of Bragg peaks provides information about the average crystal structure (atomic coordinates, site-occupancies or mean-square atomic displacements), diffuse scattering contains information about how pairs of atoms behave. Thus, it is potentially a rich source of information on how atoms and molecules interact [19]. Crystallographers have been aware of such scattering since the earliest times, but development of techniques for recording and analysing it have lagged well behind the advances made in conventional crystallography. Typical diffuse intensities are several orders of magnitude below Bragg peak intensities, and this was clearly a major impediment to earlier generations of researchers. However, with advances in X-ray sources (rotating anodes, synchrotron radiation) and in methods of detection (linear-detectors, area detectors, CCDs, image plates, etc.), now good quality diffuse diffraction data are much more readily accessible. Therefore, obtaining good quality data is no longer the main

impediment to extract information from diffuse scattering [49].

Figure 1.1 illustrates an example of correlated disorder in water ice crystals due to different orientations of water molecules [17].

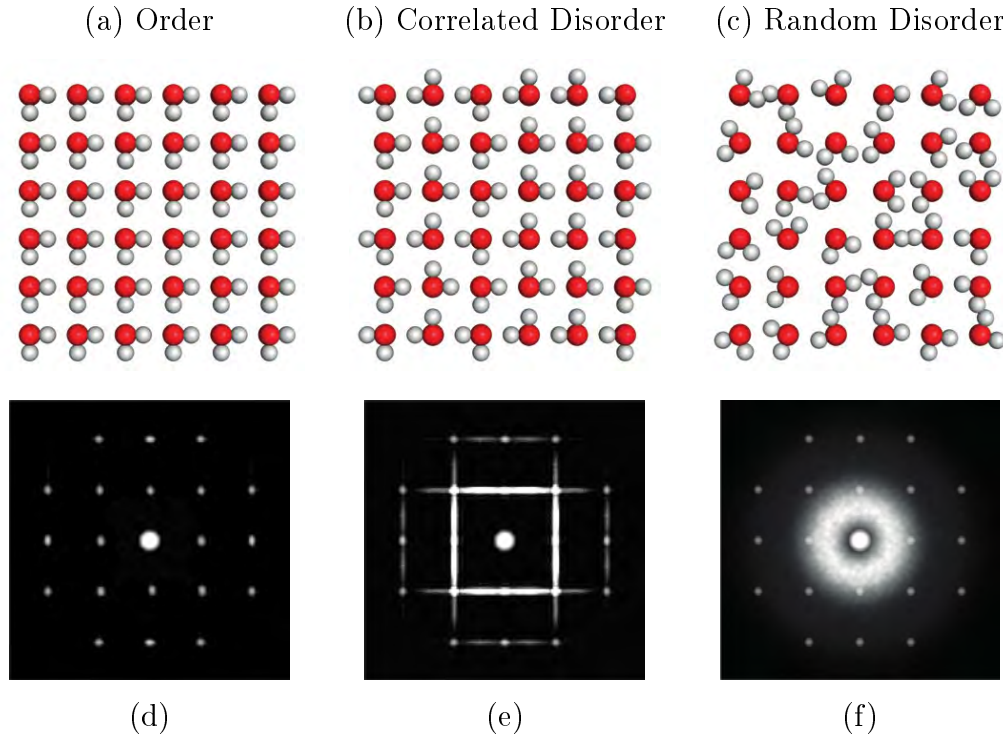


Figure 1.1: The figure shows how structures with correlated disorder (b, e) fall in between those with complete order (a, d) and those that are disordered randomly (c, f). The differences between the structures of the systems (a,b,c) are evident from the diffuse scattering in their diffraction patterns (d,e,f). The example used is that of square ice, a simplified two-dimensional representation of the three-dimensional structure of water ice. Taken from reference [17].

The average crystallographic unit cell for square ice has two 50% occupied hydrogen sites (white) between each pair of oxygen sites (red). Since the repeating lattice is the same for structures (a), (b) and (c), their Bragg scattering (shown as grey dots in the X-ray diffraction plots in (d), (e) and (f)) is indistinguishable. It is therefore the broad or diffuse scattering in plots (d),(e) and (f) that are sensitive to the differences between these structures.

In case (a), each oxygen atom is surrounded by four hydrogen atoms; two of these hydrogen atoms are covalently bonded and two are hydrogen-bonded to the oxygen atom. This spatial arrangement [50, 51] leads to an ordered structure. No diffuse scattering in plot (d) is observed for this ordered structure. The second structural variant (b) is, despite the disorder, more likely because the short-range nature of the interaction between their atoms result in structures with correlated disorder and residual low-temperature entropy [52]. The correlation in (b) involves all O–H bonds pointing along a common direction for each individual row and each column. In this case the structure is disordered because these directions O–H are not correlated across rows or columns, but is not completely random as in (c). The corresponding diffraction pattern in plot (e) for structure (b), has horizontal and vertical lines of diffuse scattering due to the locally correlated hydrogen atom positions. Structure (b) can be contrasted with the random arrangement of water molecule orientations on a square lattice (c), whose average unit cell would have a ring of hydrogen density around each oxygen site; this gives a broad ring of diffuse scattering centred at the origin (as in plot (f)), similar to the familiar solvent ring seen in diffraction from proteins [53].

The major impediment to use diffuse scattering information is the diversity and often complex combination of disorder effects that arise in nature and the fact that until recently no simple method of analysis has been available which can usefully deal with all of them [19]. A computer simulation of a model crystal provides a general method by which diffuse scattering of all kinds and from all types of materials can be interpreted and analysed. Such methods have only been feasible since the advent of powerful and relatively inexpensive computers.

Of crucial importance in the study of disorder problems is an appreciation of the theory of disordered systems. This appreciation not only means an understanding of how different types of disorder give rise to particular diffraction effects but more importantly an appreciation of what correlation means: What does it mean for occupancies and for displacements, how does it occur in a lattice and how does it vary with distance? What constraints are there on values that correlation can take? What does it mean by pair correlations and multi-site correlations and what is the relationship between them?

In Chapter 1 section 1.3 and 1.3.1, structure of the hexacyanocobaltates is discussed based in crystallographic data able to describe only the average structure. In Chapter 3, structural disorder of manganese hexacyano-

cobaltate (MnHCC) is discussed based on experimental diffuse scattering evidence.

## 1.2 Thermal expansion of crystals

The way crystalline materials respond to changes in temperature and pressure are important for the valuable insight they provide into the fundamental chemistry of the solid state. Also for their use in a wide range of practical applications such as negative thermal expansion (NTE) in Metal-Organic Frameworks (MOFs) [54–57] and transition metal hexacyanides [58], negative linear compressibility (NLC) in molecular co-crystals [59] and extreme gating responses to guest sorption in microporous materials [60–62].

Crystallographic techniques offer a direct and straightforward measure of any structural variation: the evolution of unit-cell parameters describes the bulk mechanical response of the material, with the corresponding changes in atomic positions indicating the microscopic mechanism responsible for this response. Thus, for any given system, determination of the temperature and/or pressure dependence of its unit-cell parameters is a simple but effective means of diagnosing anomalous (and useful) mechanical behaviour [63].

The mechanical behaviour in a single crystal is described by a second rank tensor  $\varepsilon$ : the strain tensor. Its dependence on the scalar parameter  $T$  is also represented by the second-rank tensor  $\alpha$  that is called the thermal expansion tensor [64].

$$\varepsilon_{ij} = \alpha_{ij}dT \tag{1.1}$$

$$\alpha = \begin{bmatrix} \alpha_{11} & \alpha_{12} & \alpha_{13} \\ \alpha_{21} & \alpha_{22} & \alpha_{23} \\ \alpha_{31} & \alpha_{32} & \alpha_{33} \end{bmatrix}$$

The central concept that allows to use the tensor algebra for the representation of the crystal thermal expansion behaviour is that for any system there exists a unique set of axes (also called the principal axes) along which the material responds in a purely linear fashion, either expanding or contracting, with the response along other directions involving some non zero shear component. It is the expansion or contraction along the principal axes that describe the fundamental mechanical response of the system.

It is more convenient to represent the tensor in the form reduced to the principal axes, i.e., in the Cartesian coordinate system in which the tensor is described by the diagonal matrix:

$$\alpha = \begin{bmatrix} \alpha_1 & 0 & 0 \\ 0 & \alpha_2 & 0 \\ 0 & 0 & \alpha_3 \end{bmatrix} \quad (1.2)$$

The crystal symmetry plays a crucial role in determining the orientation of these axes, imposing limitations on the thermal expansion tensor [65]. For monoclinic and triclinic crystal classes, the principal axes are not necessarily related to the unit cell axes and must instead be determined as the eigenvectors of the full strain tensor [65]. In crystals of the cubic crystal system, all diagonal components of the thermal expansion tensor are equal ( $\alpha_1 = \alpha_2 = \alpha_3 = \alpha_l$ ), the other components are identically equal to zero, and the principal axes can be chosen in an arbitrary manner (it is common practice to choose them in parallel to the crystallographic axes). In this case, in order to fully describe the crystal thermal behaviour, it is sufficient to calculate the thermal expansion coefficient in one arbitrarily chosen direction.

From the thermodynamic point of view [66], the isobaric thermal expansion coefficient  $\alpha$  can be calculated using equation 1.3 and for a cubic structure ( $V = l^3$ ),  $\alpha$  is directly related with the lineal thermal expansion coefficient  $\alpha_l$  as shown in equation 1.7.

$$\alpha = \frac{1}{V} \left( \frac{\partial V}{\partial T} \right)_{p,n} \quad (1.3)$$

$$= \frac{1}{l^3} \left( \frac{\partial (l^3)}{\partial T} \right)_{p,n} \quad (1.4)$$

$$= \frac{3l^2}{l^3} \left( \frac{\partial l}{\partial T} \right)_{p,n} \quad (1.5)$$

$$= 3 \left[ \frac{1}{l} \left( \frac{\partial l}{\partial T} \right)_{p,n} \right] \quad (1.6)$$

$$\alpha = 3\alpha_l \quad (1.7)$$

This is the trace of tensor in equation 1.2.

In Chapter 3 section 3.1, isobaric thermal expansion coefficients are calculated for hydrated, dehydrated and semidehydrated states of MnHCC single crystals using single crystals X-ray diffraction experimental data.

### 1.3 Structure of transition metals hexacyanometallates

The structural prototype for hexacyanometallates is the prussian blue (PB) [67]. The Prussian blue was the first modern synthetic pigment, used for centuries by european painters as the classical blue color. Four different variants are known [41,42]:  $\text{Fe}_4[\text{Fe}(\text{CN})_6]_3 \cdot n\text{H}_2\text{O}$  (insoluble, IPB),  $\text{FeK}[\text{Fe}(\text{CN})_6] \cdot n\text{H}_2\text{O}$  (soluble, SPB),  $\text{Fe}_3\text{M}[\text{Fe}(\text{CN})_6]_2 \cdot n\text{H}_2\text{O}$  (Turnbull blue, TB), where M is an appropriate cation, and the fourth variety obtained when the ferric ferricyanide is reduced to ferric ferrocyanide  $\text{Fe}(\text{H}_3\text{O})[\text{Fe}(\text{CN})_6] \cdot n\text{H}_2\text{O}$  (APBr) [68]. All these compounds crystallize in the cubic system.

Molecular materials formed by octahedral blocks  $[\text{Ma}(\text{CN})_6]^n$  (where Ma is an internal transition metal) bound by an outer transition metal (Mb) are analogous to the prussian blue family. A very important group within this family is the group of materials of molecular formula  $\text{Mb}_3[\text{Ma}(\text{CN})_6]_2 \cdot n\text{H}_2\text{O}$  which are known as transition metal(II) hexacyanometallates(III) [68–70]. Their structures are based on a three dimensional array of chains  $\text{Mb}^{\text{II}}-\text{N}\equiv\text{C}-\text{Ma}^{\text{III}}$ . The metal Ma is bonded to carbon forming octahedral molecular blocks of the form  $\text{Ma}(\text{CN})_6$ , while the metal Mb acts as an assembling element for the octahedral blocks and may have a tetrahedral or an octahedral coordination [71]. Except in the case of zinc [72], Mb is in a pseudo-octahedral coordination [22].

In these materials the charge balance is guaranteed by the absence of a molecular block  $[\text{Ma}(\text{CN})_6]^{3-}$  for every three external transition metals Mb. This absence implies the existence of vacancies in the crystalline structure (Figure 1.2) that gives rise to pores with diameters approximately of  $8.5 \text{ \AA}$ <sup>1</sup>, although there are also interstitial pores located around the inner metal of approximately  $4.5 \text{ \AA}$  in diameter [22]. Each pore originated by a vacancy leaves at most six external metals with an unsaturated coordination sphere. These vacancies are filled with water molecules, which can be removed without col-

<sup>1</sup>Pores of around  $8.5 \text{ \AA}$  are formed if they are isolated. However they can be combined to form bigger pores.

lapsing the lattice [73, 74]. The pores have specific polar adsorption sites in their walls due to the rupture of the configurational octahedral symmetry by the presence of vacancies. Consequently, these materials have been extensively studied as adsorbent and molecular sieves [20, 32, 34, 75].

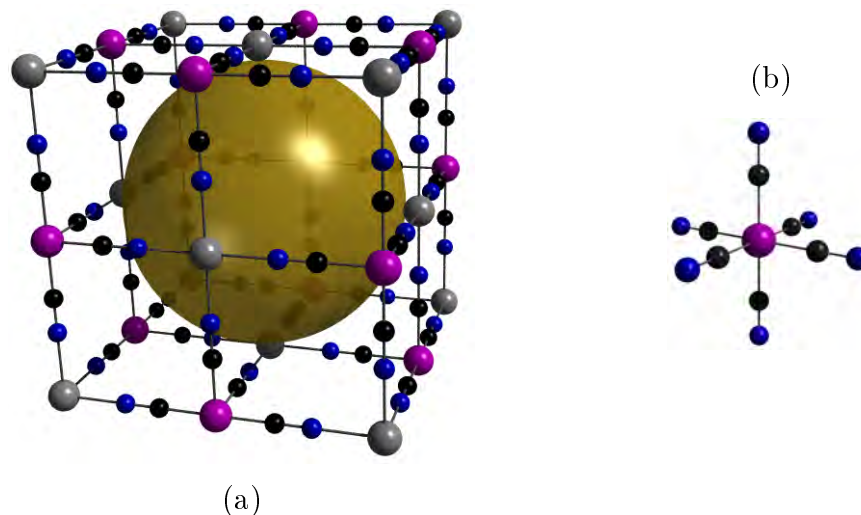


Figure 1.2: Spatial arrangement of atoms for hexacyanides. a) Unit cell with one vacancy (absence of  $[\text{Mi}(\text{CN})_6]^{-3}$  molecular block). b)  $[\text{Mi}(\text{CN})_6]^{-3}$  molecular block.

Materials with molecular formula  $\text{Mb}_3[\text{Ma}(\text{CN})_6]_2 \cdot n\text{H}_2\text{O}$  can crystallize in three different space groups<sup>2</sup>  $R\bar{3}/c$ ,  $Pm\bar{3}m$  and  $Fm\bar{3}m$ , [72, 76, 77]. Only those compounds in which  $\text{Mb} = \text{Zn}$  that additionally are synthesized at temperatures higher than the ambient temperature or remain for prolonged periods of time at very low humidity conditions, crystallize or change phase to  $R\bar{3}/c$  [72]. This phase has no vacancies and it is unstable therefore, it is beyond the scope of this thesis. The phases that crystallize in the cubic space groups  $Pm\bar{3}m$  and  $Fm\bar{3}m$  are stable and differ mainly in the arrangement and number of vacancies in the crystal lattice, which determines that their volumetric densities are different [76].

Space group  $Pm\bar{3}m$  has ordered vacancies of the  $[\text{Ma}(\text{CN})_6]_3^-$  blocks in 50% of the internal metal sites [76] (Figure 1.3). There are two positions for the outer metal Mb (1a and 3c), and two for the internal metal Ma (1b

<sup>2</sup>Space groups 167,221 and 225 respectively

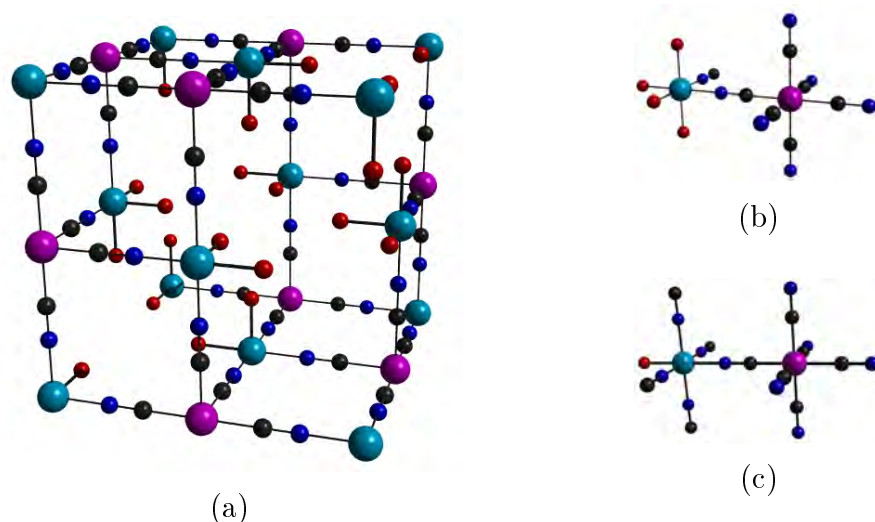


Figure 1.3: Structure of CuHCC ( $Pm\bar{3}m$ , ordered vacancies). a) The spatial arrangement of atoms can be reproduced using a unit cell with an ordered arrangement of vacancies. b) There are two different coordination environments for copper atoms.

and 3d). The former have an occupancy factor of one, while the latter have occupancy factors of 0.048 and 0.092 respectively. This structural characteristics leads to two different coordination environments for the outer metal  $Mb(NC)_2(H_2O)_4$  (1a) and  $Mb(NC)_5(H_2O)$  (3c). In this model, there is one molecule per unit cell, which suggests that the structure has a volume accessible to solvents greater than that corresponding to cells  $Fm\bar{3}m$ , where there are 1.33 molecules per cell.

In the  $Fm\bar{3}m$  structural model, vacancies are found in 33.3% of the sites of the internal metal, distributed randomly [77] (Figure 1.4). In the latter, the outer metal has a mixed coordination of the type  $Mb(CN)_{6-n}(H_2O)_n$ , where  $n = 0, 1, \dots, 6$ . The probability of finding it in each configuration obeys a binomial distribution. The morphology of the pores is very diverse due to the random nature of their vacancies. Experimental evidence found in recent years in other materials of the hexacyanocobaltate family suggests the possibility that some of them may be found at some intermediate point between the phases with ordered and disordered vacancies [76].

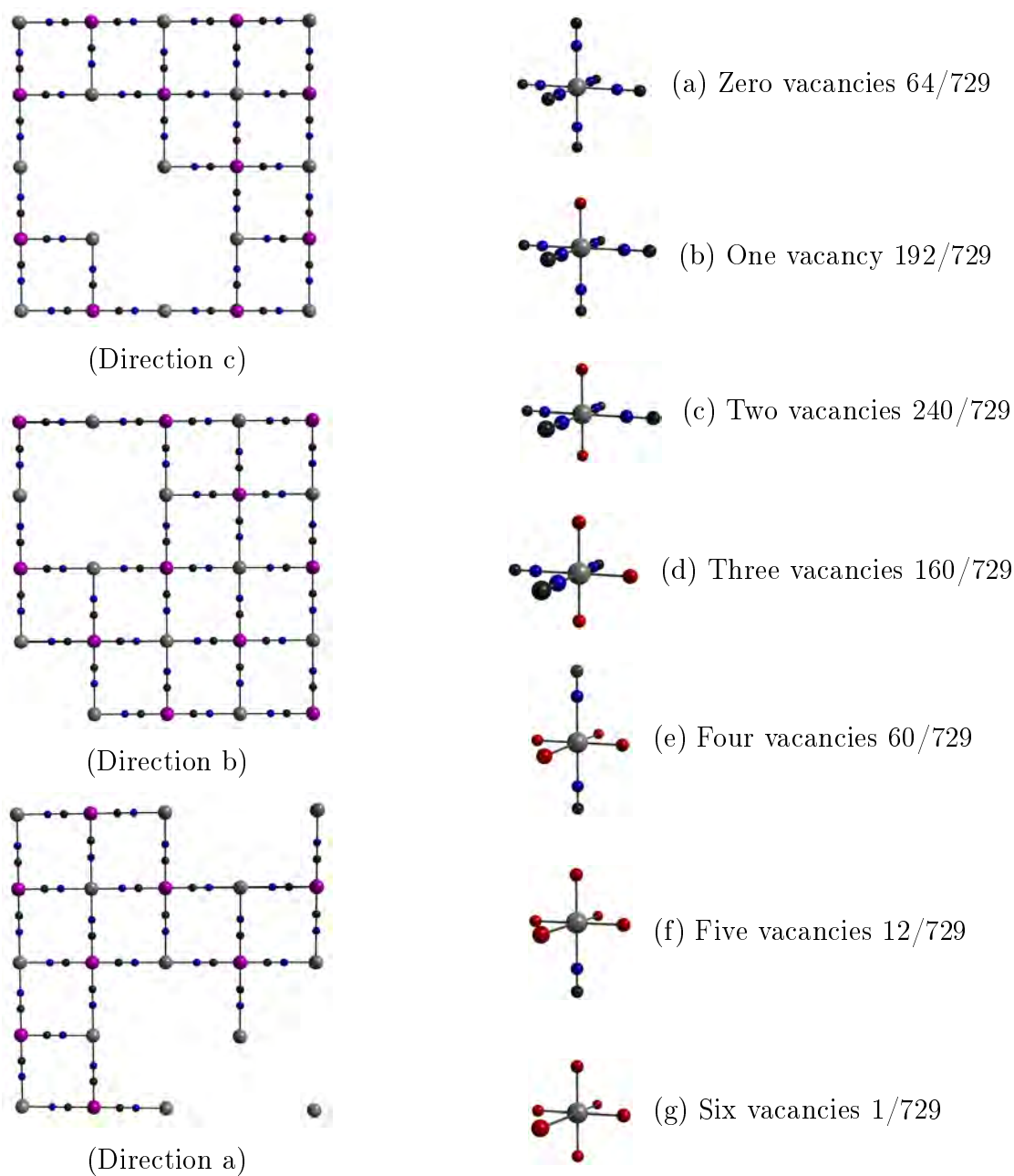


Figure 1.4: Structure of MnHCC ( $Fm\bar{3}m$ , disordered vacancies). The spatial arrangement of atoms can not be represented using one unit cell. a) Supercell of  $2 \times 2 \times 2$  viewed in crystallographic directions a, b and c. b) There are seven coordination environments for manganese in MnHCC with different probabilities

### 1.3.1 Review of manganese and cobalt hexacyanocobaltate structures.

The first structural model for Manganese Hexacyanocobaltate (MnHCC) was proposed by Keggin and Miles [78] based on powder diffraction refinement, due to the high insolubility of the transition metal-cyanide complexes. In this model, both metals ions ( $\text{Mn}^{2+}$  and  $\text{Co}^{3+}$ ) were at the special positions 4a and 4b respectively, in  $Fm\bar{3}m$  space group unit cell, and had the same occupancy factors. Additional  $\text{Mn}^{2+}$  ions were randomly distributed in the special positions 8c to reach electroneutrality. The crystallographic positions of  $\text{H}_2\text{O}$  molecules were neglected and there were two formula units per unit cell. Both assumptions were in disagreement with experimental density and analytical findings, as was demonstrated later [79]. Also, the interatomic distances were not correct and there were no vacancies in the framework.

Ludi et al. [79] proposed a structural model based on single crystal refinement. The spatial arrangement of atoms was a three-dimensional array of two octahedral coordination units:  $\text{CoC}_6$  and  $\text{MnN}_4(\text{H}_2\text{O})_2$  (average composition). Four Mn were at the special position 4a of the face centered unit cell, one third of the Co (4b), C(24e) and N (24e) special positions were not occupied. Due to the high symmetry of the  $Fm\bar{3}m$  group, these vacancies (missing  $[\text{Co}(\text{CN})_6]^{3-}$  anions), were assumed to occur randomly. The structure had two types of water molecules which were distinguishable with respect to their crystallographic position as well as their bonding. There were 8 water molecules at the special position 24e, replacing the missing nitrogen atoms octahedrally coordinated to the four Mn atoms. Other 8 water molecules were at the special position 8c filling the interstitial space. This model had  $1\frac{1}{3}$  water molecules per unit cell, in better agreement with experimental density. The unit cell parameter was  $a = 10.421 \pm 0.005$  Å. The difference Fourier map showed a small diffuse peak near the position 4b that was not in complete agreement with the structural model. This could not be explained due to the limitations of the experimental technique.

Ludi work was complemented by Beall *et al.* [77] using neutron and X-ray diffraction techniques. The unit cell parameter was  $a = 10.436 \pm 0.003$  Å. The transition metals interchanged atomic position in relation to Ludi's model. Carbon, nitrogen and coordinated water molecules continued to be at the special position 24e. In the average structure, the atoms next to Mn continued to be disordered with almost the same occupation factors they had in Ludi's model and four different types of water molecules located at the

special positions 4a, 24e, 8c and 32f were reported. In Beall's model two different coexisting configurations were suggested to explain neutron and X-ray data. The first configuration was an ordered arrangement of the metal atoms and cyanide ligands. Additional atoms of Mn with occupancy  $\frac{1}{4}$ , are sharing position 8c with interstitial water molecules. This configuration is present  $\frac{1}{3}$  of the time in average structure. For the second configuration, none of the atom sites is fully occupied. This configuration exists  $\frac{2}{3}$  of the time. The cobalt atoms share position 4a with the water molecules. Although Beall model tried to explain experimental diffuse evidence, the two different configurations are randomly distributed. Therefore, local ordering was not considered in any of the above-mentioned models.

New models [22, 80] have been suggested for the  $\text{Mn}_3[\text{Co}(\text{CN})_6]_2 \cdot n\text{H}_2\text{O}$  structure, based on powder diffraction studies, but they are not discussed here because single crystal scattering provides better quality data to propose a structural model. The zeolitic nature of part of the water molecules, implies a broad range of hydration for this structure depending on ambient conditions.

There are no previous reports on structural models for CoHCC based in single crystal diffraction analysis. The structural model reported by Ludi *et al.* [81], from powder diffraction data, indicates that CoHCC crystallizes also in the  $Fm\bar{3}m$  space group with an unit cell parameter of  $a = 10.210 \pm 0.005 \text{ \AA}$  and it has random vacancies [81]. According to the experimental density, there are 1.33 formula units per unit cell. Four  $\text{Co}^{2+}$  ions are in the special position 4a and 2.67  $\text{Co}^{3+}$  ions are in the special position 4b. Additionally, 16 Carbon and 16 nitrogen atoms are in the special position 24e. They report two types of water molecules: 8 water molecules in the special position 96k (near 24e) and 8 water molecules at the general position 192l (near 8c).

The work of Reguera *et al.* offers an structural variant to better fit the structural disorder observed in the background of the powder X-ray diffraction pattern [22]. Although the assigned spatial group continues to be  $Fm\bar{3}m$  and the unit cell parameter is very similar to Ludi's work ( $a = 10.2202 \pm 0.0001 \text{ \AA}$ ) there is one formula unit ( $\text{Co}_4[\text{Co}(\text{CN})_6]_{2.67} \cdot 17.64\text{H}_2\text{O}$ ) per unit cell. Both metal cations were removed from positions 4a and 4b to the special position 24e. The nitrogen and carbon atoms were also in the position 24e. There were four types of water molecules in the structure in the special positions 4a, 24e, 32f and 8c. Occupancy factor were altered to fit the stoichiometry.

An additional work assigned the  $F\bar{4}3m$  space group to CoHCC also with random vacancies [80]. This structural model is not going to be explain here

because there is no experimental evidence derived from this work to support the assignation of the  $F\bar{4}3m$  space group.

Previous works indicate that neither of the two structures (MnHCC and CoHCC) collapses after dehydration [73,74,82] and the unit cell volumes are reduced by proximally 4% [22]. Nevertheless, the local structural changes due to dehydration are still not clear.

The existence of several structural model to describe MnHCC and CoHCC materials is directly related to their structural disorder. As can be concluded from this section, the conventional crystallographic analysis is insufficient to generate an appropriate structural model and therefore, additional local structure information is necessary to better understand their complex structures and to understand how this structures change due to the loss of water molecules. We intend to evaluate these changes from X-ray single crystal diffraction taking MnHCC as an example.

In chapter 3, the evolution of MnHCC framework due to the interaction with the water molecules is studied based in the comparison between the linear thermal expansion coefficients of hydrated, dehydrated and partially dehydrated states. Local structure information is analysed in the form of diffuse scattering for hydrated and dehydrated states.

## 1.4 Hydrogen and carbon dioxide adsorption in porous materials

### 1.4.1 Interaction of H<sub>2</sub> and CO<sub>2</sub> molecules with crystalline porous solids

The nature of H<sub>2</sub> and CO<sub>2</sub> interactions with crystalline surfaces is determined by each gas physicochemical properties. The H<sub>2</sub> molecule has an ellipsoidal shape, it has no electric dipole moment but it does has a quadrupole moment  $Q = 0.4926 ea_0^2$  which allows it to interact with an electric field gradient  $\nabla E$  [83]. The positive sign of its quadrupole moment indicates that when H<sub>2</sub> molecule interact with the electric field, it is oriented transversely to the electric gradient direction. As a result of this interaction, the absorbed complex has a T-shaped configuration [84]. On the other hand, CO<sub>2</sub> molecule has a linear geometry. It has no dipole moment, but its ellipsoidal shape determines the existence of a quadrupole moment  $Q = -2.987 ea_0^2$ . The

negative sign of this moment causes the molecule to be oriented with the main axis of its ellipsoid on the direction of the field gradient [85]. This feature explains why their electric behaviour is essentially different. Both molecules are also affected by external electric fields through induced dipole interaction, although CO<sub>2</sub> polarization constant ( $\alpha = 2.507 \text{ \AA}^3$ ) is three times bigger than the one for H<sub>2</sub> ( $\alpha = 0.802 \text{ \AA}^3$ ) [86]. Relevant types of interactions of both molecules with nanoporous structures are described below.

H<sub>2</sub> molecules interact with nanoporous structures in four different ways [87]. They can be polarized in the presence of a strong external electric field ( $E$ ). The stabilization energy in this case would be  $\Delta H = \alpha E^2/2$ , where  $E^2$  is a function of  $r^{-4}$  ( $r$  is the interaction distance). Another form of interaction is manifested between the quadrupole moment of H<sub>2</sub> and the local electric field gradient  $\nabla E$ , with a stabilization energy given by  $\Delta H = (Q \cdot \nabla E)/3$ . This type of interaction depends on  $r^{-3}$ . The third form is a dispersive interaction whose nature lies in the resonant fluctuation of the electron charge distribution between the H<sub>2</sub> molecule and the material surface or between neighbouring host molecules. This interaction has two terms, an attractive term that depends on  $r^{-6}$  and a repulsive term (due to the overlap of the electronic clouds) that depends on  $r^{-12}$ . All three interactions described above will be favoured when the H<sub>2</sub> molecule is confined in nanocavities of about 1 nm.

The fourth type of interaction is the coordination of H<sub>2</sub> molecules to metal centres. Coordination interaction is of a great importance for this work because this is the interaction that changes the most after ozonization. The H<sub>2</sub> molecules are coordinated to donate charge from its  $\sigma$  bond orbitals to the metal. This is a relatively weak coordination interaction but it is favoured if the metal has  $d$  orbitals, in particular  $t_{2g}$  located in an appropriate arrangement to retro-donate electronic charge density to the H<sub>2</sub> antibonding orbital  $\sigma^*$ . The above mentioned process of metal–H<sub>2</sub> donation is favoured for metals with very extensive (diffuse)  $d$  orbitals. The H<sub>2</sub>-Metal coordination energy is a function of the metal, its valence state, and other groups present in its coordination environment.

CO<sub>2</sub> molecules have the same type of electrostatic interactions with porous solid as H<sub>2</sub> because of their electrical similarities. Stabilization inside the pores is related to Van der Waals forces and the interaction of CO<sub>2</sub> quadrupole moment with the electric field gradient on the surface of the pores [22].

These different types of H<sub>2</sub> and CO<sub>2</sub> interactions with porous materi-

als surfaces has different contributions to the adsorption energy. Studies of hydrogen storage in porous materials indicate that volumes occupied by adsorbates at pressures of the same magnitude order than atmospheric pressure are determined by the strength of host-host interactions. Molecular simulations made in these materials to estimate adsorption heats, show that optimum values are between  $20 \text{ kJ mol}^{-1}$  to  $30 \text{ kJ mol}^{-1}$  [88]. Adsorption heats for  $\text{H}_2$  close to ideal values were reported in porous silicas with extended surfaces and  $\text{Ti}^{3+}$  metals with unsaturated coordination spheres ( $22 \text{ kJ mol}^{-1}$ ). However,  $\text{H}_2$  adsorption gravimetric density is less than 6% in weight.

These values of adsorption heats are related to the existence of  $\text{H}_2$  coordination bonds with unsaturated metal centres, which suggests that the optimization of this type of interaction may be the key to achieving appropriate adsorption heats and adequate mechanisms of reversibility, able to meet mobile applications criteria imposed by the department of Energy of the United States. On the other hand, to increase the gravimetric density it is necessary to generate new adsorption sites. In this sense, the transition metal hexacyanocobaltates (object of study of this work) are a good model to study host-host interaction. In them the cavities are of 0.85 nm, which guarantees the existence of all the interactions previously discussed. Hexacyanometallates also offer high density of heterogeneous adsorption sites because their surfaces (BET) are of the order of zeolites, but they have the advantage of being covered by metallic cations of transition metals with unsaturated coordination spheres (six cations in each pore). Ideally, in this cavity diameter it would be possible to store at least 7  $\text{H}_2$  molecules, six of them through a direct interaction  $\text{H}_2$ -metal and one at the center of the cavity, stabilized by  $\text{H}_2$ - $\text{H}_2$  electrostatic interactions. The CN ligand has the ability to donate electrons to the metal located on the surface of the cavities, which is favourable to the metal- $\text{H}_2$  coordination interaction. However, even though the reported adsorption heats show a definite dependence of the metal located on the cavity surface, they are lower than  $10 \text{ kJ mol}^{-1}$  in all cases [27, 73]. For  $\text{CO}_2$  molecule the adsorption heats are not higher than  $12 \text{ kJ mol}^{-1}$  [89].

In this work, it is proposed to increase the adsorption heats in the materials under study by increasing the local electric field in the walls of the pores. This is done by oxidizing the metal cations with ozone.

### 1.4.2 Adsorption applications in hexacyanocobaltates

Transition metal hexacyanometallates are porous materials containing metallic cations with unsaturated coordination spheres on their surface. This feature makes them excellent candidates as adsorbents and molecular sieves leading to a great number of investigations in processes of retention and separation of fuel gases like the  $\text{H}_2$  and the  $\text{CO}_2$  in these materials. In the hexacyanocobaltates family  $\text{Mb}_3[\text{Co}(\text{CN})_6]_2 \cdot n\text{H}_2\text{O}$  where  $\text{Mb} = \text{Mn, Fe, Co, Cu, Zn}$  and  $\text{Ni}$ , surface areas BET in the range of  $560 \text{ m}^2/\text{g}$  to  $870 \text{ m}^2/\text{g}$ , comparable to those in zeolites, were reported through the experimental measurement of Ar isotherms [73]. The adsorption isotherms of  $\text{H}_2$  for these materials show a high reversibility with a capture from 1.4 wt % to 1.8 wt % at 890 Torr and 77 K. No correlation was established between the BET surface and  $\text{H}_2$  capture for the values of pressures studied. The adsorption heats for hydrogen are in the range of  $6.3 \text{ kJ mol}^{-1}$  to  $6.9 \text{ kJ mol}^{-1}$  [73], except for  $\text{Mn}_3[\text{Co}(\text{CN})_6]_2$  having a value of  $5.3 \text{ kJ mol}^{-1}$  [73]. These bond energies are relatively low and are consistent with the results of high energy X-ray scattering experiments performed on a sample of  $\text{Mn}_3[\text{Co}(\text{CN})_6]_2$  with  $\text{H}_2$  and powder neutron diffraction which found no evidence of the binding of adsorbed molecules to the accessible metal sites [90]. The most likely position for the  $\text{H}_2$  molecules in the  $\text{Mn}_3[\text{Co}(\text{CN})_6]_2$  lattice is at the center of the pore, maximizing the Van der Waals interactions of this molecule with the pore surface. Powder neutron diffraction measurements of  $\text{Cu}_3[\text{Co}(\text{CN})_6]_2$  at low temperature (5 K) show two possible adsorption sites for  $\text{H}_2$ . The first one, located at the center of the pore (site  $(1/4, 1/4, 1/4)$ ), is the most prominent interstitial position within the structure; and the other, at  $(x, 0, 0)$ , is located at sites where  $\text{Cu}^{2+}$  is exposed as a result of vacancies of ions  $[\text{Co}(\text{CN})_6]_3^-$  [91]. Further adsorption studies of  $\text{H}_2$  in this family of materials illustrate that the adsorbent adsorbate interaction strength follows the order  $\text{Ni} > \text{Cu} > \text{Co} \sim \text{Cd} > \text{Mn} > \text{Zn}$  [82].

The  $\text{CO}_2$  isotherms on dehydrated hexacyanocobaltates show that there is a weak correlation between the strength of the adsorbate-adsorbent interaction and the metal on the pore surface [82]. This behaviour is attributed to the relatively large size of the  $\text{CO}_2$  molecule ( $2.40 \text{ \AA}$  of diameter), in addition to the fact that at 273 K the molecule is rotating [92]. For a linear molecule such as  $\text{CO}_2$  the dispersion and polarization interactions reach their maximum strength when the molecule is placed with its axis parallel to the surface of the cavity. The lowest interaction observed was found for the case

of Zn, and is attributed to the low accessibility of the molecule to the crystalline lattice of this material, because when dehydrated the Zn adopts pseudotetrahedral coordination. This results in a greater distance CO<sub>2</sub>-surface and a low adsorption potential for this molecule.

## 1.5 Reactions of ozone with transition metals

### 1.5.1 Physical and chemical properties of ozone molecule

The ozone molecule at its ground state has an obtuse angle of 116.82° [86]. The bond distance between the oxygen atoms is (1.278 ± 0.003) Å. It has no appreciable paramagnetic behaviour. The molecular structure corresponds to a resonance hybrid with four possible canonical forms (Figure 1.5).

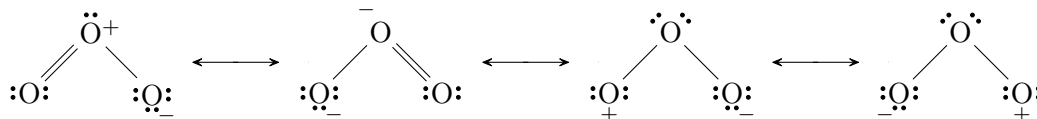


Figure 1.5: Canonical forms of the ozone molecule

The ozone molecule has a bent structure of  $C_{2v}$  symmetry. Each oxygen atom has  $sp_2$  hybridization, with two of the three  $sp_2$  orbitals of the central atom forming localized  $\sigma$ -type molecular bonds, in combination with the  $sp_2$  orbitals of the oxygen atoms at the ends. All unlinked  $sp_2$  orbitals contain 2 electrons, so that the entire molecule is surrounded by a cloud of  $\pi$  electrons, which come from the contribution of the unpaired atomic orbitals  $p$ . The small value of the total dipole moment in this molecule is explained because the dipole moment resulting from the free electron pair of the unbound  $sp_2$  orbital in the central atom is compensated by the dipole moment existing in the canonical forms. However, ozone has a diradical behaviour in singlet state in its ground state, which explains its electrophilic behaviour. In addition, ozone can function as 1,3-dipole and in some cases as nucleophile.

Ozone is thermodynamically unstable and its decomposition is exothermic:



Useful thermodynamic properties are listed below:

1. Standard heat of reaction for equation [1]

$$\Delta H_{298}^{\circ} = -142 \text{ kJ mol}^{-1}$$

2. Standard free energy of reaction [93]

$$\Delta G_{298}^{\circ} = -163 \text{ kJ mol}^{-1}$$

3. Entropy [94]

$$\Delta S_{298}^{\circ} = 239 \text{ J mol}^{-1} \text{ K}^{-1}$$

4. Heat capacity at room temperature [93]

$$c_p = 39.2 \text{ J mol}^{-1} \text{ K}^{-1}$$

5. Melting point [95]

$$80.45 \text{ K}$$

6. Boiling point [95]

$$161.25 \text{ K}$$

7. Critical point [95]

$$242.31 \text{ K and } 67.9 \text{ bar}$$

8. Dipole moment [96]

$$0.53 \text{ D}$$

9. Quadrupole moments [97]

$$(a) \theta_{aa} = -1.39 \times 10^{-26} \text{ esu cm}^2$$

$$(b) \theta_{bb} = -0.70 \times 10^{-26} \text{ esu cm}^2$$

$$(c) \theta_{cc} = 2.09 \times 10^{-26} \text{ esu cm}^2$$

The three principal infrared bands of ozone are:  $\tilde{\nu}_1 = 1135 \text{ cm}^{-1}$ ,  $\tilde{\nu}_2 = 716 \text{ cm}^{-1}$  and  $\tilde{\nu}_3 = 1089 \text{ cm}^{-1}$  [98]. The Raman spectrum of ozone gives  $\tilde{\nu}_1 = 1103 \text{ cm}^{-1}$  and  $\tilde{\nu}_2 = 702 \text{ cm}^{-1}$  [99]. The absorption cross sections [100] and absorption spectra [101, 102] of ozone in the visible and ultraviolet regions have been reported: There are three major regions in the absorption spectrum, the strong Hartley band from 200 nm to 300 nm, the Huggins band from 300 nm to 350 nm, and the weak Chappuis band from 400 nm to 750 nm. In the visible region (Chappuis band), ozone displays a diffuse absorption band centered at approximately 600 nm, an absorption cross section  $\sigma = 489 \times 10^{-20} \text{ cm}^2$ , and a molar absorptivity of  $2.94 \text{ L cm}^{-1} \text{ mol}^{-1}$  [103]. In

the ultraviolet (UV) region (Hartley band), the spectrum has a single broad absorption centered at 254 nm approximately. At this wavelength and 273 K, the absorption cross section is  $\sigma = 1147 \times 10^{-20} \text{ cm}^2$ . The molar absorptivity at 260 nm and 298 K is  $2930 \text{ L cm}^{-1} \text{ mol}^{-1}$  [103]. The Hartley and Chappuis bands are symmetric, whereas the Huggins band is a decreasing shoulder region of the Hartley band.

### 1.5.2 Ozone as oxidizing agent

Ozone is a stronger oxidizing agent than molecular oxygen or hydrogen peroxide and reacts with most substances at room temperature [104]. It has a standard reduction potential of 2.07 V [105]. This decomposition reaction occurs spontaneously given the ozone molecule instability.

As discussed before, transition metal hexacyanocobaltates with molecular formula:  $\text{M}_3[\text{Co}(\text{CN})_6]_2$  ( $\text{M} = \text{Mn}, \text{Fe}, \text{Co}, \text{Ni}, \text{Cu}$ ); have  $\text{M}^{2+}$  metallic centres with heterogeneous chemical environments. When dehydrated, those cations have unsaturated coordination spheres that make them specific adsorption sites, favouring the dipole–dipole interaction with ozone molecules. Oxidation–reduction potentials for those exposed metal sites vary depending on the electronic configuration they have in the lattice. However, in order to estimate oxidation processes with ozone, standard oxidation–reduction potentials (measured at 298 K, 1 atm, and with 1 M solutions) become a useful tool. Due to the way they are determined, they represent an overestimated reference to predict oxidative processes.

Oxidation-reduction potentials for the above-mentioned transition metals are showed in table Table 1.1. A quick comparison with ozone standard reduction potential suggest that all mentioned metals can be oxidized by ozone, except copper. The copper case is supported by experimental evidence discussed in section 5.1.

## 1.6 Post-synthesis modification of hexacyano-metallates with ozone.

### 1.6.1 Oxidation of ferrocyanides

Studies on ferrocyanides prototype  $\text{Fe}_4[\text{Fe}(\text{CN})_6]_3 \cdot n\text{H}_2\text{O}$  (IPB) samples, after being subjected to interaction with ozone, showed evidence of the internal

Table 1.1: Oxidation-Reduction potentials for transition metal cations.

Element	Couple	Potential (V) <sup>*</sup>
Mn	Mn <sup>2+</sup> / Mn <sup>3+</sup>	-1.488
	Mn <sup>2+</sup> / Mn <sup>4+</sup>	-1.23
	Mn <sup>3+</sup> / Mn <sup>4+</sup>	-1.652
Fe	Fe <sup>2+</sup> / Fe <sup>3+</sup>	-0.771
Co	Co <sup>2+</sup> / Co <sup>3+</sup>	-1.95
Cu	Cu <sup>2+</sup> / Cu <sup>3+</sup>	-2.3

<sup>\*</sup>Taken from reference [106].

cation oxidation (Fe<sup>2+</sup> to Fe<sup>3+</sup>) [107]. The O<sub>3</sub> output as a function of contact time in the reactor shows that IPB oxidation is the dominant mechanism for ozone decomposition. The oxidation is corroborated by comparing IR spectra before and after post-synthesis modification. The spectrum of the (IPB) has a characteristic band  $\nu_{CN}$  at  $\tilde{\nu}=2078\text{ cm}^{-1}$ , and after being exposed to ozone an additional intense band at  $\tilde{\nu}=2172\text{ cm}^{-1}$  is observed. This band is associated to Fe<sup>2+</sup> oxidation to Fe<sup>3+</sup>. The product is unstable: over time, IR bands change their relative intensity leading to the total disappearance of the characteristic band of Fe<sup>3+</sup> after 1440 h, and the material returns to its original configuration, as is evidenced by the corresponding spectrum. X-ray diffraction of ozonized PB did not show any indication of a change in spatial group symmetry which indicates that ozone molecules can reach active reaction sites without collapsing the lattice.

The evolution of the quadrupolar splitting in Mössbauer spectra for ozonized PB, suggests that water molecules participate in the oxidation process following the global reaction [107]:



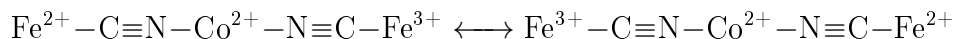
The excess of O<sub>3</sub> reacts with the OH<sup>-</sup> ions causing a chain reaction that leads to the formation of the species O<sub>2</sub><sup>-</sup>, O<sub>3</sub><sup>-</sup>, HO<sub>2</sub><sup>-</sup> and of the free radicals OH<sup>•</sup> and OH<sub>3</sub><sup>•</sup>.

The oxidation of a wide variety of ferrocyanides [Fe(CN)<sub>6</sub>]<sup>4-</sup> after ozone exposure was studied by Reguera *et al.* [108] using IR and Mössbauer spectroscopies. Structural changes were evaluated from X-ray diffraction analysis.

For external cations Na<sup>+</sup>, K<sup>+</sup>, Co<sup>2+</sup>, Ni<sup>2+</sup>, Cu<sup>2+</sup>, Ga<sup>3+</sup>, In<sup>3+</sup>, Mn<sup>2+</sup>, Sm<sup>3+</sup>K<sup>+</sup>, Ho<sup>3+</sup>K<sup>+</sup> the study of IR spectra [108] showed that after being

exposed to  $O_3$ , the characteristic bands  $\nu_{CN}$  moved exclusively to the characteristic values of their corresponding ferricyanides in all but the last three cases. This displacement is associated with the oxidation of the internal cation  $Fe^{2+}$  to  $Fe^{3+}$ . The comparison of Mössbauer spectra between the oxidation products and the corresponding ferricyanides shows that the magnitude variation of the quadrupole splitting ( $\Delta$ ) is significantly different, with the exception of  $Na^+$ ,  $Sm^{3+}$  and  $Ho^{3+}$  compounds; being greater for the ozonized samples. This increase can be explained by a change in the relative population of  $t_{2g}$  levels due to the loss of the water molecules of crystallization as a consequence of the reaction with the ozone. In addition, the presence of charged species and free radicals produced during ozonization may add a certain anisotropy around the orbitals  $d_{xy}$ ,  $d_{xz}$  and  $d_{yz}$ ; modifying the value of  $\Delta$ . X-ray diffraction experiments indicate that the oxidation products have the same unit cells reported for the corresponding ferricyanides, except for Mn. In this case, the diffraction pattern corresponding to the product of the ozonization of  $Mn^{2+}$  ferrocyanide had low crystallinity, and the unit cell parameter could not be determined [108].

In terms of stability, the ferricyanides obtained by the ozonation of the parent compounds tend to reduce with time. However, the rate at which this occurs, depends strongly on the external cation and structural similarities between the ferricyanides and ferrocyanides of the cation in question. For this reason, the  $K^+$  and  $Mn^{2+}$  ferricyanides resulting from oxidation remain stable. The reduction of the  $Co^{2+}$  ferricyanide produces a mixed state that remains stable with an average structure:



Of particular importance for this work are Mn and Co ferrocyanides. Their ozonation provides important information to predict Mn and Co hexacyanides oxidation. In Mn ferrocyanide case ( $Mn_2Fe(CN)_6$ ), ozonation leads to the oxidation of both metallic cations:  $Fe^{2+}$  is oxidized to  $Fe^{3+}$  and  $Mn^{2+}$  is oxidized to  $Mn^{3+}$  and  $Mn^{4+}$  [109]. The band  $\nu_{CN}$  in manganese ferrocyanide, located at  $\tilde{\nu} = 2066 \text{ cm}^{-1}$  disappears and it is replaced by three new bands at  $\tilde{\nu} = 2148, 2162$  and  $2176 \text{ cm}^{-1}$  corresponding to compounds with the following cations:  $Mn^{2+}Fe^{3+}$ ,  $Mn^{3+}Fe^{3+}$  and  $Mn^{4+}Fe^{3+}$  [108]. Previous investigations of Co ferrocyanide ( $Co_2Fe(CN)_6$ ) indicated that IR spectra for ozonized compound shows a band at  $\tilde{\nu} = 2125 \text{ cm}^{-1}$  with weaker bands at  $\tilde{\nu} = 2165$  and  $2190 \text{ cm}^{-1}$ , assigned to  $Co^{2+}Fe^{3+}$  and  $Co^{3+}Fe^{3+}$  respectively [110]. The intense band can be assigned to an intermediate complex

of the form  $\text{Fe}^{2+}-\text{C}\equiv\text{N}-\text{Co}^{2+}-\text{N}\equiv\text{C}-\text{Fe}^{3+}$ , as suggested by the results of the Mössbauer spectra.

### 1.6.2 Ozonization of Mn and Co ferricyanides

These compounds are treated in more detail because of their structural similarities with materials being studied in this thesis. Their stoichiometry ( $\text{M}_3[\text{Fe}(\text{CN})_6]_2$ ;  $\text{M} = \text{Mn}, \text{Co}$ ) is the same as in Mn and Co hexacyanocobaltates and they also crystallize in the  $Fm\bar{3}m$  space group with random vacancies.

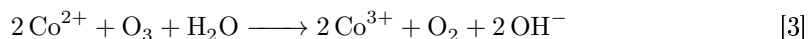
Ozonization of  $\text{Mn}^{2+}\text{Fe}^{3+}$  leads to the formation of  $\text{Mn}^{3+}$  and  $\text{Mn}^{4+}$  ferricyanides. This can be observed by comparing their corresponding IR spectra. The band  $\nu_{\text{CN}}$  in  $\text{Mn}^{2+}\text{Fe}^{3+}$  at  $\tilde{\nu} = 2148 \text{ cm}^{-1}$  disappears and is replaced by two new bands at  $\tilde{\nu} = 2162$  and  $2176 \text{ cm}^{-1}$  corresponding to the compounds  $\text{Mn}^{3+}\text{Fe}^{3+}$  and  $\text{Mn}^{4+}\text{Fe}^{3+}$  respectively [109]. The increase  $\Delta\nu = 16 \text{ cm}^{-1}$  is similar to that corresponding to the transformation of  $\text{Co}^{2+}\text{Fe}^{2+}$  to  $\text{Co}^{2+}\text{Fe}^{3+}$ . The IR spectrum for cobalt ferricyanide after being exposed to ozone shows a new frequency band at  $\tilde{\nu} = 2200 \text{ cm}^{-1}$ , higher than that of the initial compound, which is at  $\tilde{\nu} = 2160 \text{ cm}^{-1}$ . This corresponds to the formation of  $\text{Co}^{3+}\text{Fe}^{3+}$ .

X-ray diffraction measurements were conducted just for  $\text{Mn}^{2+}\text{Fe}^{3+}$ . Its X-ray pattern shows a predominant phase with a cubic structure similar to that of the initial compound but with a smaller cell parameter ( $\Delta a = 0.142(1) \text{ \AA}$ ) [109]. This can be explained by the formation of the  $\text{Mn}^{3+}$  and  $\text{Mn}^{4+}$  cations which results in a contraction of the Fe-CN-Mn-NC-Fe lattice. When  $\text{Mn}^{2+}$  is oxidized, its electron density decreases, favouring the  $\sigma$  donation from  $\text{C}\equiv\text{N}^-$  ligands and reducing the  $\pi$  back-bonding donation from the metal d orbitals. Both effects strengthen the Mn-N bond and the  $\text{C}\equiv\text{N}$  triple bond, reducing the length of the Fe-CN-Mn-NC-Fe chain.

In the Mössbauer spectrum for  $\text{Mn}^{2+}\text{Fe}^{3+}$ , the isomeric shift decreases slowly but monotonously with increasing manganese cation charge. This indicates a polarization of the electrons of the CN bond towards  $\text{Mn}^{2+}$  away from the  $\text{Fe}^{3+}$  cation, which facilitates the expansion of the electron cloud of the iron atom [111]. The quadrupole splitting shows more pronounced effects, changing from  $0.26 \text{ mm s}^{-1}$  for  $\text{Mn}^{2+}$  to  $0.94 \text{ mm s}^{-1}$  for  $\text{Mn}^{3+}$  and diminishing to  $0.55 \text{ mm s}^{-1}$  for  $\text{Mn}^{4+}$ . The large value of the quadrupole splitting is connected with the well known Jahn-Teller effect of  $\text{Mn}^{3+}$  compound, whose incomplete  $t_{2g}$  levels seek stabilization by distortion of the octahedral sym-

metry. The asymmetric effect is transmitted to strongly bound CN ligands and distorts the environment of the central  $\text{Fe}^{3+}$  cation.

In the  $\text{Co}^{2+}\text{Fe}^{3+}$  case, the ozonized product has a lower isomeric shift and a quadrupolar splitting higher than the initial compound. The first can be explained by the fact that the  $\text{Co}^{3+}$  cation attracts the electrons of the CN group, producing the electron cloud expansion of  $\text{Fe}^{3+}$ , reducing the shielding effect of the orbital electrons and increasing the effective charge of the nucleus of  $\text{Fe}^{3+}$ . The increase in quadrupolar cleavage can be attributed to an increase in the electrical asymmetry of the environment of  $\text{Fe}^{3+}$  due to the presence of  $\text{OH}^-$  ions which are formed by the reaction of ozone with the water molecules coordinated to the external cation in the crystal structure [42].



Compounds formed as a result of the oxidation of Mn ferricyanide are not stable [109]. In 15 days all the cations of the  $\text{Mn}^{4+}$  species had been reduced to  $\text{Mn}^{3+}$  (40%) and  $\text{Mn}^{2+}$  (60%). After one year only  $\text{Mn}^{2+}$  cations were reported. The stability of Co ferricyanide has not been discussed in the literature.

The studies described above do not assess to what extent the change in the oxidation state of the affected metals in the described structures modifies their gas retention capacities, nor to what extent the oxidation of the metals affects the corresponding adsorption enthalpies. In this work, these points will be studied in Chapter 5.

## 1.7 X-ray photoelectron spectroscopy (XPS) analysis

In XPS, the surface of a sample is irradiated with photons of characteristic energy (usually Mg  $K_\alpha$  radiation). These photons directly interact with core electrons of the sample atoms [112]. As a result, ionized states are created, and a photoelectron is emitted with a kinetic energy given approximately by the difference between the photon energy and the binding energy. The measured photoelectron spectrum is therefore a direct indication of the binding energies of the different atomic electron levels and is often directly calibrated in eV. The inelastic mean free path of the photoelectrons is determined by

the probability to suffer an energy loss and the attenuation length, taking into account inelastic and elastic scattering, is determined by the probability of the photoelectron to be received by the electron energy analyser.

The popularity of XPS is based on the fact that this technique can:

1. Identify and quantify the elemental composition of the outer 10 nm or less of any solid surface with all elements from Li to U detectable <sup>3</sup>. Elements H and He are not detectable due to their extremely low photoelectron cross sections and the fact that XPS is optimized to analyse core electrons.
2. Reveal the chemical environment of the respective element, that is, the speciation of the respective elements observed.
3. Obtain the above information with relative ease and minimal sample preparation.

In this work, XPS experimental results can provide information about changes in oxidation states of the exposed metal sites after post-synthesis modification with ozone. This information can be extracted qualitatively through changes in elemental composition and the chemical environment of the ozonized samples. This changes are observed experimentally in the form of chemical shifts of photoelectron peak energy as well as changes in the shapes of this peaks, and the modification of the valence band spectra.

### 1.7.1 Basic physical principles

Photoelectron emission three stages process is described as follow:

1. X-rays interact with the electrons in the atomic shell and photoelectrons (and Auger electrons) are generated.
2. Part of these electrons move through the solid to the surface and are subject to various scattering processes (those which are inelastically scattered creating the background).
3. Electrons reaching the surface are emitted in a vacuum (after surmounting the work function threshold). An X-ray with characteristic energy  $h\nu$  transfers its energy to a core electron with binding energy  $E_b$  (with

---

<sup>3</sup>This is on the assumption that the element of interest exists at  $> 0.05$  atomic percent.

reference to the Fermi level,  $E_F$ ). The kinetic energy of that electron in vacuum is given by  $h\nu - E_b - \Phi_S$ , where  $\Phi_S$  is the work function of the sample and  $\Phi_A$  the work function of the analyzer. The kinetic energy  $E_{kin}$  measured for the analyzer is given by

$$\begin{aligned} E_{kin} &= h\nu - E_b - \Phi_S - (\Phi_A - \Phi_S) \\ E_{kin} &= h\nu - E_b - \Phi_A \\ E_b &= h\nu - E_{kin} - \Phi_A \end{aligned} \tag{1.8}$$

Equation (1.8) is fundamental for qualitative XPS analysis. Because the sample work function cancels, the photoelectron energy is known and the analyzer work function is constant, the kinetic energy determines the binding energy and vice versa.

## 1.7.2 Qualitative analysis of the XPS spectra: Chemical state identification

Chemical state identification using XPS has become an experimental routine technique for most elements in the periodic table. There are several binding energy databases, as NIST Database [113] or Handbook of XPS [114] able to provide sufficient data for the chemical state determination for uncomplicated (single peak) spectra. However, the transition metal  $2p$  spectra give a number of complications that these databases do not adequately address, specifically, shake-up and plasmon loss structures, and multiplet splitting, all of which can complicate identification of the chemical states present. For example, fitting parameters such as peak widths and asymmetries, which are vital for curve fitting of complex, mixed metal and metal oxide systems, are not reported in these databases. Importantly, some of the transition metal electronic states give rise to significant intensity components in their  $2p$  spectra due to multiplet splitting and these contributions are not normally considered [115].

### Multiplet splitting

Multiplet splitting arises when an atom contains unpaired electrons. In these instances when a core electron vacancy is formed by photoionization there can be coupling between the unpaired electron in the core with the unpaired outer shell electron. At the most fundamental level, multiplet splitting arises from the fact that an electron can have one of two spins ( $m_s = \pm\frac{1}{2}$ ), which

in turn generates an specific magnetic field. If two unpaired electrons exist (valence and core), the spin component of one of them can be aligned or opposed to the magnetic field vector generated by the other. This results in a splitting in energy of the associated orbitals and thus the binding energy ( $E_b$ ) of the core level from which the initial electron emanated from. This can create a number of final states, which will manifest in the photoelectron spectrum [114]. Unlike spin orbit splitting, multiplet splitting can affect the binding energy of any electron from any orbital, even s orbitals.

Since valence levels play a critical role in multiplet splitting, this form of splitting is sensitive to the local chemical environment as well as any core hole induced rearrangement effects introduced. The former arises from the fact that valence electrons are involved in bonding, while the latter explains why both paramagnetic and diamagnetic ions can exhibit multiplet splitting ( $\text{Co}^{2+}$  and  $\text{Co}^{3+}$  are two examples). Multiplet splitting can also alter the apparent separation induced by spin orbit splitting. As an example, the apparent spin orbit splitting of the  $\text{Co}_{2p}$  doublet varies from 14.97 eV noted from the metal to 16.0 eV noted in  $\text{Co}_2\text{O}_3$  [116]. Lastly, metals can also exhibit multiplet splitting due to core hole-induced localization of valence electrons.

The multiplet splitting energy separation ( $E_{\text{mult}}$ ) on a the core-level photoelectron emission can be shown, via vectorial analysis, to scale as:

$$E_{\text{mult}} = \frac{2(S_V + s_C) + 1}{2l + 1} K_{\text{mult}} \quad (1.9)$$

where:  $S_V$  is the total 3d level spin of the photoelectron emitting atom/ion,  $s_C$  is the core level spin and  $K_{\text{mult}}$  is the multiplet splitting exchange integral [117]. This integral increases as the interacting core electron  $E_b$  decreases, or in other words, as the unpaired core and valence electrons move toward each other. Since the extent of splitting depends on the exchange integral, this and the value of  $E_{\text{mult}}$  can also be related to the  $E_b$  of the level affected by multiplet splitting.

As can be seen from equation (1.9), the splitting pattern is a function of the core level  $l$ . That is, photoelectrons from s orbitals result in doublets, p orbitals in triplets, d orbitals in quintuplets, and so forth. Similar trends can be derived empirically or otherwise for other levels and other transition metal ions. In addition, the first row transition metal ions with less than half-filled 3d orbitals exhibit a splitting of the main photoelectron peak, while those with more than half-filled 3d orbitals exhibit a splitting of the satellite peak.

When spin orbit splitting is in effect, only the spin orbit peak with the higher  $J$  value suffers multiplet splitting.

Multiplet splitting degeneracy  $D_{\text{mult}}$  can be expressed via the same relation used to describe spin orbit splitting degeneracy if all spins are effectively accounted for. Although normally represented using  $J$  [118], this is represented for  $l = 0$  levels using  $S_V$  and  $s_C$  to be consistent as:

$$D_{\text{mult}} = 2(S_V \pm s_C) + 1 \quad (1.10)$$

$$D_{\text{mult}} = 2J + 1 \quad (1.11)$$

The interaction of an  $s$  core level with a single valence electron will therefore result in a 3:1 degeneracy. Likewise, two valence electrons of the same spin will yield a 2:1 degeneracy, and so forth.

In the first transition series, low-spin  $\text{Fe}^{2+}$ , low spin  $\text{Ni}^{2+}$ ,  $\text{Cr}^{6+}$  and  $\text{Mn}^{7+}$  species do not have unpaired  $d$  electrons and thus will not exhibit multiplet splitting.  $\text{Cr}^{3+}$ ,  $\text{Mn}^{2+}$ ,  $\text{Mn}^{3+}$ ,  $\text{Mn}^{4+}$ ,  $\text{Mn}^{6+}$ , high-spin  $\text{Fe}^{2+}$ ,  $\text{Fe}^{3+}$ ,  $\text{Co}^{2+}$ ,  $\text{Co}^{3+}$ , high spin  $\text{Ni}^{2+}$  and  $\text{Ni}^{3+}$  species all contain unpaired  $d$  electrons and therefore exhibit multiplet structures [119].

In MnHCC and CoHCC (materials studied in this thesis), the inner metal cation  $\text{Co}^{3+}$  is found to be always in a low spin (LS) state, while the outer cation ( $\text{Co}^{2+}$  or  $\text{Mn}^{2+}$ ) is in a high spin (HS) state. The coordination bond  $\text{Co}^{3+}\text{-C}$  ( $\text{Mb}^{2+}\text{-N}$ ), is formed by a  $\sigma$  donation from the  $\text{CN}^-$  ligands to the metal and it is stabilized by a  $\pi$  back-bonding donation from the  $d$  orbitals of the metal to the  $\pi$  orbitals of the ligand. The energy degeneracy of the five  $d$  orbitals is broken due to their interaction with the  $\sigma$  bonds of the strong ligands  $\text{CN}^-$ . Two of the  $3d$  orbitals ( $e_g$ :  $3d_{x^2-y^2}$  and  $3d_{z^2}$ ) of the metal ion, point directly toward the  $\sigma$  orbitals from the six  $\text{CN}^-$  ions, increasing the electronic repulsion in comparison with the other three  $d$  orbitals ( $t_{2g}$ :  $3d_{xy}$ ,  $3d_{xz}$ , and  $3d_{yz}$ ), which lie between the direction of the  $\sigma$  orbitals. As a consequence, the  $e_g$  orbitals have a higher energy than the  $t_{2g}$ .

The LS configuration is achieved because each inner cation  $\text{Co}^{3+}$  has a complete octahedral coordination sphere ( $\text{Co}^{3+}(\text{CN})_6$ ), the cyano groups are strong field ligands and because the coordination bond  $\text{Co}^{3+}\text{-C}$  has mainly a covalent character. In this case, the splitting energy exceeds the pairing energy and the electrons will fill the  $d$  orbitals  $t_{2g}$  before any electrons are placed on the higher energy orbitals  $e_g$ .

To analyse the HS configuration of the  $\text{Mn}^{2+}$  and  $\text{Co}^{2+}$  ions, it must be considered that Mn-N bonds have mainly an ionic character. As a result,

the  $\pi$  back-bonding donation from the metal to the ligand is reduced, also reducing the electronic repulsion between the metal  $e_g$  orbitals and the  $\sigma$   $\text{CN}^-$  molecular orbitals. Therefore, the splitting energy is lower than the pairing energy and the electrons will fill  $d$  orbitals as if they were degenerate. The structural disorder also contribute to the HS configuration because the  $\text{Mn}^{2+}$  and the  $\text{Co}^{2+}$  ions have heterogeneous coordination environments ( $(\text{Ma}^{2+}(\text{NC})_n(\text{H}_2\text{O})_{6-n})$ ) and in the  $\text{Ma}-\text{H}_2\text{O}$  bonds prevail a dipolar interaction.

### Multiplet splitting in Mn cations

Manganese presents a serious challenge for both qualitative and quantitative analysis because it has six stable oxidation states (0, 2+, 3+, 4+, 6+ and 7+), three of them with significant multiplet splitting (2+, 3+, 4+), one oxidation state with less defined splitting or broadening (6+), and overlapping binding energy ranges for these multiplet splitting structures [120]. Previous work conducted by Oku *et al.* [121] shows a series of spectra of a variety of manganese oxide species. These spectra showed excellent peak structure, useful for qualitative assignment of Mn oxidation states. Some discussion of multiplet splitting was presented with some prominent peaks binding energy values reported, but no attempt at fitting of these structures was made. A thin layer of nickel metal deposited on the surface of the samples is used for charge correction.

Nesbitt and Banerjee use curve fitting of  $2\text{Mnp}_{3/2}$  spectra [122], based on the multiplet splitting proposed by Gupta and Sen [119], to interpret  $\text{MnO}_2$  precipitation and reactions on birnessite ( $\text{MnO}_{1.7}(\text{OH})_{0.25}$  or  $\text{MnO}_{1.95}$ ) mineral surfaces [123–125]. These papers provide excellent detail of FWHM values, multiplet splitting separations and peak weightings for easy reproduction of their curve fitting procedure. Binding energies are quoted uncorrected for charging and the apparent measured C1s charge reference of 284.24 eV can only be found in one paper [124]. In the earlier publication [122], the authors include a small satellite peak approximately at 645.5 eV in their fitting for MnO, but this is not discussed in later publications. Fitting parameters are based on standard spectra of MnO, natural manganite ( $\text{MnOOH}$ ).

These fittings, with binding energies corrected to the apparent C1s at 284.8 eV, were modified by latter work of Biesinger *et al.* [120] to better fit new experimental data. Their results are presented in Table 1.2 with additional information of peak parameters for:  $\text{Mn}_2\text{O}_3$ ,  $\text{K}_2\text{MnO}_4$ ,  $\text{KMnO}_4$ ,

Table 1.2:  $2\text{Mnp}_{3/2}$  spectral fitting parameters: binding energy (eV), percentage of total area (%), FWHM at 10 eV pass energy, and spectral component separation (eV). Taken from reference [120].

	Mn(0) Metal (eV)	Mn <sup>2+</sup> MnO (eV)	Mn <sup>3+</sup> Mn <sub>2</sub> O <sub>3</sub> <sup>b</sup> (eV)	Mn <sup>3+</sup> MnOOH <sup>c</sup> (eV)	Mn <sup>4+</sup> MnO <sub>2</sub> (eV)	Mn <sup>4+</sup> MnO <sub>2</sub> <sup>d</sup> (eV)	Mn <sup>6+</sup> K <sub>2</sub> MnO <sub>4</sub> (eV)	Mn <sup>7+</sup> KMnO <sub>4</sub> (eV)
FWHM	0.74	1.21	1.65	1.34	0.84	0.92	1.31	0.98
Peak 1	638.6	640.2	640.8	641.0	641.9	641.8	643.8	645.5
%	87.0	24.0	18.9	24.0	41.7	21.0	100	100
Peak 2	639.6	641.1	641.9	641.7	642.7	642.7	—	—
$\Delta\text{Peak}_{2-1}$ <sup>a</sup>	1.00	0.97	1.10	0.70	0.86	0.87	—	—
%	13.0	27.8	44.5	24.0	26.5	27.4	—	—
Peak 3	—	642.1	643.1	642.5	643.4	643.5	—	—
$\Delta\text{Peak}_{3-2}$	—	0.93	1.27	0.81	0.70	0.75	—	—
%	—	22.1	25.3	27.8	15.5	16.1	—	—
Peak 4	—	643.0	644.6	643.5	644.2	644.3	—	—
$\Delta\text{Peak}_{4-3}$	—	0.95	1.50	1.02	0.75	0.81	—	—
%	—	12.5	8.5	17.5	9.1	8.9	—	—
Peak 5	—	644.2	646.2	644.9	645.0	645.2	—	—
$\Delta\text{Peak}_{5-4}$	—	1.14	1.62	1.37	0.85	0.91	—	—
%	—	4.7	3.1	6.7	4.9	4.6	—	—
Peak 6	—	645.9	—	—	646.0	646.2	—	—
$\Delta\text{Peak}_{6-5}$	—	1.75	—	—	1.00	1.03	—	—
%	—	9.1	—	—	2.5	2.1	—	—
Space group	217	225	206	14	—	136	62	62
Mn Coord.	8	6	6	6	—	6	4	4

<sup>a</sup> Binding energies are significant to 0.1 eV but an additional figure is added because energy splitting are much more accurate than the absolute binding energies. <sup>b</sup>  $\alpha$  phase. <sup>c</sup> Manganite. <sup>d</sup> Pyrolusite.

and pyrolusite ( $\text{MnO}_2$ ).

It is important to consider that assigned peak positions on spectra depend of the energy calibration method whilst the relative position of the peaks are related to each other by the local electric field around the atoms, which is characteristic of each sample. This local electric field breaks the energy degeneration of electron states (stark effect) and the energetic gap between them depends of the field intensity. Due to the quantum nature of electric interaction at the atomic scale, the photons beam directed to the sample during the experiment create a stationary excited state that makes changes on external electric field negligible. For an stable electric field, multiplet energy splitting depends mainly of the material electric properties. In hexacyanocobaltates,  $\text{Mn}^{\text{II}}$  and  $\text{Co}^{\text{II}}$  cations are bonded to nitrogen as described earlier.

<sup>3</sup>Full Width at Half Maximum

This bond is mostly ionic in nature as it happens in oxides. This similarity creates the possibility to use manganese and cobalt oxides XPS data as a base reference to study the multiplet splitting in MnHCC and CoHCC.

### Multiplet splitting in Co cations

There are apparently few examples of good quality high resolution  $\text{Co}2p_{3/2}$  spectra presented in the literature. Fitting appears to be inconsistent and the approach to the analysis of the spectral changes reported is basically qualitative. Fitting of a broad main peak combined with a portion of the satellite structure has been one approach [126,127] although fitting parameter details are not presented in enough detail to emulate. Recent work [128] has clarified the position and type of plasmon loss structure associated with the Co metal (and CoP, cobalt phosphide) spectrum<sup>4</sup>. The Co metal spectrum is fitted with an asymmetric main peak and two plasmon loss peaks at 3.0 eV and 5.0 eV above the main peak, which constitute the surface and bulk plasmons, respectively, with FWHM values of 3.0 eV in both cases.

Results for CoO were analyzed by Biesinger *et al.* [120] and show significantly better resolution than previous work using non-monochromatic sources [129–132] and/or older spectrometers [133]. Previous published databases [114,115] showed inconsistencies related with the peak shapes apparently due to the oxidation of the CoO surface to  $\text{Co}_3\text{O}_4$ , even though the bulk powder XRD spectrum showed only CoO. Attempts to reduce this surface oxide by heating the sample to 950 °C (4h) under argon [120] were unsuccessful. A second sample purchased from the same supplier contained larger lumps of the compound that when analyzed gave spectra that were in better agreement with previous literature results.

Co metal, CoO,  $\text{Co}(\text{OH})_2$  and  $\text{Co}_3\text{O}_4$  spectral fitting parameters are presented in Table 1.3. Fitting parameters for CoOOH from a fit of a digitized spectrum from the recent work of Yang *et al.* [134] are also presented. The binding energy overlap of the various oxide and hydroxide forms greatly increase the absolute error in speciation quantification. However, the curve fitting procedures, can be useful for a more meaningful interpretation for a series of similar Co containing samples. A second concern is the overlap of the higher binding energy  $2p_{3/2}$  multiplet or satellite structures of the various oxides and hydroxides with the metal  $2p_{1/2}$  peak at 793.1 eV. This overlap,

---

<sup>4</sup>A plasmon loss is described as a loss of kinetic energy of the photoelectron when it interacts with bound valence electrons, causing them to oscillate.

Table 1.3: Co2p<sub>3/2</sub> spectral fitting parameters: Binding Energy (eV), percentage of total area (%), FWHM values (at 10 eV pass energy) and spectral component separation (eV).

	Co (eV)	CoO (eV)	Co(OH) <sub>2</sub> (eV)	CoOOH (eV)	Co <sub>3</sub> O <sub>4</sub> (eV)
Peak 1	778.1	780.0	780.4	780.1	779.6
%	81.0	46.6	38.1	61.4	40.5
FWHM	0.70	2.23	2.01	—	1.38
Peak 2	781.1	782.1	782.2	781.4	780.9
$\Delta$ Peak <sub>2-1</sub>	3.00	2.10	1.80	1.32	1.30
%	11.0	25.7	26.6	24.5	29.1
FWHM	3.00	2.59	2.60	—	1.55
Peak 3	783.1	785.5	786.0	783.1	782.2
$\Delta$ Peak <sub>3-2</sub>	2.00	3.40	3.79	1.68	1.30
%	8.0	1.6	33.0	5.2	15.2
FWHM	3.00	2.42	4.47	—	1.94
Peak 4	—	786.5	790.4	790.1	785.2
$\Delta$ Peak <sub>4-3</sub>	—	1.00	4.40	7.07	3.00
%	—	26.1	2.4	8.9	8.1
FWHM	—	5.28	2.33	—	4.28
Peak 5	—	—	—	—	789.5
$\Delta$ Peak <sub>5-4</sub>	—	—	—	—	4.30
%	—	—	—	—	7.2
FWHM	—	—	—	—	3.15
Space group	<i>hcp</i>	225	164	166	227
Mn coordination	12	6	6	—	6 <sup>a</sup> , 4 <sup>b</sup>

<sup>a</sup> Co(III). <sup>b</sup> Co(II).

when the metal is present, requires the use of an offset for the higher binding energy background endpoint.

### 1.7.3 Quantitative analysis of XPS spectra

For transition metal spectra with prominent shake-up lines, it is best to include the entire  $2p$  region when measuring peak area [114, p. 25]. For sample that is homogeneous in analysis volume, the number of photoelectrons per second in a specific spectra peak is given by:

$$I = n f \sigma \theta y \lambda A T \quad (1.12)$$

$$n = \frac{I}{f \sigma \theta y \lambda A T} \quad (1.13)$$

$$n = \frac{I}{S} \quad (1.14)$$

where:

$n$  is the number of atoms of the element per  $\text{cm}^3$  of the sample,

$f$  is the X-ray flux in photons/ $\text{cm}^2\text{s}$ ,

$\sigma$  is the photoelectric cross-section for the atomic orbital of interest in  $\text{cm}^2$ ,

$\theta$  is an angular efficiency factor for the instrumental arrangement based on the angle between the photon path and the detected electron,

$y$  is the efficiency in the photoelectric process for formation of photoelectrons of the normal photoelectron energy,

$\lambda$  is the mean free path of the photoelectrons in the sample,

$A$  is the area of the sample from which photoelectrons are detected,

$T$  is the detection efficiency for electrons emitted from the sample, and

$S$  is the atomic sensitivity factor.

Transition metals, specially of the first series, have widely varying and low values of  $y$ , whereas  $y$  for the other elements is rather uniform at about 0.8 eV. Thus, a value of  $S$  determine on one chemical state for a transition metal may not be valid for another chemical state. This effect can be minimized by including shake-up peaks in the area measurement.

Part II  
Methodology

# Chapter 2

## Materials and Methods

This chapter describes experimental recording techniques and data analysis methodologies. Experimental strategy is resumed in figure 2.1. This scheme illustrates: Materials under study, their post-synthesis modification with ozone, and different characterization techniques used to study both as synthesized and modified materials.

### 2.1 Synthesis

MnHCC and CoHCC *powder samples* ( $M_3[Co(CN)_6]_2 \cdot nH_2O$ ,  $M = Mn$  and  $Co$ ) were synthesized mixing 0.05 M aqueous solution of  $K_3[Co(CN)_6]$  (Sigma–Aldrich 12902 ACS 97 %) and  $MnSO_4$  monohydrate (Sigma–Aldrich 221287, ACS 98 %) or  $CoSO_4$  heptahydrate (Sigma–Aldrich C6768, ACS 99 %). The resulting precipitate was aged for a week and separated from the mother liquor by centrifugation. The precipitate was washed at least 5 times with 40 mL of distilled water to remove the accompanying ions and finally air dried. MnHCC *single crystals* were obtained using two different methods in order to study how diffuse scattering shape is influenced by the synthesis media: in water and in gel. The synthesis in a water media was conducted using the saline bridge method [135]. Water solutions of  $MnSO_4$  and  $K_3[Co(CN)_6]$  at 0.1 M were placed in both sides of an **H** tube inside a thermal bath at  $T = 0^\circ C$  (Figure 2.2, left). The bridge was carefully filled with distilled water. Several pale yellow single crystal with edges from 0.1 mm to 0.4 mm were formed after 21 d by the slow interdiffusion of both components. In order to grow single crystals in a gel media (Figure 2.2, right), 5 mL of  $CH_3COOH$

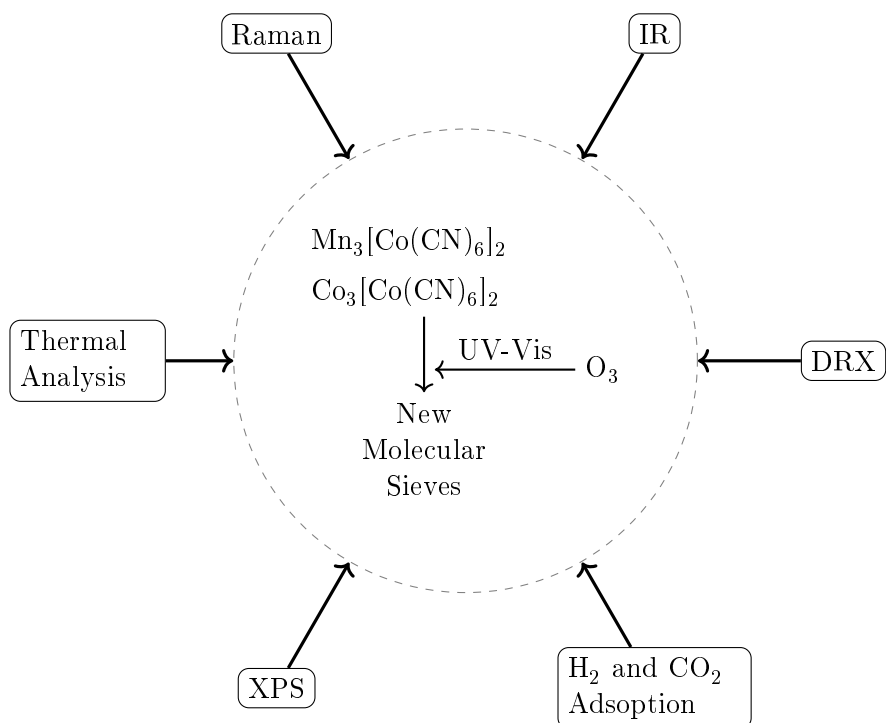


Figure 2.1: Different characterization techniques and post-synthesis modification processes in samples.

2.0 M water solution was deposited in a pipette and 2.5 mL of  $\text{MnSO}_4$  solution at 0.2 M were added while shaking by hand. Finally, 2.5 mL of  $\text{Na}_2\text{SiO}_3$  solution (1.4 M) was added and the resulting mixture was placed in a glass container. A waiting time of 12 h to 24 h was needed to stabilize the mixture. Stabilization was achieved when the mixture becomes solid. To complete the reaction, a  $\text{K}_3[\text{Co}(\text{CN})_6]$  solution (1.2 M) was added to the gel and single crystals were formed by a slow diffusion of this solution into the gel media. Crystal's size varied depending of their height inside the glass container. CoHCC single crystals could not be synthesized in an appropriate size to conduct single crystal X-ray diffraction experiments.

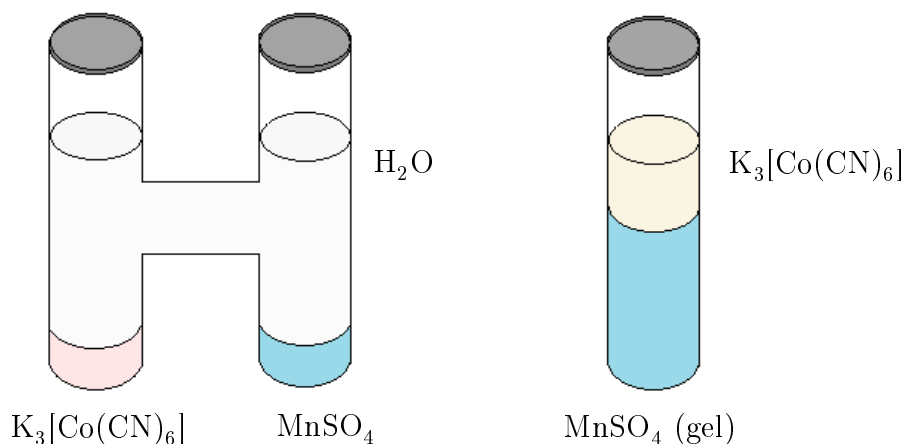


Figure 2.2: Synthesis Methods for MnHCC single crystals. Left: H tube method. Right: Gel Method.

## 2.2 Post-synthesis modification

In order to conduct a post-synthesis modification of oxidation states of open metal sites in manganese hexacyanocobaltate (MnHCC) and cobalt hexacyanocobaltate (CoHCC) frameworks in an environment free of solvents (Specific objective 1), an ozonization system was design and implemented according to the diagram represented at Figure 2.3. This ozonization system was able to modify post-synthesis the powder samples using a flow of ozone enriched dry air in a selective manner (Figure 2.3). Before the post-synthesis modification, the samples were dehydrated in situ in order to facilitate direct

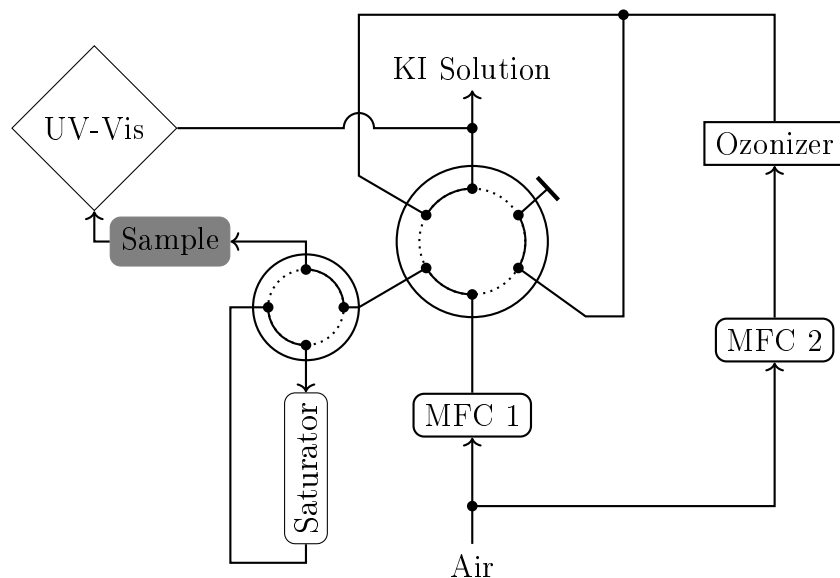


Figure 2.3: Experimental set-up for ozonization. The position A of six way valve (continuous line) is for sample degassing. The position B of six way valve (dotted line) is for sample ozonization with a mixture of air and ozone. The position A of four way valve (continuous line) is a bypass for saturator. Its B position allows methanol saturation of the sample.

interaction between the open metal sites and the ozone molecule. This experimental setup has two mass flow controllers: a Sierra Smart Trak C100L (MFC 1) and an MKS 1179A controlled by Single Channel Power Supply MKS 246C (MFC 2). A Vici E60 six ports two positions switching valve, manually actuated with electric actuator was used to switch the flux during the experiment. A Swagelok SS-43YFS1 four ports two positions switching valve, manually actuated, allowed to switch the flux through the saturator with methanol (methanol HPLC Tecsiquim, 99.8%, CAS# 67-56-1). Additionally, an ozonizer Ozono Carbars with an approximated ozone production of 100 mg/h and an UV-VIS Spectrophotometer Varian CARY 400 with a micro flow cell of a path length UV of 50 mm were used. An extra-dry air tank from INFRA, code 32015, was used to feed the system. The ozone enriched air flow was neutralized using a 1 M solution of KI. All the connections were made with PTFE tubing.

The ozonization system was operated in two different modes: dehydration

and ozonization (Figure 2.3). In position A of switching valve, the sample is dehydrated, while in position B it is ozonized. In the dehydration mode the incoming air flux was split in two fluxes. One of them passed through MFC 1 operating at 100 sccm and through the sample, while the sample was heated at 200 °C. The other part of the dry air flows through MFC 2 operating at 40 sccm and then through the ozonizer, where ozone is produced at a rate of 100 mg h<sup>-1</sup>. The resulting enriched dry air flux goes directly to the neutralization solution without any contact with the sample. After dehydration is completed, the valve is changed manually to position B (Figure 2.3). The dry air that flows through the MFC 1 mixes with the ozone enriched air flux coming from the ozonizer and goes directly to the sample. The volumetric concentration of ozone is determined quantitatively using UV-Vis spectrometer applying the Lambert-Beer law [136]. The ozone molecule in the gas phase has a maximum adsorption at 253.7 nm. Quantitative determination of the volumetric concentration of ozone using the maximum amplitude of the 253.7 nm adsorption band is an absolute measurement with a  $\pm 1\%$  of accuracy [136]. Ozonization stopped when ozone consumption was undetectable. This experimental design allows to control the ozone concentration in the enriched air using the mass flow controllers. The methanol saturation of the sample avoiding exposure to the environment was achieved by switching the four ports valve.

## 2.3 Structural characterization

The characterization techniques used to determine structural changes after the post-synthesis modification with ozone are explained in the following paragraphs. They describe both materials evolution with temperature and solvents desorption (water and methanol), to address the specific objectives 2 and 3.

Structural characterization for hydrated, dehydrated and hydrated ozonized powder samples were performed from XRD data at room temperature using an Empyrean PANalytical diffractometer with monochromatic  $\text{CuK}\alpha$  ( $\lambda = 1.54183 \text{ \AA}$ ) radiation in a  $2\theta$  range from 5° to 90° with a scan speed of 0.11814 ° s<sup>-1</sup> and step size of 0.01°. Hydrated samples were measured using a steel spinner stage, dehydrated samples on a borosilicate glass capillary tube (BGCT) stage and ozonized samples in a steel flat stage. From these diffraction data, unit cell parameters were determined to evaluate volumet-

ric changes due to dehydration and to ozonization separately. Cell parameter determination from obtained XRD powder patterns were carried out with the software FULLPROF, june of 2015 version. Pseudo-Voigt peak shape functions were used to fit diffraction peaks [137]. Dehydration process for MnHCC and CoHCC powder samples were performed under vacuum ( $2.4 \times 10^{-2}$  mbar), at 110 °C and 90 °C respectively, for 17 h inside a BGCT capillary of 0.5 mm. A thermal bath of glycerol was used. The temperature was regulated using a temperature controller. After dehydration the capillary was cut using a blowtorch and the glass was sealed with heat and wax.

Total diffraction experiments were also conducted on hydrated, dehydrated and ozonized powder samples in order to describe bond length changes due to dehydration and ozonization. Borosilicate 0.5 mm capillaries with the samples were placed in a PANalytical Empyrean diffractometer, equipped with a GaliPIX detector and an Ag X-ray source  $\lambda = 0.559421 \text{ \AA}$ . On the incident beam side, diffractometer optics included a focusing mirror,  $0.25^\circ$  divergence and anti-scatter slits and a 0.04 rad soller slit. On the diffracted beam side a 0.04 rad soller slit was used. As data collection strategy, measurements of the scattering pattern were split into the following regions: low  $Q$   $2^\circ$  to  $43^\circ$  for 10 repeat measurements, mid  $Q$   $41^\circ$  to  $90^\circ = 55$  repeats, high  $Q$   $89.5^\circ$  to  $146.3^\circ = 70$  repetitions. The splitting and longer measuring at high angle (large  $Q$ ) was performed because this region is the most important for a good signal in the PDF when it is Fourier transformed. The time per step (degrees) is the same across all 3 regions. However, it is not straightforward to quantify it as we are using a detector in a scanning line mode. Pair distribution function was calculated from PDFgui software [138] using  $D(r)$  formalism.

Changes in bond strength were observed using Infrared and Raman spectroscopy. Infrared spectra were collected from  $\tilde{\nu} = 4000 \text{ cm}^{-1}$  to  $600 \text{ cm}^{-1}$  with a Nicolet FT-IR 6700 Thermo Scientific spectrophotometer, using Attenuated Total Reflection (ATR) technique. Raman spectra were recorded with a Raman-Luminescent microscope Rammics M532 and Olympus CX-41 using a Linear CCD Array detector with a Spatial resolution  $1 \mu\text{m}$  and efficiency of  $7000 \text{ counts mW}^{-1} \text{ s}^{-1}$ . The spectrometer works with a laser wavelength  $532 \text{ nm}$  (power from  $20 \text{ mW}$  to  $30 \text{ mW}$ ) at a spectral resolution from  $5 \text{ cm}^{-1}$  to  $8 \text{ cm}^{-1}$ . The sample was exposed to 200 scans at 20 % of attenuation.

Variations on MnHCC and CoHCC local electric field inside the pores due to oxidation of the metallic centres was characterized using X-ray pho-

photoelectron spectroscopy (XPS).

X-ray photoelectron spectroscopy experiments were performed in an ultra-high vacuum (UHV) system Scanning XPS microprobe PHI 5000 VersaProbe II, with an  $AlK_{\alpha}$  X-ray source ( $h\nu = 1486.6$  eV) and a MCD analyzer. The surface of the samples were not etched. The XPS spectra were obtained at  $45^{\circ}$  to the normal surface in the constant pass energy mode (CAE),  $E_0 = 50$  and  $20$  eV for survey surface and high-resolution narrow scan, respectively. The peak positions were referenced to the background silver  $3d_{5/2}$  photopeak at  $368.20$  eV, having a FWHM of  $0.56$  eV, and C  $1s$  hydrocarbon groups as  $285$  eV, Au  $4f_{7/2}$  en  $84.00$  eV central peak core level position. Elemental composition was determined using atomic sensitivity factors (ASF) [139] peak area of core levels C  $1s$  ( $0.314$ ), O  $1s$  ( $0.733$ ), N  $1s$  ( $0.499$ ), Mn  $2p$  ( $2.688$ ) and Co  $2p$  ( $3.529$ ); corrected by MultiPak PHI software [140]. The XPS analysis deconvolution of spectra were fitted with the program SDP v 4.1 [141]. The deconvolution analysis in binding energy for central peak estimated the uncertain  $5\%$  ( $\pm 0.05$  eV) and a Chi-square value of less than 2.

First principles computational calculations to simulate the valence band in both materials were carried out using Dmol3 [142,143]. Electronic calculations were undertaken by applying the double-numeric quality basis set with polarization functions (dnp). We applied an cutoffof global of  $4.5 \text{ \AA}$ . The exchange correlation interaction was calculated with the generalised gradient approximation using the functional parameterised by Perdew, Burke, and Ernzerhof (PBE) [144]. The convergence threshold for the self-consistent field was  $10 E_h$  to  $6 E_h$ , while the smearing was set to  $0.02 E_h$ . The Brillouin zone has been sampled with a highly converged set of  $k$  points, using grids up to  $2 \times 2 \times 2$  points according to the Monkhorst Pack scheme [145] for all calculations. The unit cells of MnHCC and CoHCC was taken from X-ray data. Partial densities of states (pDOS) were obtained considering the contribution of specific atoms into the total density of states.

Frameworks evolution with temperature on ozonized samples containing water and methanol solvents in MnHCC and CoHCC were determined from thermogravimetric analyses. Thermogravimetric analyses on hydrated and ozonized samples were carried out in a TA Instruments Hi-Res<sup>TM</sup> thermogravimetric analyzer TGA Q5000. The heating rate was dynamically controlled with instrumental resolution of  $5$  and Hi-Res sensitivity of  $1.00$ . The experimental atmosphere was created combining  $10$  ml/min dry nitrogen balance flow and  $25$  ml/min dry air oven purge flow. The mass loss profiles of the

studied samples were analyzed using the software Universal Analysis 2000 v4.5A.

In order to find the law that correlates the vacancies in hydrated and dehydrated phases of MnHCC, experimental diffuse scattering information was needed. To obtain this information, single crystals X-ray diffraction experiments at variable temperatures were conducted in a single crystal diffractometer from Agilent Technologies (Oxford Diffraction) Supernova. A  $\text{MoK}_\alpha$  radiation was used with a resolution of  $0.4 \text{ \AA}$ . A  $2\theta$  range from  $130^\circ$  to  $135^\circ$  was used and a detector Atlas CCD type (Charge-Coupled Device) with 4-axis KAPPA goniometer. Temperature was controlled from 80 K to 500 K using a low-temperature Oxford Cryostream system. The experiment was designed for a total of 44 h, from which X-ray diffraction patterns were collected for 12 h at 100 K, 500 K and again at 100 K. The heating ramp was of  $2 \text{ K min}^{-1}$  and the stabilization time before each measurement was of 30 min. Diffuse scattering information was simulated using Montecarlo algorithm and compared with experimental data in order to find an appropriate spatial configuration for atoms within the structure.

An Additional single crystals X-ray diffraction experiments was conducted at different temperatures to determine thermal expansion coefficients for hydrated, dehydrated and partially dehydrated MnHCC structures. The experiment was designed for 54 h in the same instrument described above. A total of 47 X-ray diffraction measurements were conducted from 100 K to 500 K and the corresponding diffraction patterns were collected within 25 K intervals. The heating ramp was of  $1 \text{ K min}^{-1}$ . For 6 points: 100 K, 300 K, 500 K, 300 K and 100 K; diffraction patterns were collected for 6 h and the stabilization time before each measurement was of 30 min. For the rest, the collection time was 15 min. Experimental strategy is described on Figure 2.4: The crystal was cooled from 275 K to 100 K to improve the diffraction pattern quality with the reduction with temperature of the noise due to thermal motion. Then, the crystal was heated from 100 K to 500 K to ensure complete dehydration. Another cooling process was conducted after that, from 500 K to 100 K in order to compare dehydrated pattern with the hydrated one at the same temperature (100 K). In this way, structural changes can specifically be attributed to the loss of water molecules. Finally the crystal was heated again until 300 K (ambient temperature). From the corresponding diffraction patterns at each temperature, unit cell parameter and unit cell volume were determined and presented in table A.1 it Appendix A. Inspection of the extended range diffraction dataset did not reveal any reflections

violating face-centered cubic (fcc) extinction rules, and the cell parameter was determined using the space group  $Fm\bar{3}m$ . For hydrated, dehydrated and partially dehydrated states, isobaric thermal expansion coefficients were determined and the first two were compared with results from the Pascal software [63].

## 2.4 Adsorption

The effect of manganese and cobalt oxidation states on  $H_2$  and  $CO_2$  retention capacity and on their partial enthalpy of adsorption was evaluated from experimental adsorption data (specific objective 5). The  $H_2$  and  $CO_2$  adsorption isotherms were recorded using a Micrometrics ASAP 2020 analyzer. The experiments were performed in a liquid nitrogen bath at a local atmospheric pressure ( $\approx 77\,981$  Pa) for  $H_2$  and at 273.15 K for  $CO_2$  isotherms. Micromeritics Chiller Dewar option and NESLAB refrigerated bath model RTE7 were combined to guarantee the cryogenic condition for  $CO_2$  isotherms. About 100 mg of samples were degassed for 1 h at a pressure below 1.3 Pa. The degassing temperatures changed according to the temperatures at which the evolution of the solvent ends in the thermogravimetric curves (383 K for original samples, 403 K for  $MnHCCOz$ , and 473 K for  $MnHCCOz$ ). After degassing, the sample tube was back filled with dry nitrogen, transferred to the analysis port and the evacuation was continued for another 12 h at room temperature. Then, the free volume was measured with helium and the samples were degassed again for another twelve hour at room temperature, previous to recording the  $H_2$  adsorption isotherms. After  $H_2$  adsorption isotherms finished, the degassing process at room temperature was repeated in analysis port and  $CO_2$  adsorption isotherm was ran. All isotherms were fitted with a Langmuir–Freundlich type isotherm (equation 4.13) derived from vacancy solution theory in section 4.2. Fitted  $p_{1/2}$  and  $g$  parameters were used to calculate the isosteric heat of adsorption by equation (4.24).

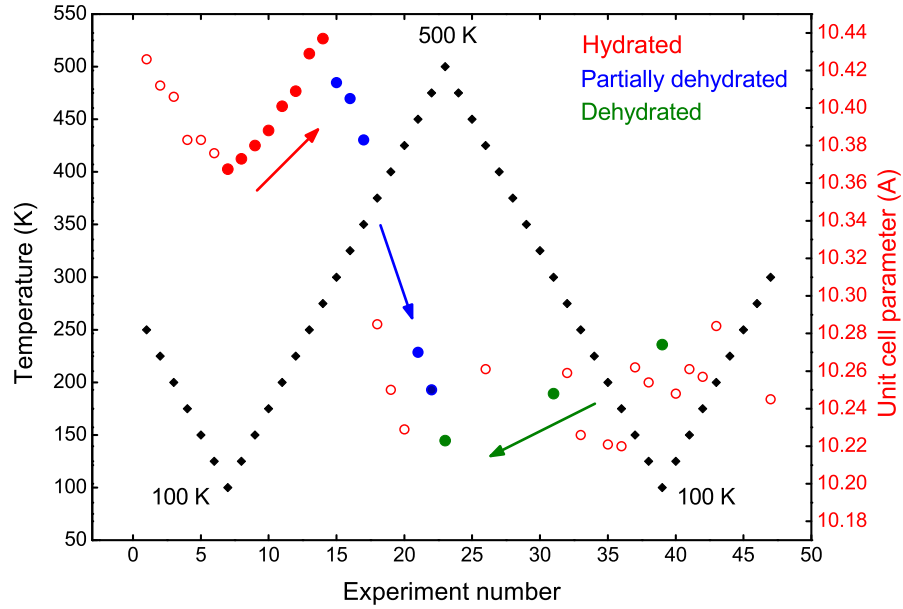


Figure 2.4: Cell parameter *vs.* temperature in MnHCC single crystals. The black points are the temperature values plotted *vs.* the experiment number. The experiment number indicates the evolution of the experiment in time. The coloured points are the values of the unit cell parameter at each experiment number. Points chosen to calculate isobaric thermal expansion coefficient for hydrated phase are highlighted with filled points in red, for the partially dehydrated state in blue, and for dehydrated phase in green. The green point at 500 K was used for both partially dehydrated and dehydrated states. Arrows are directed considering if the cell parameter increases or decreases with temperature.

# Part III

## Results

## Chapter 3

# Structural analysis of Manganese Hexacyanocobaltate

In this chapter, experimental data providing new structural information on MnHCC both hydrated and dehydrated states is presented. The aim is to include local information in the form of diffuse scattering and to characterize the framework evolution in a wide temperature range. The analysis of local structural data can lead to a better description of its structural disorder and hence to a more precise determination of its pore size distribution function. The framework evolution with temperature can provide a description of its interaction with water and other polar solvents. The knowledge of both types of information can greatly improve adsorption computational simulations in a wide range of materials with structural and electrical similarities.

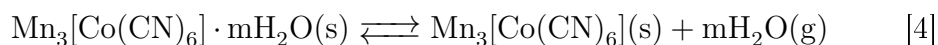
In section 3.1, volumetric changes induced by temperature in MnHCC single crystals are determined from single crystal X-ray diffraction data. Thermal expansion coefficients of hydrated and dehydrated states are reported in addition to the states where the crystal is being dehydrated. In section 3.2, diffuse scattering experimental evidence in MnHCC single crystals synthesized in two different media is presented. The influence of the surrounding media on the crystallographic disorder is discussed. Experimental results show a correlation between vacancies, which implies that vacancy distribution is not random, as it was previously assumed.

## 3.1 Thermal Expansion Coefficient of MnHCC

### 3.1.1 Problem definition

As previously discussed in section 1.3.1, MnHCC has an open framework with different type of pores, which are regularly occupied by physically adsorbed water molecules. Previous reports indicate the framework does not collapse after dehydration [73] and the cell volume decreases as a consequence of the loss of water molecules [22].

On heating, water molecules are reversibly desorbed according to the reaction:



The volume of the solid is affected by both the temperature and the water content. To differentiate the effects of both variables is a major challenge due to the difficulties imposed by water chemical potential control under variable temperature conditions. This is essential to determine isobaric thermal expansion coefficient, a key parameter in the thermodynamic description of the solid.

The aim of this section is to determine the isobaric thermal expansion coefficient of MnHCC in a wide temperature range. The temperature range include the dehydration event, therefore the effect of water molecules on the volume of the material should be considered. To achieve this goal we combine X-ray diffraction of MnHCC single crystals at different temperatures with thermogravimetric analysis.

### 3.1.2 Thermodynamic formulation

The thermodynamic system is delimited by MnHCC single crystal borders. Volumetric changes due to temperature variation are characterized by Gibbs thermodynamic potential because each of their natural variables: temperature ( $T$ ), pressure ( $p$ ) and number of particles of each component ( $n_i$ ), can be controlled at a given time during the experiment.

We are going to analyse the most general case in which the crystal is loosing water. A MnHCC single crystal is an open system in which the framework is able to exchange water molecules with it's environment. Therefore, the crystal can be modelled as a solid solution with two components: the

CHAPTER 3. STRUCTURAL ANALYSIS OF MANGANESE  
HEXACYANOCOBALTATE

---

framework and the solvent, in this case, water. Considering that all experiments were carried out under constant pressure and controlled temperature, the Gibbs potential for this boundary conditions is:

$$dG = -SdT + Vdp + \sum_{i=1}^c \mu_i dn_i \quad (3.1)$$

$$dG = -SdT + Vdp + \mu_f dn_f + \mu_w dn_w \quad (3.2)$$

where subscripts f and w refer to the framework and water respectively. Here  $\mu$  is the chemical potential for each component and the extensive variables  $S$  and  $V$  refer to the crystal entropy and volume. For isobaric conditions ( $dp = 0$ ) and for temperatures below the decomposition temperature of the MnHCC ( $dn_f = 0$ ):

$$dG = -SdT + \mu_w dn_w \quad (3.3)$$

Gibbs potential only depends on temperature and the number of water molecules in the structure. Under these conditions, the volume will be a function of  $T$  and  $n_w(T)$  and the total derivative ( $\frac{dV}{dT}$ ) can be determined using the chain rule:

$$\begin{aligned} V &= V(T, n_w) \\ dV|_p &= \left(\frac{\partial V}{\partial T}\right)_{p, n_w} dT + \left(\frac{\partial V}{\partial n_w}\right)_{p, T} dn_w \\ dV|_p &= \left(\frac{\partial V}{\partial T}\right)_{p, n_w} dT + \left(\frac{\partial V}{\partial n_w}\right)_{p, T} \left(\frac{dn_w}{dT}\right)_p dT \\ \frac{dV}{dT}\Big|_p &= V\alpha(p, n_w) + \left(\frac{\partial V}{\partial n_w}\right)_{p, T} \left(\frac{dn_w}{dT}\right)_p \end{aligned}$$

Solving for the isobaric thermal expansion coefficient ( $\alpha$ ):

$$\alpha(T, n_w) = \frac{1}{V} \left[ \frac{dV}{dT} - \left(\frac{\partial V}{\partial n_w}\right)_{p, T} \left(\frac{dn_w}{dT}\right)_p \right] \quad (3.4)$$

The first term on right side of equation 3.4 ( $\frac{dV}{dT}\Big|_p$ ) is the isobaric rate of change of the crystal volume with temperature. Changes due to the remaining thermodynamic variables in the system are included in this term,

CHAPTER 3. STRUCTURAL ANALYSIS OF MANGANESE  
HEXACYANOCOBALTATE

---

that is why it is represented with a total derivative. This derivative can be experimentally obtained as discussed in section 3.1.3.

The second term  $\left[ \left( \frac{\partial V}{\partial n_w} \right)_{p,T} \right]$  is the rate of volume change due to a change in the crystal chemical composition (in this case water), maintaining isobaric and isothermal experimental conditions. This derivative is very difficult to obtain directly from an experiment. To achieve this goal, the chemical potential of water ( $\nu_w$ ) must be modified at constant temperature and pressure (conjugate variable of  $n_w$  in equation 3.3). To maintain the isobaric conditions able to create a suitable chemical potential gradient (80 kJ mol<sup>-1</sup>), the experiment should be conducted under a controlled atmosphere using an inert gas with nearly zero hydration degree<sup>1</sup>. This type of experiment is very expensive and difficult to conduct successfully. All difficulties mentioned above can be solved by using additional thermogravimetric information as described in the next section.

The last term in equation 3.4  $\left[ \left( \frac{dn_w}{dT} \right)_p \right]$  is the rate of change of the number of water molecules inside the structure with temperature. Taking into consideration that  $n_w$  is only a function of temperature for isobaric conditions, this term is represented as a total derivative, which means that it is valid for any other changes in the system during the experiment.  $\left[ \left( \frac{dn_w}{dT} \right)_p \right]$  can be determined directly from TGA data.

Considering that  $n_w$  decreases with temperature if the crystal is losing water, it is evident that the total number of particles in the system  $n$  also changes with T. Therefore,  $\alpha$  is different at each equilibrium point and it is not a constant but a function of T and  $n_w$ . The mathematical approach suggested in this work allows, for the first time, to separate temperature and dehydration contributions of the crystal volumetric changes.

For MnHCC hydrated and dehydrated states the number of moles of water inside the structure  $n_w$  remains constant or it is zero. In both cases, the crystal volume during an isobaric process would be only a function of temperature ( $dn_w = 0$ ). Therefore,  $\left( \frac{\partial V}{\partial n_w} \right)_{p,T} = 0$  in equation 3.4 and the thermal expansion coefficient  $\alpha$  is reduced to:

$$\alpha \equiv \frac{1}{V} \left( \frac{\partial V}{\partial T} \right)_{p,n} = \frac{1}{V} \left( \frac{dV}{dT} \right) = \frac{d \ln(V)}{dT} \quad (3.5)$$

---

<sup>1</sup>The crystal is losing water. The outer atmosphere must have a negligible hydration degree in order to absorb the evolving water and continue to have a nearly zero  $\mu_w$ .

### 3.1.3 Linear thermal expansion coefficient calculation for MnHCC single crystal

In this section we are going to determine  $\alpha$  for MnHCC hydrated and dehydrated states in addition to the temperature interval where MnHCC is partially dehydrated. To do this, the crystal volume ( $V$ ) and the number of moles of water remaining inside the structure ( $n_w$ ) in equation 3.4 must be transformed into unit cell dimensions to fit experimental crystallographic information. The resulting transformation is as follows,

$$V = N_c V_c = \frac{m_0}{mw Z} V_c \quad (3.6)$$

$$n_w = n_0 - \frac{mw Z}{m_0} n_{wec} \quad (3.7)$$

where:  $N_c$  is the number of unit cells in the sample,  $V_c$  is the unit cell volume,  $m_0$  is the sample mass,  $mw$  is the molecular weight,  $Z$  is the number of formula units per unit cell,  $n_0$  is the initial number of moles of water in the sample, and  $n_{wec}$  is the number of water molecules lost per unit cell at each temperature. Quick inspection of equation 3.4 after substituting relations 3.6 and 3.7 shows that  $\alpha$  is invariant to those transformations. This behaviour was expected because  $\alpha$  does not depend on the crystal size.

Finally, equation 3.4 can be rewritten in a suitable form to use X-ray and thermogravimetric experimental data as follows,

$$\alpha(T, n_{wec}) = \left[ \frac{\partial \ln(V_c)}{\partial T} \right]_p - \left[ \frac{\partial \ln(V_c)}{\partial n_{wec}} \right]_{p,T} \left( \frac{\partial n_{wec}}{\partial T} \right)_p \quad (3.8)$$

General results concerning single crystals X-ray diffraction data at variable temperatures in MnHCC single crystals are in Appendix A, table A.1 and the experimental strategy was already described in Chapter 2, Figure 2.4. Experimental points from table A.1 relevant to the estimation of the thermal expansion coefficient at each state, were selected and they are summarized in table 3.1.

**TEC for hydrated and dehydrated states: Finding  $\left[ \frac{\partial \ln(V_c)}{\partial T} \right]_p$  from the experiment.**

Data plots from table 3.1 in the form  $\ln(V_c)$  vs  $T$  are presented in figure 3.1. The first relevant question is: What is the correct functional form to fit the

CHAPTER 3. STRUCTURAL ANALYSIS OF MANGANESE  
HEXACYANOCOBALTATE

---

Table 3.1: Experimental Temperature ( $T$ ), cell parameter ( $a$ ) and calculated unit cell volume ( $V_c$ ) in MnHCC single crystals.

State	$T$ (K)	$a$ (Å)	$V_c$ (Å <sup>3</sup> )
Hydrated	100	10.3675(4)	1114.4(1)
	125	10.373(3)	1116(1)
	150	10.380(3)	1118(1)
	175	10.388(4)	1121(1)
	200	10.401(4)	1125(1)
	225	10.409(4)	1128(1)
	250	10.429(4)	1134(1)
	275	10.437(4)	1137(1)
Partially dehydrated	300	10.4135(9)	1129.2(3)
	325	10.405(4)	1126(1)
	350	10.383(4)	1119(1)
	375	10.285(14)	1088(4)
	400	10.250(9)	1077(3)
	425	10.229(15)	1070(5)
	450	10.27(2)	1083(6)
	475	10.25(1)	1077(3)
	500	10.223(4)	1068(1)
Dehydrated	500	10.223(4)	1068(1)
	300	10.248(5)	1076(2)
	100	10.274(3)	1084.5(9)

CHAPTER 3. STRUCTURAL ANALYSIS OF MANGANESE  
HEXACYANOCOBALTATE

Table 3.2: Slopes  $\left[\frac{d\ln(V_c)}{dT}\right]$  and intercept for linear fitting of experimental points in figure 3.1.

State	$\frac{d\ln(V_c)}{dT}$ (MK <sup>-1</sup> )	$\delta\frac{d\ln(V_c)}{dT}$ (MK <sup>-1</sup> )	$\ln(V_0)$	$\delta\ln(V_0)$
Hydrated	119.0140	7.99	7.002 54	1.5670
Partially	-291.2350	12.0200	7.119 85	4.9000
Dehydrated	-37.3226	0.3957	6.992 54	0.1352

experimental points at each state? The simplest scenario is for  $\left[\frac{\partial\ln(V_c)}{\partial T}\right]_p$  to be a constant which implies a linear behaviour for  $\ln(V_c) = f(T)$ . Considering the MnHCC structure, even when the structure is highly symmetric, the existence of disordered vacancies in its framework gives rise to anharmonic vibrations which suggest a deviation from the expected linear behaviour. To address this, three different functions (linear, polynomial and exponential) were fitted to data plots in figure 3.1. For dehydrated state, there are only three experimental points, therefore only a linear fitting is possible. In hydrated and partially dehydrated states, all three functions were tested. In order to choose the best fit, experimental values for  $\ln(V_c)$  were compared with the extrapolated values for linear fitting  $\ln(V_l)$ , polynomial fitting  $\ln(V_p)$  and exponential  $\ln(V_e)$ . Their differences are within the  $\delta\ln(V_c)$  error (see table A.2). Hence, the variation of  $\ln(V_c)$  with the temperature is indeed linear for the given experimental resolution. The linear fitting results are in table 3.2.

According to equation 3.5, for hydrated and dehydrated states, isobaric thermal expansion coefficient are:

$$\alpha_h = (119 \pm 8) \text{ MK}^{-1} \quad (3.9)$$

$$\alpha_d = (-37.3 \pm 0.4) \text{ MK}^{-1} \quad (3.10)$$

### TEC for partially dehydrated states

In order to determine  $\alpha$  from equation 3.8, the evolved millimole of water ( $n_{we}$ ) for each temperature and the cell volume were calculated using a Fortran 90 code. This code generates ( $V_c$ ,  $n_{we}$ ) pairs, interpolating temperature values from two input files:  $T$  vs  $V_c$  and  $T$  vs sample weight (thermogravimetric data). Output information appears in table 3.3. Values of  $n_{we}$  (in

CHAPTER 3. STRUCTURAL ANALYSIS OF MANGANESE  
HEXACYANOCOBALTATE

---

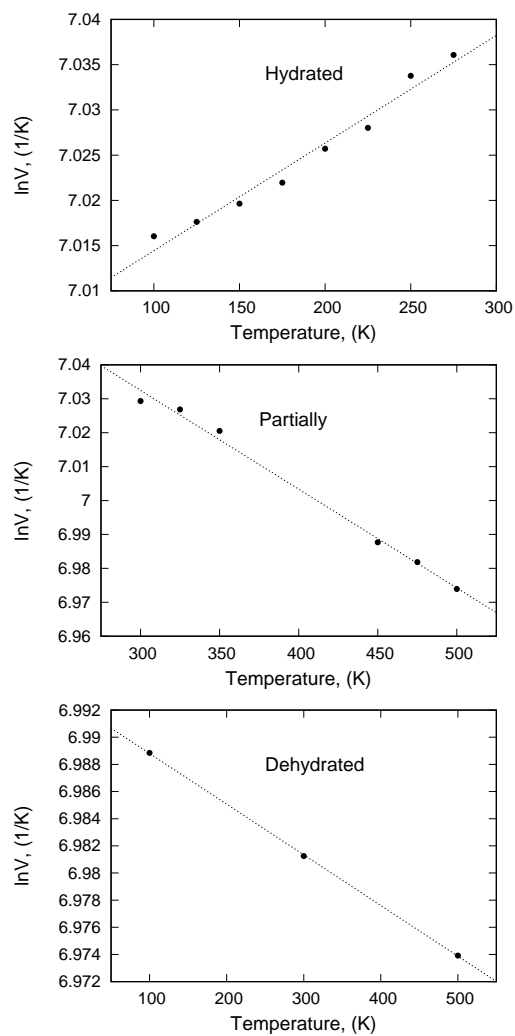


Figure 3.1:  $\ln V$  vs.  $T$  of hydrated, dehydrated and partially hydrated states in MnHCC single crystals.

CHAPTER 3. STRUCTURAL ANALYSIS OF MANGANESE  
HEXACYANOCOBALTATE

Table 3.3: Interpolation results.

Temperature (K)	$V_c$ ( $\text{\AA}^3$ )	$n_{we}$ ( $\mu\text{mol}$ )	$n_{wec}$ molec/cell
300	1129.25012	3.462	0.8186
325	1126.48718	7.684	1.8169
350	1119.35681	22.851	5.4034
450	1083.20667	66.396	15.6999
475	1076.89063	67.376	15.9316
500	1068.40295	68.075	16.0969

mmol) were transformed to  $n_{wec}$  (in molec/cell) using:

$$n_{wec} = \frac{mw Z}{m_0} n_{we}$$

Values in Table 3.3 were fitted to find  $\left[\frac{\partial \ln(V_c)}{\partial n_{wec}}\right]_{p,T}$  and  $\left(\frac{\partial n_{wec}}{\partial T}\right)_p$  derivatives (Figure 3.2). In Figure 3.2 (a) experimental data  $\ln(V_c)$  vs  $T$  shows a linear behaviour as was already discussed in section 3.1.3, table 3.2. In Figure 3.2 (b) a polynomial function was fitted to the first 4 points of  $\ln(V_c)$  vs  $n_{wec}$  to avoid further error due to the plot asymptotic tendency. The asymptotic behaviour is associated to the evolution of less than 3% residual water molecules, coordinated to Mn atoms, with high enthalpy of adsorption. MnHCC crystallize in the  $Fm\bar{3}m$  space group and has  $Z = 1.33$  formula units per unit cell. Considering TGA information, there are  $12.5^2$  water molecules per formula unit and hence there are 16.6 water molecules per each unit cell (see  $n_{wec}$  values for 475 K and 500 K in table 3.3). The same reasoning was applied to  $n_{wec}$  vs  $T$  linear fitting in plot (c). Fitted functions and their derivatives

---

<sup>2</sup>Even when the degree of accuracy given by the experiment is superior to the one reported (12.51 water molecules), the given data includes the possible error derived from choosing the correct limits for the dehydration event.

excluding their units were:

$$\ln(V_c) = (-2.912 \times 10^{-4}) T + 7.120 \quad (3.11)$$

$$\frac{d \ln(V_c)}{dT} = -2.912 \times 10^{-4} \quad (3.12)$$

$$\ln(V_c) = (-8.752 \times 10^{-5}) n_{\text{wec}}^2 (-1.325 \times 10^{-3}) n_{\text{wec}} + 7.030 \quad (3.13)$$

$$\left[ \frac{\partial \ln(V_c)}{\partial n_{\text{wec}}} \right]_{p,T} = (-1.750 \times 10^{-6}) n_{\text{wec}} - 1.325 \times 10^{-3} \quad (3.14)$$

$$n_{\text{wec}} = (1.030 \times 10^{-1}) T - 30.745 \quad (3.15)$$

$$\left( \frac{\partial n_{\text{wec}}}{\partial T} \right)_p = 1.030 \times 10^{-1} \quad (3.16)$$

Substituting equations 3.14 and 3.16 in equation 3.8:

$$\alpha_{\text{sd}} = (1.86) T - 708.84 \quad (3.17)$$

## Discussion

To explain thermal behaviour on MnHCC single crystals, it is useful to describe the system as a lattice of anharmonic oscillators. If the bond vibrations were purely harmonic the mean position of the atoms would not change even though the atoms would vibrate with larger and larger amplitudes as the temperature increases (Bragg peaks gives information about the average atomic positions).

In this structure the anharmonicity is given by the presence of different chemical elements. Their varied electronegativities result in different bond strengths and as a consequence, in an heterogeneous response to temperature variations. Additionally, there is anharmonicity related to the presence of two types of water inside the structure: coordinated and non-coordinated. The first type is substituting the missing  $[\text{Co}(\text{CN})_6]^{-3}$  ions and the second type is linked to water molecules coordinated by hydrogen bridges and also filling the volume of interstitial spaces. After dehydration, anharmonicity is caused by the presence of vacancies. In the partially dehydrated state, both features (the presence of different types of water molecules and the presence of vacancies) contribute to the anharmonicity. As the temperature increases, the population of higher energy levels of anharmonic lattice vibrations also increases which result in the increase of the average bond distances.

CHAPTER 3. STRUCTURAL ANALYSIS OF MANGANESE  
HEXACYANOCOBALTATE

---

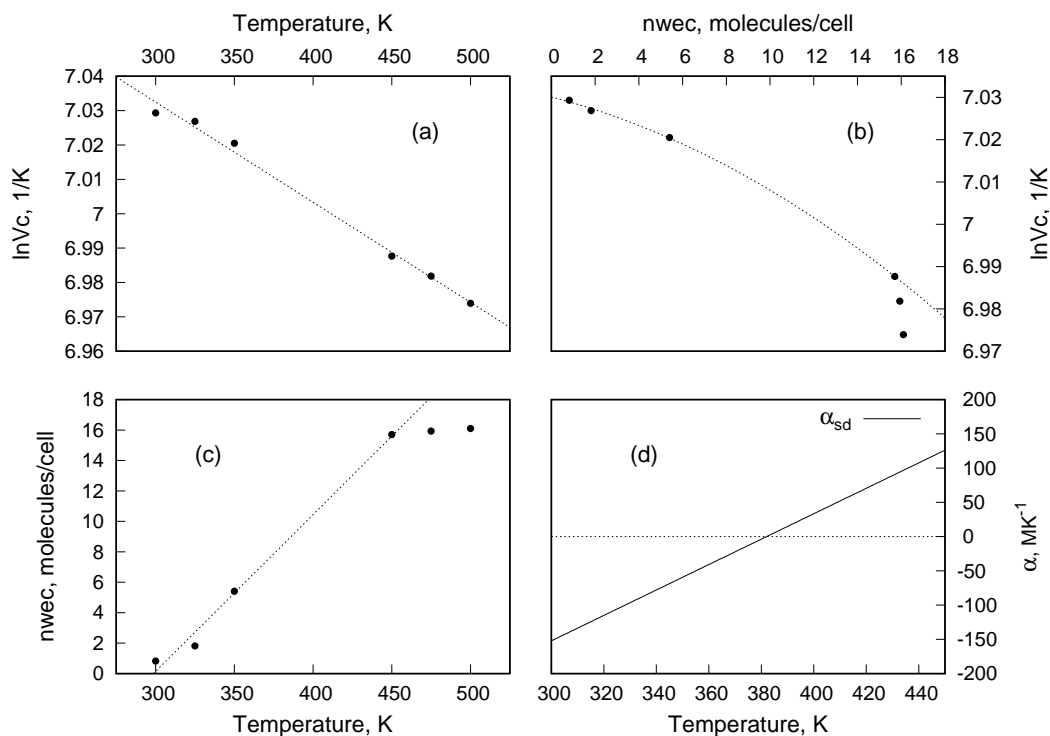


Figure 3.2: MnHCC semidehydrated state. Finding derivatives in equation 3.8: (a) Linear fitting:  $\frac{d\ln(V_c)}{dT}$  is a negative constant. (b) Polynomial fitting of  $V_c$  vs.  $n_{wec}$ , the derivative  $\left[\frac{\partial \ln(V_c)}{\partial n_{wec}}\right]_{p,T}$  is a linear function. (c) Linear fitting of  $n_{wec}$  vs.  $T$ , the derivative  $\left(\frac{\partial n_{wec}}{\partial T}\right)_p$  is a positive constant. (d) Plot for  $\alpha$  in equation 3.17,  $\alpha$  becomes zero at 382 K.

On the other hand, MnHCC structure incorporates stiff octahedral units ( $\text{MnN}_x\text{O}_{6-x}$  and  $\text{CoC}_6$ ) with strong metal carbon and metal-nitrogen bonds linked linearly by the relatively loose cyanide bridges, which confers considerable flexibility to the structure [146]. In these flexible systems, NTE has been shown to derive from the presence of low-energy, highly anharmonic transverse thermal vibrations, which tend to contract the lattice on heating. Such vibrations have been termed rigid unit modes and involve cooperative rotational motion of the rigid octahedral building blocks in the structure [147–149].

Both thermal features compete in the experimental temperature range, contributing to the global thermal behaviour of the structure. Considering the crystal  $Fm\bar{3}m$  symmetry and the high level of structural disorder, all three crystallographic directions change equally in each state.

**Hydrated state**(100 K to 275 K). The presence of non-coordinated water molecules filling the space inside the structure, prevents the contraction of the unit cell due to octahedral transverse thermal vibrations. Global volumetric changes are dominated by the increase of the average bond distances with temperature. Hence,  $\alpha_h$  is positive (see equation 3.9).

**Semidehydrated state**(300 K to 450 K). A linear behaviour is observed for  $\alpha_{sd}$  (Figure 3.2, plot (d)). At 300 K, approximately one molecule per cell is missing (table 3.3). Considering the differences in the bonding strengths between all three different types of water, those that occupy interstitial space evolve first. As a result, the number of volumetric defects increases, reducing the cell volume to a greater extent than its expansion due to the anharmonic vibrations. Besides, this available volume favours the octahedral transverse thermal vibrations and the global thermal effect is the contraction of the unit cell with temperature. As a consequence  $\alpha_{sd}$  is negative near 300 K.

From 300 K to 382 K dehydration is still dominated by the loss of non-coordinated water molecules (Table 3.3), but the volume reduction with the temperature is smaller because the hydrogen bonded water molecules generate smaller empty spaces when they leave the structure. This happens because they are more localized than interstitial water due to the stronger nature of hydrogen bonds interaction. As a consequence their thermal ellipsoid sphere is smaller. The contribution of octahedral transverse thermal vibrations is partially reduced by the contraction of the unit cell. At the same time, the bond distances continue to increase with temperature. The result of all contributions is a positive linear monotony for  $\alpha_{sd}$ .

At 382 K, the number of water molecules that have left the structure can

be determined using equation (3.15) ( $n_{wec} = 8.6$ ). As was mentioned before, considering thermogravimetric evidence, there is a hydration degree of 12.5 water molecules per MnHCC molecule. The number of formula units per unit cell is  $Z = 1.33$ , hence from initial 16.6 water molecules per cell only 8 remain inside the structure at 382 K and they are mostly coordinated waters because they are the most strongly bonded. At the present conditions, the usual effect of positive thermal expansion forces appear to finely balance the volume-reducing octahedral rotational modes, thereby leading to an overall zero thermal expansion ( $\alpha_{sd} = 0$ ). This structural behaviour has been reported for a similar structure [146].

From 382 K onward,  $\alpha_{sd}$  becomes positive. With temperature evolution, coordinated water molecules begin to leave the structure. Despite that they are the most strongly bonded, the irregular topology of the pores gives rise to a wide energy interval for coordinated waters which guaranties a continuous loss, in agreement with TGA experimental result for this sample (see 5.3). To compensate the structural disequilibrium, the C–N bonds are strengthened, reducing the contribution of the octahedral transverse thermal vibrations to the volume reduction. Under this conditions, the increase of the bond distances overcomes the cell reducing effect and the global thermal behaviour is the increase of the cell volume with the temperature, as observed for calculated  $\alpha_{sd}$  values between 382 K to 450 K.

Near 450 K, the loss of coordinated water molecules becomes asymptotic, indicating that the dehydration degree limit is being reached (Table 3.3). When the amount of coordinated water molecules is negligible and the temperature is between the 450 K to 500 K interval, the shape of Bragg diffraction points gets broader. This feature in addition to a change in the shape of the diffuse scattering pattern (Figure 3.3 (c) and (d)), suggests a sudden change in the structural disorder that can be attributed to a transition from collective vibration to an independent thermal vibration. This is the same as in a regular lattice of atoms in a uniform solid material at Debye temperature [150]. This transition can also explain the discontinuity near 500 K.

**Dehydrated state (500 K to 100 K).** Here, the available free volume in the structure due to vacancies provides an additional space for atomic vibrations to occur, despite the previous pore reduction. Thermal behaviour is dominated by the cooperative rotational motion of the rigid octahedral building blocks in the structure. When the temperature increases the average bond distance between the atoms also increases, but the final result is a decrease of volume with temperature because of the unit cell contraction due

to a displacement of the atoms towards the available empty spaces created by these vacancies. Hence  $\alpha_d$  is negative (equation 3.10). This volume reduction with temperature is known as negative thermal expansion (NTE) and is frequent in materials with CN bridges [151, 152].

**Comparing results.** To the best of our knowledge, this is the first time that MnHCC single crystals had being studied in three different states; and the first time that the contribution to the unit cell volume due to the loss of solvents and the temperature have been separated for semidehydrated states (equation 3.4). A linear thermal expansion coefficient for MnHCC from 125 K to 300 K was previously reported by Heinz Nakotte *et al.* [80]. The experiment was conducted on powder samples and  $\alpha_l$  was calculated as the slope of the linear fit to the curves of the lattice parameter  $l$  vs.  $T$  (section 1.2):

$$\alpha_l = \frac{1}{l_0} \left( \frac{\Delta l}{\Delta T} \right) \quad (3.18)$$

Where  $\Delta l$  is the average change in the lattice parameter over a temperature range  $\Delta T$  and  $l_0$  is the lattice parameter at a reference temperature (in their case, the room temperature). They reported two different values for  $\alpha_l$  because the dependence of unit cell parameter with temperature was clearly not linear:

$$\alpha_{l1} = (-29.2 \pm 5.8) \text{ MK}^{-1}$$

$$\alpha_{l2} = (-48.0 \pm 2.5) \text{ MK}^{-1}$$

In order to compare these results with ours, the relation between linear and volumetric thermal expansion coefficient must be evaluated (Chapter 1 section 1.2). Substituting their results in equation (1.7) and comparing with equations (3.9) and (3.10) can be concluded that Heinz results are not in agreement with this work: their  $\alpha_{l1}$  ( $\alpha_{l2}$ ) is negative while in this work  $\alpha_l$  is positive for the corresponding temperature interval. The deviation error between  $\alpha_l$  and  $\alpha_{l1}$  ( $\alpha_{l2}$ ) is 173 % (221 %).

There are two important mistakes in their assumptions. The first one is that the determination method is incorrect by definition because the thermal linear expansion coefficient  $\alpha_l$  is the slope in  $\ln(l)$  vs.  $T$  curve, not  $l$  vs.  $T$  (see Chapter 1, equation 1.6 in section 1.2). The use of the  $l_0$  reference is not realistic because  $l$  is changing for each point. The second one is to assume

that MnHCC structure is in a single state from 125 K to 300 K. Our results indicate that from 125 K to 275 K MnHCC is in hydrated state while from 275 K to 300 K is in semidehydrated state <sup>3</sup>. This wrong assumption results, in their case, in two results for  $\alpha_l$  instead of one: experimental data was inconsistent with a linear behaviour expected for hydrated state. Additionally, it must be considered that their experiments were performed with powder samples whilst in this work single crystals were used. Differences in crystal-lite sizes can explain why they began to observe a negative tendency from 175 K: A highly energetic X-ray beam can heat the powder sample making it to dehydrate faster.

In order to compare both thermodynamic and crystallographic methods (section 1.2),  $\alpha$  values for hydrated and dehydrated states were calculated from  $\alpha_l$  values determined from Pascal software [63]. Results are in Appendix A. Deviation errors are lower than 0.02 %.

## 3.2 Local structure observations on MnHCC single crystals: Diffuse scattering

Previous structural models of MnHCC, based on a classical crystallography analysis, suggest that vacancies are randomly distributed [22, 77, 79, 80]. However, this classical approach to explain the crystallographic data only allows the determination of the material's average structure. In materials with structural disorder, differences between local and average structure can introduce a significant error in any attempt to simulate their chemical or physical properties. Local structure can be described analysing the diffuse scattering behaviour.

In crystals, the diffuse scattering is a measure of the correlated structural disorder [17, 19]. For an ideal crystal the diffraction pattern is a set of discrete sharp Bragg reflections; while for completely disordered systems as liquids or glasses, the scattering consists of smoothly continuous broad rings with no distinguishable Bragg peaks. Crystal systems with a correlated disorder have an intermediate behaviour (see Figure 1.1, (b) and (e)), as they produce diffraction patterns with discrete Bragg reflections as well as continuous diffuse scattering. The shape of the diffuse scattering pattern determines the

---

<sup>3</sup>The correct determination method for semidehydrated state was explained in section 3.1.2

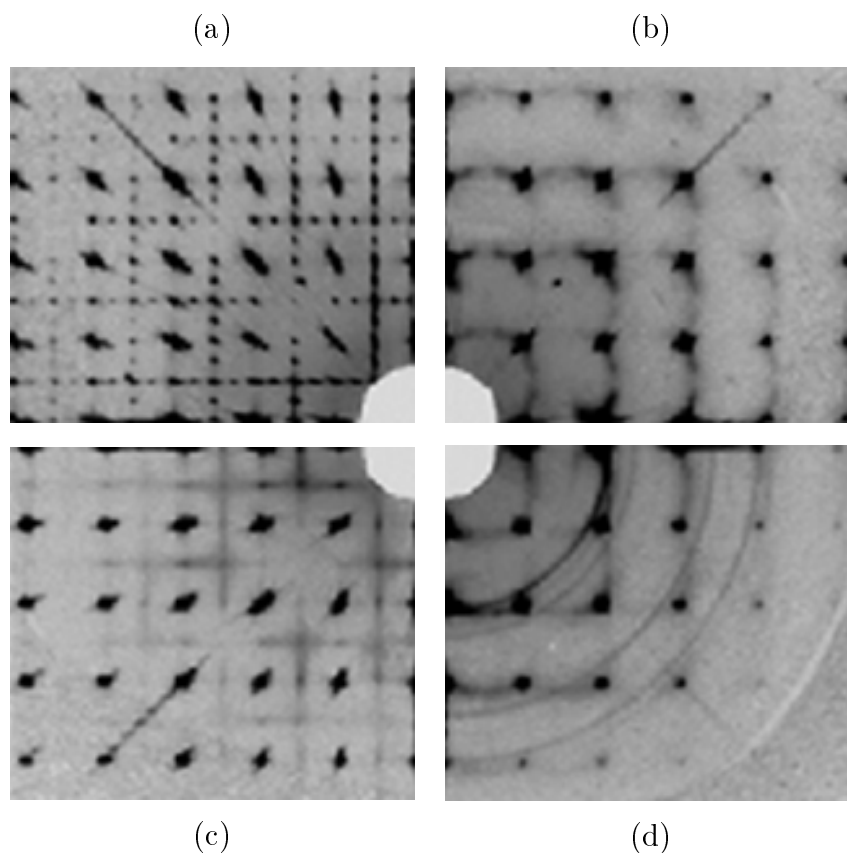


Figure 3.3: X-ray diffraction patterns of MnHCC single crystals, in  $[0kl]$  direction, measured at 100 K. Bragg reflections indicates the same average structure. Diffuse scattering shape is different in each picture which indicates a different disorder correlation. Picture (a), hydrated state of a single crystal synthesized in gel: The Bragg peaks are surrounded by small dots organized in perpendicular directions. Picture (b), corresponds to the same crystal and the same crystallographic direction, after dehydration: The shape of the diffuse scattering changes drastically, adopting a curly shape and now it crosses the Bragg peaks. Picture (c), hydrated state for a single crystal synthesized in water media: We can compare this picture with (a) and notice differences in the shape of the diffuse scattering. There are lines in this case, surrounding the Bragg peaks, which indicate that (c) is a more disordered structure than (a). Picture (d) represents the same crystal after dehydration and it can be noticed that for dehydrated state the diffuse scattering shape is very similar to (b).

correlation law between the disordered sites inside the crystal structure. This correlation suggests that the probability to have a vacancy is conditioned to the existence of previous vacancies next to it. In other words, they are not random.

MnHCC single crystals were synthesized in water and in gel media (section 2.1). Single crystals X-ray diffraction experiments were performed at 100 K on hydrated and dehydrated crystals to obtain structural information from each diffuse scattering pattern. The diffuse shape is different for each sample, as it can be observed in Figure 3.3.

These experiments provide information about the structural changes induced by water evolution and also by the used synthesis media. To address the first subject, we are going to analyse hydrated and dehydrated MnHCC crystals synthesized in water, using the saline bridge method. A comparison between Figure 3.3, pictures (c) and (d), indicates that the Bragg reflections are in the same position in both cases, which suggests the average structure is the same in hydrated and dehydrated states, but the diffuse scattering shape is different. In (c) the diffuse pattern consists of straight lines passing between the Bragg reflections but in (d) the diffuse pattern adopts a curved shape and now passes through the Bragg reflections. The same tendency is observed comparing MnHCC hydrated and dehydrated single crystals synthesized in gel (3.3, pictures (a) and (b)). The second subject is the influence of the synthesis media on the structural disorder. Although the structures (a) and (c) have the same average structure (Bragg reflections), differences in the diffuse scattering shape are evident. In picture (a) the Bragg peaks are surrounded by small dots organized in perpendicular directions whilst in (c) it is not possible to distinguish dots because the diffuse pattern consists of continuous lines, traced in the same perpendicular directions. These differences suggest that the crystal synthesized in gel, (structure (a)), is more organized than the one synthesized in water, probably because the gel framework influences the crystallographic directions in which the crystal grows, acting as a chemical template. This assumption is corroborated by the fact that for similar experimental conditions more information is obtained from the crystal synthesized in gel, because it is possible to see a higher number of Bragg peaks in Figure 3.3 than for the crystals synthesized in water. Nevertheless, in pictures (b) and (d) the shape of the diffuse patterns are indistinguishable (both, Bragg peaks and the diffuse shape) and, according to previous experimental results, there is no crystallographic evidence of a change in the spatial group of crystallographic symmetry with dehydration.

These two features (indistinguishable diffuse patterns and the assignation of the same crystallographic space group) indicate that differences in the shape of the structural disorder due to the synthesis conditions are mainly related with the positions of disordered water molecules and the nature of their interaction, rather than the positions of ordered water molecules, metal ions or cyanide bridges<sup>4</sup>. After dehydration the structure has a smaller cell parameter but the positions of Bragg peaks are the same.

To find a structural model capable of explaining the diffuse scattering experimental behaviour, Monte Carlo simulations were performed on MnHCC hydrated and dehydrated states (Figure 3.4). These results are preliminary and further calculation must be performed to improve the explanation of the experimental data. Nevertheless, these results can provide some conclusions.

The shape of the modelled diffuse scattering pattern in hydrated state (picture (I)) is similar to its experimental shape, as can be corroborated by comparison with Figure 3.3, pictures (a) and (c). Picture (I) was generated taking into account the occupancy factors reported for the average structure [77], (1 and 2/3 for Mn<sup>2+</sup> and Co<sup>3+</sup> cations respectively). The conclusion is that structural disorder in hydrated phase is dominated by the interaction of water molecules with the framework. Therefore, the morphology of the pores depends on the chosen synthesis media. In picture (III), a spatial arrangement of atoms able to reproduce the diffuse pattern in picture (I) is presented.

The diffuse scattering pattern for the dehydrated state (picture (II)), is also similar to experimental patterns (b) and (d) in Figure 3.3. In both cases (simulated and experimental) this pattern is formed by diffuse lines passing through the Bragg peaks. To generate the spatial arrangement of atoms that represent this diffuse shape (picture (IV)), only Mn and Co positions were taken into account since there was no clear understanding of how the CN groups were distributed in the crystal after dehydration. In this case, it was assumed that Mn and Co occupancy factors were the same. The result obtained using this assumption requires further justification: dehydration process creates a great distortion in the framework, mostly because of the loss of coordinated water. Although the framework does not collapse completely, as can be seen by the presence of Bragg intensities in pictures (b) and (d),

---

<sup>4</sup>The Bragg peaks positions are determined by the distance between parallel planes of atoms, while the Bragg peak intensities are determined by the arrangement of atoms in the entire crystal (structure factor).

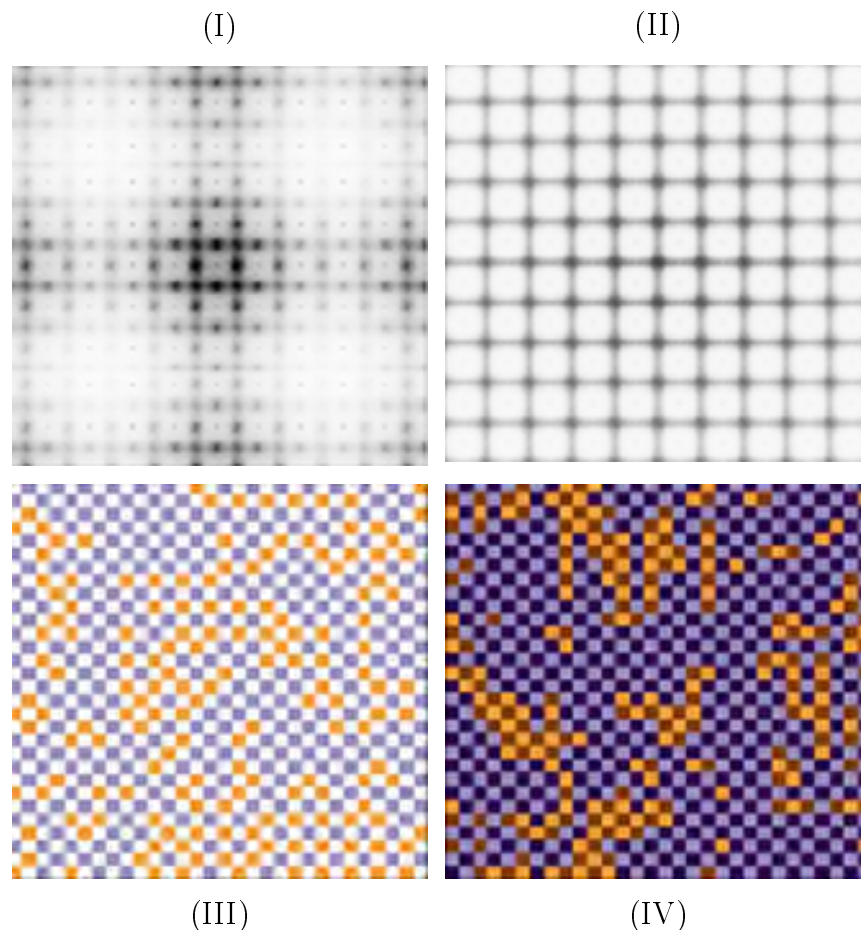


Figure 3.4: Monte Carlo simulations for diffuse scattering in MnHCC single crystals. Picture (I): Diffuse scattering pattern simulated for hydrated state. Here atoms have the same occupation factor that they have in the average structure. The diffuse pattern is oriented in perpendicular directions around the Bragg peaks. Atoms are located in space following the arrangement in picture (III) (white squares ( $\text{Mn}^{2+}$ ), blue ( $[\text{Co}(\text{CN})_6]^{3-}$ ), orange (vacancies)). Picture (II): Diffuse scattering pattern simulated for dehydrated state. Here atoms have the same occupation factor of one. The diffuse pattern is oriented in perpendicular directions crossing the Bragg peaks. Atoms are located in the space following the arrangement in picture (IV) (dark blue squares ( $\text{Mn}^{2+}$ ), light blue (Co), brown and orange (vacancies)).

CHAPTER 3. STRUCTURAL ANALYSIS OF MANGANESE  
HEXACYANOCOBALTATE

---

a partial collapse is observed via the presence of concentric rings of diffuse scattering. Considering that the framework keeps the average stoichiometric chemical composition in this temperature range, the use of the same occupancy factors for both metals suggests that they become indistinguishable in terms of their position inside the structure.

To verify the hypothesis of indistinguishable metal positions in the structure, experimental evidence of a phase transition from a face-centered cubic to a primitive crystallographic system would be required. The analysis of the Bragg peaks positions from the diffraction patterns in Figure 3.3 could be sufficient in this regard. This is part of the future work related with this thesis<sup>5</sup>.

The curved shape of the diffuse scattering data in pictures (b) and (d), could not be explained by a displacement disorder. Further analysis of other types of disorder is needed to explain it.

---

<sup>5</sup>The dehydrated structure of MnHCC has not yet been reported. A previous work of Reguera *et al.* reports the cell parameter from powder diffraction data [22] but the diffraction pattern had a poor quality and the structure was assumed to be  $Fm\bar{3}m$  in absence of any refuting experimental evidence.

## Chapter 4

# Langmuir-Freundlich Adsorption Model

### 4.1 About the need for this model

Prussian blue analogues are adsorbent materials with a complex size distribution of irregular pores and energetically heterogeneous surfaces, which results in isotherms with non-linear functional shapes. Therefore, a suitable adsorption model must have at least three parameters to explain experimental data, and must be able to describe the adsorption in disordered materials for different adsorbates using a simple isotherm equation. One of them is the *Vacancy Solution Model*. This model is based on a solid solution approach and hence, does not take into account the adsorbate's intrinsic characteristics. The simplest isotherm derived from this model, able to describe heterogeneous adsorbents, is the Langmuir-Freundlich equation. Some derivations of this isotherm have been previously reported [153, 154]. However, all of them use the osmotic hypothesis that fails to describe the system adequately.

In this Chapter the parallelism generally used between the adsorption and osmotic experiments is replaced by a more general series expansion; the connection between the relative activity coefficient parameter for vacancies and one parameter of the isotherm is well established, and the functional dependence between partial enthalpy of adsorption and isotherm parameters is found.

## 4.2 Langmuir-Freundlich isotherm

Let the adsorbed phase be a solution where the particles of adsorbate are the solute and their vacancies the solvent. Thus, the sum of the volume occupied by the particles of adsorbate ( $V_a$ ) with the free volume ( $V_v$ ) is equal to the total volume accessible to the adsorbate molecules:

$$V = V_a + V_v$$

If additionally, the volume of the adsorbate ( $b$ ) is the same as that of the vacancies, then the maximum number of adsorption sites in the adsorbent ( $N_m$ ) is:

$$N_m = \frac{V}{b} = \frac{V_a}{b} + \frac{V_v}{b} = N_a + N_v$$

where:  $V$  is the total pore volume in the adsorbent,  $N_a$  is the number of adsorption sites occupied by the adsorbate and  $N_v$  are the number of unoccupied sites. Dividing the whole equation by  $N_m$ :

$$\frac{N_a}{N_m} + \frac{N_v}{N_m} = \frac{n_a}{n_m} + \frac{n_v}{n_m} = X_a + X_v = 1$$

here the lowercase letters refer to the molar amounts. The gas phase is considered as a solution of the adsorbate at the vacancies in such a diluted state that it can be considered as pure vacancies. Solving for  $X_v$ :

$$X_v = 1 - \frac{N_a}{N_m} = 1 - \frac{n_a}{n_m} = 1 - \theta \quad (4.1)$$

where  $\theta$  is the volume filling of the adsorbate.

The field of the adsorbent causes the pressure in the adsorbed phase ( $p_v$ ) to be different from the gas phase ( $p$ ), so the chemical equilibrium condition for the vacancies has the form:

$$\mu_v(p, T, 1) = \mu_v(p_v, T, X_v) \quad (4.2)$$

Expanding  $\mu_v(p_v, T, X_v)$  in a Taylor series around  $p$ :

$$\mu_v(p_v, T, X_v) = \mu_v(p, T, X_v) + \left. \frac{\partial \mu_v(p_v, T, X_v)}{\partial p_v} \right|_{p_v=p} (p_v - p) + \mathcal{O}[p - p_v]^2$$

Considering that the derivative of the chemical potential with respect to the pressure is the molar volume, making  $\pi = p_v - p$ , substituting into 4.2 and neglecting powers higher to one in the series expansion because  $(p_v - p) \approx 0$ :

$$\mu_v(p, T, 1) \approx \mu_v(p, T, X_v) + v_v\pi \quad (4.3)$$

Moreover, the chemical potential of the vacancies in the gas phase will be:

$$\mu_v(p, T, 1) \approx \mu_g^\circ(p, T) + RT \ln(1) \approx \mu_g^\circ(p, T) \quad (4.4)$$

The adsorbed phase can be considered broadly as a non-ideal solution so that the chemical potential of the vacancies has a term of excess with respect to the ideal case:

$$\mu_v(p, T, X_v) = \mu_v^\circ(p, T) + RT \ln(X_v) + \mu_v^E = \mu_v^\circ(p, T) + RT \ln(fX_v) \quad (4.5)$$

where we have introduced the relative activity coefficient  $f$  as  $\mu_v^E = RT \ln(f)$ . Besides, substituting  $\mu_v(p, T, 1)$  from (4.4) in (4.3), solving for  $\mu_v(p, T, X_v)$ , substituting it in equation (4.5), and simplifying  $\mu_v^\circ(p, T)$  terms we obtain:

$$-v_v\pi = RT \ln(fX_v) \quad (4.6)$$

Replacing  $X_v$  from equation (4.1) in (4.6):

$$-v_v\pi = RT \ln[f(1 - \theta)] \quad (4.7)$$

Given that the molar volume of vacancies and temperature are constant and differentiating the entire equation:

$$-v_v d\pi = RT d \ln[f(1 - \theta)] \quad (4.8)$$

The Gibbs-Duhem equation for the adsorbed phase is:

$$SdT - Vdp + n_v d\mu_v + n_a d\mu_a = 0$$

Isothermal addition of an infinitesimal amount of adsorbate should not cause changes in the chemical potential of the vacancies as the chemical potential of them in the gas phase does not change. Therefore the Gibbs-Duhem equation becomes (note that  $-dp = d\pi$ )<sup>1</sup>.

---

<sup>1</sup>Adsorbent vacancies are in equilibrium with the vacancies reservoir and the mechanical equilibrium impose the condition  $p_v = \text{Const}$ .

$$-Vd\pi = n_a d\mu_a \quad (4.9)$$

Given that  $V = v_v n_m$ , eliminating  $d\pi$  from equations (4.8) and (4.9), and transforming:

$$\theta d\mu_a = RT d \ln [f(1 - \theta)] \quad (4.10)$$

If in the above equation we take into account that the adsorbed phase is in equilibrium with the gas and that it is in such conditions that it can be considered as an ideal gas then:

$$d\mu_a = RT d \ln (p_{eq}) \quad (4.11)$$

Substituting (4.11) in (4.10) and simplifying  $RT$ :

$$d \ln (p_{eq}) = d \ln [f(1 - \theta)]$$

Let  $f = (1 - \theta)^{g-1}$  in the above equation, grouping  $\theta$  on the left side of equation and transforming:

$$d \ln (p_{eq}^{1/g}) = -d \ln \left( \frac{\theta}{1 - \theta} \right)$$

Integrating the above equation, transforming and eliminating the logarithms:

$$p_{eq} = C^g \left( \frac{\theta}{1 - \theta} \right)^g$$

where  $C$  is an integration constant equal to the pressure evaluated at  $\theta = 1/2$ :

$$p_{eq} = p_{1/2} \left( \frac{\theta}{1 - \theta} \right)^g \quad (4.12)$$

Solving this equation for adsorbed moles of adsorbate ( $n_a = n_m \theta$ ) we obtain the Langmuir-Freundlich isotherm:

$$n_a = \frac{n_m p_{1/2}^{-1/g} p_{eq}^{1/g}}{1 + p_{1/2}^{-1/g} p_{eq}^{1/g}} \quad (4.13)$$

Here the parameter  $n_m$  is the limit capacity,  $p_{1/2}$  is the pressure evaluated at  $\theta_{1/2}$  and is related with the isotherm's slope and hence with the adsorption energy distribution. The parameter  $g$  describes how much the material is deviated from an ideal solution.

### 4.3 Temperature dependence of parameter $g$

Replacing  $f = (1 - \theta)^{g-1}$  in equation (4.10) and transforming:

$$\begin{aligned}\theta d\mu_a &= RT d \ln [(1 - \theta)^g] \\ \theta d\mu_a &= -\frac{RTg}{1 - \theta} d\theta \\ d\mu_a &= -\frac{RTg}{\theta(1 - \theta)} d\theta \\ d\mu_a &= RTg d \ln \left( \frac{\theta}{1 - \theta} \right)\end{aligned}\tag{4.14}$$

Integrating (4.14) from  $\theta = 1/2$ <sup>2</sup> to  $\theta$ :

$$\mu_a - \mu_{1/2} = RTg \ln \left( \frac{\theta}{1 - \theta} \right)$$

Solving for  $g$ :

$$g = \frac{\Delta\mu}{RT \ln \left( \frac{\theta}{1 - \theta} \right)}$$

Given that  $\Delta\mu = \Delta h - T\Delta s$ :

$$g = \frac{\Delta h}{RT \ln \left( \frac{\theta}{1 - \theta} \right)} + \frac{\Delta s}{R \ln \left( \frac{\theta}{1 - \theta} \right)}\tag{4.15}$$

Since  $\lim_{T \rightarrow \infty} g = 1$  because at high temperatures the solution should become ideal, then:

$$\lim_{T \rightarrow \infty} \frac{\Delta h}{RT \ln \left( \frac{\theta}{1 - \theta} \right)} = 0$$

This limit is zero because  $\Delta h = \int c_p dT$  and the  $c_p$  changes very little with temperature. According to the above, the entropic term in equation (4.15) is one in the high temperature limit and:

$$\begin{aligned}g &= \frac{\Delta h}{RT \ln \left( \frac{\theta}{1 - \theta} \right)} \\ g &= 1 - \frac{b}{T}\end{aligned}\tag{4.16}$$

where

$$b = \frac{\Delta h}{R \ln \left( \frac{\theta}{1 - \theta} \right)}$$

---

<sup>2</sup> $\theta = 1/2$  is equivalent to  $\ln \left( \frac{\theta}{1 - \theta} \right) = 0$

## 4.4 Temperature dependence of parameter $p_{1/2}$

The Langmuir-Freundlich isotherm (4.13) becomes Langmuir isotherm [155] for ideal solution ( $g = 1$ ) with:

$$p_{1/2}^{-1} = K_L \quad (4.17)$$

The Langmuir model for mobile adsorption can describe the gas adsorption in heterogeneous porous materials with polar adsorption sites. The functional dependence of the Langmuir constant with temperature in this model is [155]:

$$K_L = \frac{c}{T} \exp\left(\frac{d}{T}\right) \quad (4.18)$$

where  $c$  depends on the ratio between the internal partition function of the adsorbate in gas and in adsorbed phases, and  $d$  depend on the adsorbate energies in gas and adsorbed phases. Substituting (4.18) in (4.17) and transforming:

$$p_{1/2} = \frac{T}{c} \exp\left(-\frac{d}{T}\right) \quad (4.19)$$

Whereas the internal partition function of adsorbate does not change during the adsorption process,  $c = v_M/R$ , where  $v_M$  is the molar adsorbate volume [155]. Under these conditions, the equation (4.19) becomes:

$$p_{1/2} = \frac{RT}{v_M} \exp\left(-\frac{d}{T}\right) \quad (4.20)$$

## 4.5 Molar enthalpy of adsorption

From Clausius-Clapeyron relation [156, p. 230]:

$$dp_{\text{eq}} = \frac{1}{T} \frac{\Delta h}{v_g - v_a} dT$$

where  $\Delta h$  is the molar enthalpy necessary to transform one mole of adsorbate in adsorbed phase to gas,  $v_g$  is the molar volume of the adsorbate in the gas phase, and  $v_a$  is the molar volume of the adsorbate in the adsorbed phase. Since:  $v_g \gg v_a$ , and the gas phase can be considered as an ideal gas ( $v_g = RT/p_{\text{eq}}$ ):

$$d \ln(p_{\text{eq}}) = \frac{\Delta h}{RT^2} dT$$

differentiating with respect to  $T$  at constant composition and solving for  $\Delta h$ :

$$\Delta h = RT^2 \left[ \frac{\partial \ln(p_{\text{eq}})}{\partial T} \right]_{\theta} \quad (4.21)$$

Substituting (4.12) in (4.21), and differentiating with respect to temperature, given that  $p_{1/2}$  and  $g$  are functions of the temperature (equations (4.16) and (4.20)):

$$\Delta h = RT^2 \ln \left( \frac{\theta}{1-\theta} \right) g'(T) + RT^2 \frac{p'_{1/2}(T)}{p_{1/2}(T)} \quad (4.22)$$

Substituting (4.20), the derivative of  $p_{1/2}$  from (4.20), the derivative of  $g$  from (4.16), and transforming:

$$\Delta h = Rb \ln \left( \frac{\theta}{1-\theta} \right) + R(d+T) \quad (4.23)$$

Clearing  $b$  from (4.16),  $d$  from (4.20), and replacing them in (4.23) an expression for estimating  $\Delta h$  as a function of the isotherm parameters  $p_{1/2}$  and  $g$  is obtained:

$$\Delta h = RT(1-g) \ln \left( \frac{\theta}{1-\theta} \right) + RT \left[ 1 - \ln \left( \frac{v_M}{RT} p_{1/2} \right) \right] \quad (4.24)$$

# Chapter 5

## Post-synthesis modification

In order to define a methodology for the post-synthesis modification of MnHCC and CoHCC, an experimental setup was designed and implemented as described in section 2.2. The samples were exposed to an ozone enriched dry air flux until saturation was verified experimentally (Figure 5.1).

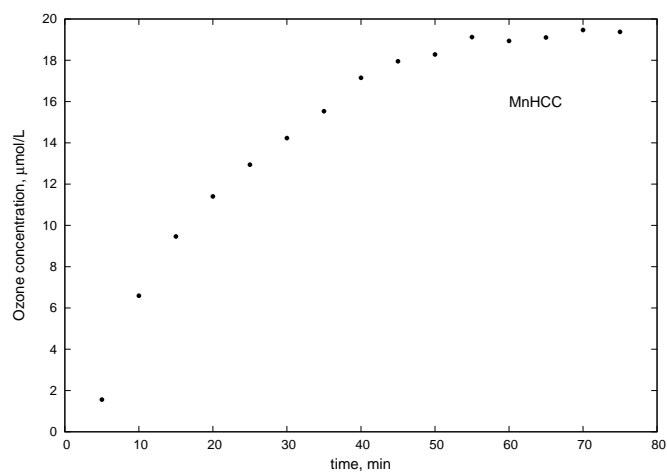


Figure 5.1: Ozone concentration *vs.* time for MnHCC powder sample. The sample was exposed to ozone until saturation was reached.

## 5.1 Infrared and Raman spectroscopy

The Infrared spectra for hexacyanocobaltates in the region from  $\tilde{\nu} = 4000 \text{ cm}^{-1}$  to  $1000 \text{ cm}^{-1}$  show three bands: a narrow band around  $\tilde{\nu} = 2160 \text{ cm}^{-1}$  assigned to  $\nu_{CN}$  stretching mode of the  $\text{C}\equiv\text{N}$  bond in  $[\text{Co}(\text{CN})_6]^{3-}$  octahedral structural unit, and two broader bands corresponding to the stretching  $\nu_{OH}$  and bending  $\delta_{H-O-H}$  modes for the water molecules in the structure. These bands are located around  $\tilde{\nu} = 3400 \text{ cm}^{-1}$  and  $1600 \text{ cm}^{-1}$  respectively, (Figure 5.2 a) and c)). In the ozonized materials  $\nu_{CN}$  bands shift to higher frequencies and the  $\delta_{H-O-H}$  band splits into three (Figure 5.2 b) and d)). The  $\nu_{CN}$  band shift is consistent with the oxidation of the metal coordinated to nitrogen [41]. The electron density of the linking metal decreases, thus favouring the  $\sigma$  donation from  $\text{C}\equiv\text{N}^-$  ligands and reducing the  $\pi$  back-bonding donation [157] from the metals d orbitals. Both effects strengthen the  $\text{C}\equiv\text{N}$  triple bond increasing the  $\nu_{CN}$  frequency. The appearance of new bands associated with  $\delta(\text{H}-\text{O}-\text{H})$  bending modes can be explained considering how the ozonization changes the interaction of water molecules with the framework. There are two types of water in the crystal structure: coordinated and non-coordinated. The first type is linked to the metallic centers through a coordination bond, substituting missing  $\text{CN}^-$  groups from  $[\text{Co}(\text{CN})_6]^{3-}$  molecular building blocks. After ozonization, the positive charge increases at the metal coordinated to nitrogen end of the cyano ligands favoring the displacement of the electronic density from the oxygen atom of the coordinated water molecules to the metal through a  $\sigma$  donation. This displacement weakens the  $\text{O}-\text{H}$  bond and it can explain the shift of  $\delta(\text{H}-\text{O}-\text{H})$  band to smaller frequencies. The second type of water (non-coordinated) fills the rest of the accessible volume interacting between them through Van der Waals forces and hydrogen bonds. These non-coordinated molecules are poorly affected by the metals' charge. Therefore, the effect of the ozonization in the frequency modes are less evident.

The FTIR spectra of dehydrated and ozonized samples have similar differences relative to the as-synthesized sample FTIR spectrum. In both cases the  $\nu_{CN}$  bands shift to higher frequencies. The coordinated water molecules share the electronic density with the positive cationic centres. After the water molecules are removed from the framework the local electronic density decreases. This is analogous to the oxidation of the metals. Experimental FTIR data supporting this similarities can be found in Appendix B, section B.1.

So far, it has not been considered whether  $O_3$  reacted with the metal coordinated to the nitrogen atom in the  $C\equiv N$  ligand, the metal coordinated to the carbon atom in the  $C\equiv N$  ligand, the  $C\equiv N$  ligand itself or with several chemical species at the same time. To get a deeper understanding, we choosed the CuHCC compound. The oxidation  $Cu^{2+}/Cu^{3+}$  has a potential of  $-2.3\text{ V}$  [86] while the standard reduction potential for  $O_3$  is  $2.07\text{ V}$  [86]. So the  $O_3$  standard reduction potential is insufficient to oxidise the  $Cu^{2+}$ . This result is consistent with the small shift observed for the  $\nu_{CN}$  band of the ozonized CuHCC relative to as-synthesized sample (see Appendix B, section B.1). This result suggests that the  $[Co(CN)_6]^{3-}$  building unit do not interact with  $O_3$ .

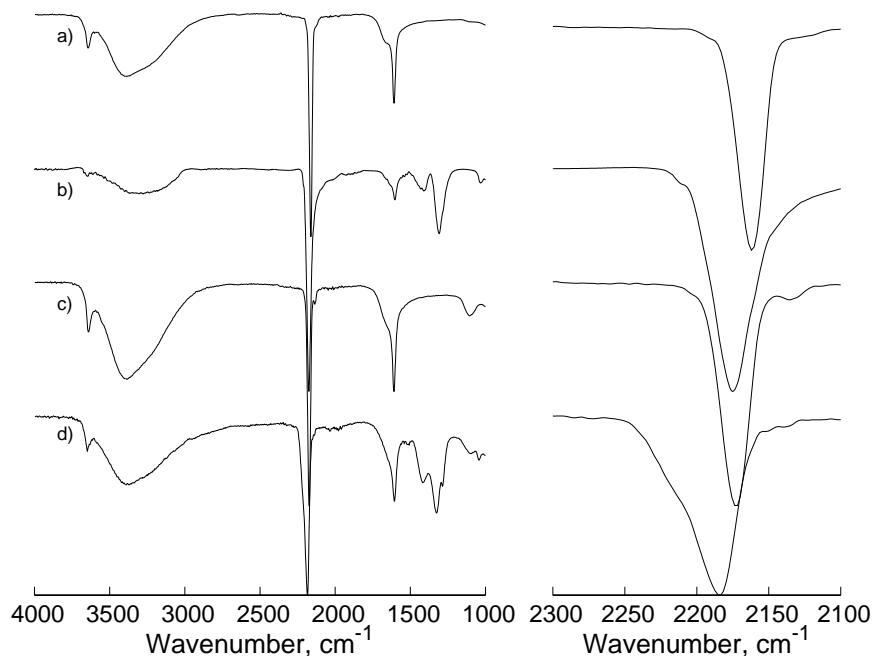


Figure 5.2: Full FTIR spectra (left column) and  $\nu_{CN}$  bands region (right column). FTIR spectra of: a) MnHCC as-synthesized, b) ozonized and hydrated MnHCC, c) CoHCC as-synthesized, d) ozonized and hydrated CoHCC.

The local symmetry of the metal coordinated to nitrogen end of cyano ligands in  $M_3[Co(CN)_6]_2 \cdot nH_2O$  ( $M = Mn$  and  $Co$ ) is not strictly octahedral. However, the observed Raman spectra do not strongly deviate from

the theoretical spectrum expected using  $Fm\bar{3}m$  selection rules. Assignments for MnHCC have been made considering reference [40] (Table 5.1). Both materials, MnHCC and CoHCC have the same four Raman active modes:

1.  $A_{1g}$  stretching mode of  $C\equiv N$ .
2.  $E_g$  stretching mode of  $C\equiv N$ .
3.  $F_{2g}$  stretching mode of  $Co-C\equiv N$ .
4.  $F_{2g}$  stretching mode of  $C-Co-C$ .

There are no active modes for  $M_3[Co(CN)_6]_2$  ( $M = Mn$  and  $Co$ ) framework. Signal-to-noise ratio of CoHCC and CoHCCOz Raman spectra are low due to the high contribution to the background from the fluorescence of the sample. The quality of the spectra prevented their analysis.

The  $\nu_1$  and  $\nu_3$  bands of MnHCC Raman spectrum (Table 5.1) are located at  $\tilde{\nu}=2192\text{ cm}^{-1}$  and  $\tilde{\nu}=2173\text{ cm}^{-1}$  respectively. These lines shift to higher frequencies,  $2197\text{ cm}^{-1}$  and  $2177\text{ cm}^{-1}$ , in the  $CoMnO_3$  spectrum. The Raman spectrum of MnHCC in the  $Co-C$  stretch and  $Co-C-N$  deformation region is expected to show three bands. Instead, a broad band at  $\tilde{\nu} = 480\text{ cm}^{-1}$  is present. This band can be resolved for  $\nu_2$  at  $\tilde{\nu}=484\text{ cm}^{-1}$  and  $\nu_4$  at  $\tilde{\nu}=469\text{ cm}^{-1}$ . Both frequencies contribute to the  $\nu_{10}$  at  $\tilde{\nu}=480\text{ cm}^{-1}$ . The ozonized sample has the  $\nu_2$  band at  $\tilde{\nu}=486\text{ cm}^{-1}$ , the  $\nu_4$  band at  $\tilde{\nu}=470\text{ cm}^{-1}$  and the  $\nu_{10}$  band is shifted to  $\tilde{\nu}=484\text{ cm}^{-1}$ . In the low energy region, a broad peak is observed for MnHCC at  $\tilde{\nu} = 202\text{ cm}^{-1}$ . This broad band has been assigned to an  $F_{2g}$  symmetry mode and  $C-Co-C$  deformation  $\nu_{11}$ . After ozonization the band becomes broader. Additionally, MnHCCOz spectra has three new small bands at  $\tilde{\nu}=2438\text{ cm}^{-1}$ ,  $\tilde{\nu}=1054\text{ cm}^{-1}$  and  $\tilde{\nu}=581\text{ cm}^{-1}$ .

Raman spectra provide structural and bonding information [157]. On the structural side, the general agreement of MnHCC Raman active modes with  $Fm\bar{3}m$  selection rules is consistent with an octahedral environment for  $[Co(CN)_6]^{3-}$  building units. The widening of the  $C-Co-C$  band in MnHCCOz spectrum after ozonization suggests a symmetry reduction around the Co sites. It could be due to structural deformations around the exposed metallic centres caused by electric density changes after the reaction with ozone. To understand how changes in the nature of chemical bonds affect the Raman spectra, it is convenient to note that the oxidation of the metal coordinated to the nitrogen atom and dehydration have similar effects. Both

Table 5.1: Observed Raman modes for the  $[\text{Co}(\text{CN})_6]^{3-}$  building units in as-synthesized and ozonized samples.

Mode	MnHCC $\text{cm}^{-1}$	MnCoO3 $\text{cm}^{-1}$	Ref. MnHCC [40] $\text{cm}^{-1}$
$\nu_1(\text{A}_{1g}, \text{CN})$	2192	2197	2191
$\nu_2(\text{A}_{1g}, \text{CoC})$	484	486	485
$\nu_3(\text{E}_g, \text{CN})$	2173	2177	2172
$\nu_4(\text{E}_g, \text{CoC})$	469	470	470
$\nu_{10}(\text{F}_{2g}, \text{CoCN})$	480	484	480
$\nu_{11}(\text{F}_{2g}, \text{CCoC})$	202	202 <sup>a</sup>	202

<sup>a</sup> This band is broader than the corresponding band in MnHCC.

processes reduce the charge density of the metal coordinated to the nitrogen atom. Hence, the observed Raman modes in the MnHCCOz spectrum can be compared with previous reports of dehydrated MnHCC crystals [40]. The shift of  $\nu_1$ ,  $\nu_2$ ,  $\nu_3$  and  $\nu_4$  to higher frequencies in MnHCCOz suggests that the Mn–N bond has been strengthened after ozonization. This strengthening is consistent with the infrared experimental results provided at this section and with the total diffraction experimental results discussed in section 5.2.

## 5.2 X-ray diffraction

According to their powder X-ray diffraction patterns, MnHCC and CoHCC crystallize in  $Fm\bar{3}m$  space group, in agreement with previous reports [73, 77, 79]. The crystalline system remains cubic and there is no indication of a change in the crystallographic space group due to dehydration or exposure to ozone. Cell parameters decrease after both processes for both materials (Table 5.2). The unit cell volume is reduced after dehydration by 3% for MnHCC and by 2% for CoHCC. After being exposed to ozone and rehydrated, the analysis of the diffraction patterns indicates the presence of two phases for MnHCC, one with a cell parameter  $a = 10.3511(6)$  Å, corresponding to a 2% volume contraction and another with a cell parameter of  $a = 10.2734(8)$  Å corresponding to a 4% cell contraction. These two phases suggest the existence of two different oxidation states for manganese. The contraction in the CoHCC cell volume was 3% relative to the as-synthesized phase.

The Differential Correlation Function for MnHCC has two maxima at around 1.9 Å and 2.4 Å (Figure 5.3) in agreement with the reported distances for Co–C and Mn–N bonds [22]. A similar behaviour is observed for CoHCC. However, the peak corresponding to the Co–N distance ( $\sim 1.9$  Å) overlaps with the peak corresponding to the Co–C distance (Figure 5.3). The Co–C peak shifts to higher distances in the dehydrated samples while the Mn–N and the Co–N peaks shift to lower distances (Figure 5.3). This shifts indicate that the bond distance Co–C increases while the M–N ( $M = \text{Mn}$  and  $\text{Co}$ ) bond lengths are shortened. The ozonized sample shows a behaviour similar to that of a dehydrated state. This may be linked to the oxidation of the metal coordinated to the nitrogen end of the cyano ligands as was suggested by FTIR analysis.

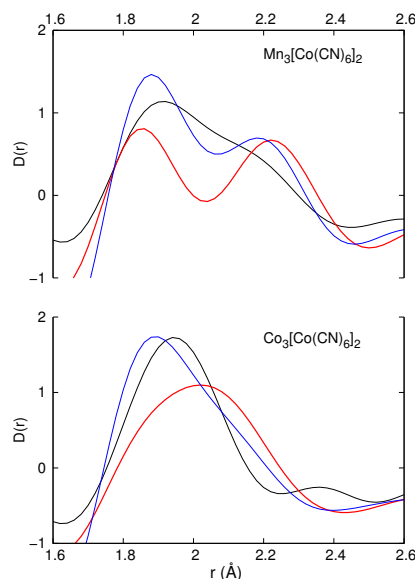


Figure 5.3: Differential correlation function fragment corresponding to the M–N and Co–C bonds in MnHCC and CoHCC: as-synthesized (red line), ozonized (blue line), and dehydrated (black line).

### 5.3 Thermogravimetric analysis

Thermogravimetric curves of MnHCC and CoHCC show two thermal events as a result of dehydration and decomposition processes (Figures 5.4 and 5.5).

Table 5.2: Percent of volume change ( $\Delta V$ ) and cell parameters ( $\text{\AA}$ ) for  $M_3[\text{Co}(\text{CN})_6]_2 \cdot n\text{H}_2\text{O}$  ( $M = \text{Mn}$  and  $\text{Co}$ ) as-synthesized and ozonized.

M	Hydrated	Dehydrated	$\Delta V, \%$	Hydrated Ozonized	$\Delta V, \%$
Mn	10.4228(1)	10.3272(4)	2.7	10.3511(6), 10.2734(8) <sup>a</sup>	2.0 , 4.2
Co	10.2191(5)	10.143(7)	2.2	10.1092(8)	3.2

<sup>a</sup> Two phases were observed in the powder pattern.

Dehydration of CoHCC starts at room temperature and finishes at 313.10 °C (weight loss of 29.48 %). For MnHCC, the same event finishes at 346.26 °C (weight loss of 27.47 %). First derivative curves indicate a maximum dehydration rate at 79.44 °C for CoHCC and at 86.36 °C for MnHCC. On heating, the water is lost through a continuous process independent of its nature (coordinated or non-coordinated water). Non-coordinated water molecules leave the solid together with a fraction of the coordinated ones probably through a cooperative process. In consequence, the thermogravimetric curves show no intermediary inflections (Figures 5.4 and 5.5). The hydration degree of the samples was estimated from weight losses. According to the crystal structure, both as-synthesized samples have six coordinated water molecules per formula unit [22]. Next to these six coordinated water molecules, the estimated numbers of uncoordinated water molecules per formula units for MnHCC and CoHCC were 6.51 and 8.08 respectively, in agreement with the previously reported values [22]. Decomposition events occurs from 346.26 °C to 362.33 °C for MnHCC (23.53 % weight loss) and from 313.10 °C to 326.61 °C for CoHCC (23.89 % weight loss). Both weight losses were associated with the loss of the  $\text{CN}^-$  groups. General dehydration-decomposition models are described in section B.5.

Dehydration events shift to higher temperatures in ozonized frameworks. The ionic hydration enthalpy and the oxidation number are positive correlated ( $\text{Co}^{2+}$ : 1996  $\text{kJ mol}^{-1}$ ,  $\text{Mn}^{2+}$ : 1921  $\text{kJ mol}^{-1}$ ,  $\text{Co}^{3+}$ : 4651  $\text{kJ mol}^{-1}$ ,  $\text{Mn}^{3+}$ : 4544  $\text{kJ mol}^{-1}$ ) [158]. The shift of dehydration events in ozonized samples is consistent with a higher oxidation state of the cations coordinated to the nitrogen end of cyano ligands as suggested in sections 5.1 and 5.2. A complete dehydration of the ozonized samples can not be accomplished without partial decomposition of the frameworks (figures 5.4 and 5.5). This limitation motivated the use of methanol to saturate the samples. Methanol molecules evolve at temperatures lowers than water (figures 5.4 and 5.5).

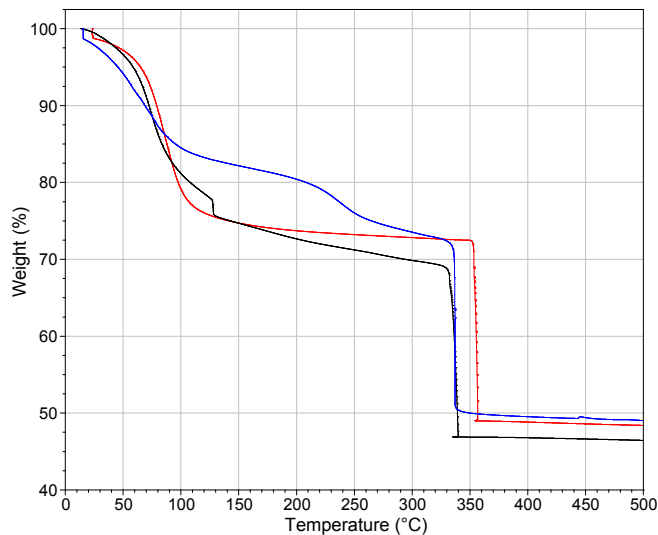


Figure 5.4: Thermogravimetric curves of MnHCC samples: as-synthesized (red), ozonized and hydrated (blue), and ozonized and saturated with methanol (black).

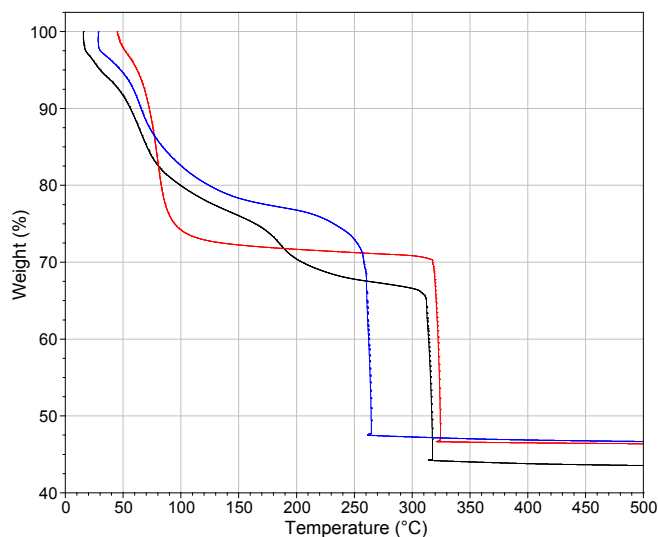


Figure 5.5: Thermogravimetric curves of CoHCC samples: as-synthesized (red), ozonized and hydrated (blue), and ozonized and saturated with methanol (black).

This allows to obtain a higher accessible volume than in hydrated samples at the same temperature. However, a complete removal of the methanol molecules also compromised the framework's integrity.

The starting temperature for the decomposition events decreases after the ozonization (figures 5.4 and 5.5). At this point, almost all solvent molecules have evolved and the framework stability is determined by three bonds: Co–C, C≡N, and N–M (M = Mn and Co). In the formula unit  $M_3[Co(CN)_6]_2$  (M = Mn and Co) there are: 12 Co–C bonds, 12 C≡N bonds and 3 N–M bonds. Most of the C≡N<sup>−</sup> ligands evolve thermally without breaking the triple bond. Consequently, the stability of the framework is mainly determined by metal–ligand bonds. According to sections 5.1 and 5.2, the Co–C bonds become weaker and the N–M are strengthened. The former contributes to lower the starting temperatures for the decomposition events, while the latter increases it. The presence of many more Co–C bonds in the structure results in lower starting temperatures for the decomposition events.

## 5.4 Gas adsorption

The wide shape of the pores size distributions for cobalt and manganese hexacyanocobaltates and the existence of open metal sites in their pores, make these materials interesting molecular sieves [22,159]. Sections 5.1, 5.2 and 5.3 described the effect of ozonization on the: hexacyanocobaltate frameworks, open metal sites and the thermal evolution of adsorbed water and methanol molecules. The cell contraction due to the ozonization, shifts the pore width distribution to lower values while the increase of the oxidation numbers of the open metal sites changes the adsorption energy distributions and the isosteric heat functions. The effect of these changes on water and methanol molecules is the shift of the desolvation event to higher temperatures, as was described in section 5.3. This shift prevents such solvents molecules from being completely removed without compromising the integrity of the framework. In this section, we extend the analysis of adsorption to the retention of two important molecules: H<sub>2</sub> and CO<sub>2</sub>. The analysis will be restricted to samples saturated with methanol because they allow the removal of a greater amount of solvent without compromising the integrity of the lattice (see section 5.3).

It is a great challenge to obtain the equation of an isotherm from a model that takes into account the details of the adsorption process in molecu-

lar sieves with wide pore distributions and pores with heterogeneous surfaces. MnHCC and CoHCC are molecular sieves with at least seven different pores due to vacancies created by the absence of the  $[\text{Co}(\text{CN})_6]^{3-}$  building units [160] and one pore in the unit cell octant. Other types of pores can be formed when vacancies overlap. Besides, surface heterogeneity due to the presence of open metal sites and the residual solvent molecules make the system even more complex. However, adsorbate-adsorbent systems involving: MnHCC, CoHCC,  $\text{H}_2$  and  $\text{CO}_2$  can be treated as a non ideal vacancy solution, similar to the hypothetical solution used in the derivation of Langmuir–Freundlich type isotherm (4.13). The Langmuir-Freundlich equation contains only three parameters: limit capacity ( $n_m$ ), related with accessible volume in the adsorbent; pressure at half volumetric filling ( $p_{1/2}$ ); and the relative activity coefficient exponent ( $g$ ). The last two parameters are related with the isosteric heat of adsorption (equation 4.24). The Langmuir–Freundlich isotherm can provide information about changes in the total pore volumes and in the adsorption energy distributions.

The limit capacity of MnHCC and CoHCC samples is reduced for both  $\text{H}_2$  and  $\text{CO}_2$  after ozonization (Table 5.3). The most likely causes of this reduction are the contraction of cell parameters with the ozonization (Table 5.2) and the existence of some methanol molecules in the porosity. The greatest reduction of the limiting capacity is observed in the MnHCC sample, specially for  $\text{CO}_2$ ; while for the CoHCC sample, the limit capacity remains almost constant. Apparently, the cell contraction combined with the existence of some strongly coordinated methanol molecules, reduces the accessible pore volume. This phenomenon is not observed in  $\text{H}_2$  isotherms due to its lower molar volume.

The Langmuir–Freundlich parameters  $p_{1/2}$  and  $g$  for CoHCC do not change significantly with ozonization (Table 5.3). Therefore, the  $\text{H}_2$  and  $\text{CO}_2$  isosteric heats of adsorption for the as-synthesized and ozonized samples of CoHCC are similar throughout the  $\theta$  range (figure 5.6). The CoHCC sample had to be degassed at temperature 70 K higher than MnHCC to accomplish approximately the same weight loss percent. This temperature increment reverted the crystalline structure to the state at which it was before being ozonized as evidenced by the position of the  $\nu_{\text{CN}}$  band (Figure 5.7). MnHCC sample is in general more stable than CoHCC, even in the ozonized state (Figures 5.4 and 5.5). This probably explains the increment in the isosteric heat of  $\text{H}_2$  adsorption observed in the ozonized MnHCC. The access of some  $\text{H}_2$  molecules to modified open metal sites can increase the average interaction.

Adsorbate	Sample	$n_m$ mmol g <sup>-1</sup>	$p_{1/2}$ mmHg	$g$
H <sub>2</sub>	MnHCC	11.1±0.1	202±6	1.22±0.01
	MnHCCOz	9.3±0.1	160±5	1.25±0.02
	CoHCC	10.8±0.2	214±10	1.33±0.02
	CoHCCOz	10.4±0.1	215±8	1.32±0.04
CO <sub>2</sub>	MnHCC	9.2±0.1	589±20	1.220±0.009
	MnHCCOz	6.74±0.03	539±5	0.988±0.003
	CoHCC	7.40±0.06	948±16	1.139±0.003
	CoHCCOz	7.0±0.1	809±31	1.127±0.008

Table 5.3: Limit capacity ( $n_m$ ), pressure at half volumetric filling ( $p_{1/2}$ ) and, relative activity coefficient exponent ( $g$ ), estimated from the fitting of the Langmuir–Freundlich equation to the experimental isotherms: H<sub>2</sub> at 77 K and CO<sub>2</sub> at 273.15 K.

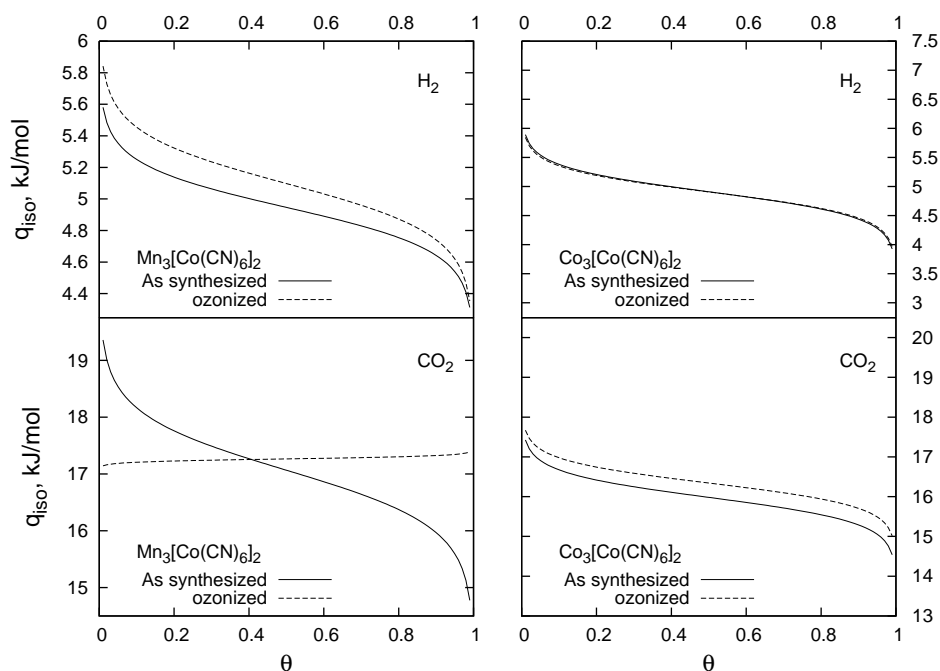


Figure 5.6: Calculated isosteric heat of adsorption for all samples.

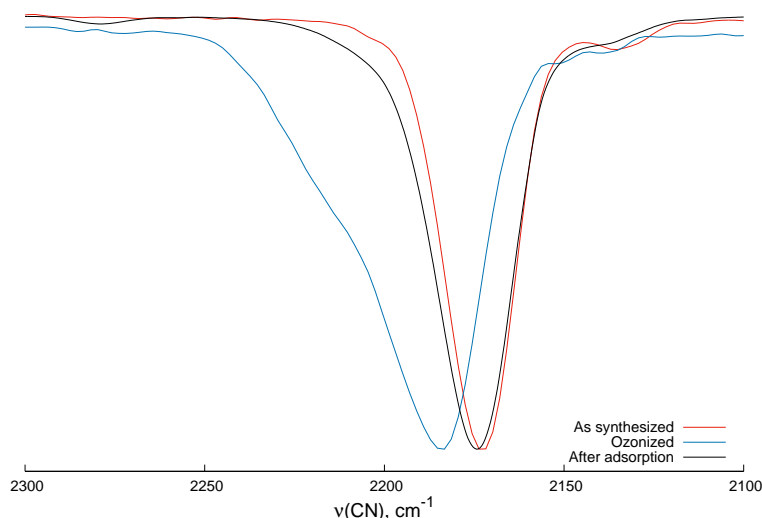


Figure 5.7: FTIR  $\nu_{CN}$  bands of CoHCC: as-synthesized (red), Ozonized (blue) and after adsorption experiment and re-hydration (black).

This tendency changes in the  $\text{CO}_2$  isotherm (Figure 5.6). Four factors could explain this change: the electric quadrupole moment, the characteristic rotational temperature [92, p. 662] (0.561 K for  $\text{CO}_2$  and 88 K for  $\text{H}_2$ ), the experimental temperature (77 K for  $\text{H}_2$  and 273.15 K for  $\text{CO}_2$ ) and the molar volume ( $2.845 \times 10^{-5} \text{ m}^3/\text{mol}$  for  $\text{H}_2$  and  $4.290 \times 10^{-5} \text{ m}^3/\text{mol}$  for  $\text{CO}_2$ ). The open metal sites are positively charged centres and the energy minimum of the quadrupole interaction is reached with molecular axis parallel to the plane of the surface for  $\text{H}_2$  and perpendicular for  $\text{CO}_2$ . The characteristic rotational and experimental temperatures suggest that  $\text{CO}_2$  molecules are rotating while  $\text{H}_2$  ones are not. The increase of molar volume reduces the accessibility of  $\text{CO}_2$  molecules to the pores. Combining all the previous elements and considering that the quadrupolar interaction is a short range interaction, we can conclude that the rotation of the  $\text{CO}_2$  molecule and the collisions derived from the activation of this degree of freedom, lead to an average adsorbate-adsorbent interaction that is weaker than the average adsorbate-adsorbate interaction. The predominance of adsorbate-adsorbate interactions explains the shape of the isosteric heat curve of the MnHCC sample in Figure 5.6 after being treated with ozone, saturated with methanol and partially desolvated.

# Chapter 6

## X-ray photoelectron spectroscopy

In order to determine the effect of Mn and Co oxidation states on the retention capacity and the partial enthalpy of adsorption for different solvents, it is necessary to identify and quantify these oxidation states before and after ozonization. As was mentioned in section 1.7, the X-ray photoelectron spectroscopy is an effective technique to perform this study.

There are some features of MnHCC and CoHCC materials that become a challenge for the identification of the chemical states:

1. Both, Mn and Co are transition metals with a wide variety of possible oxidation states. Their electronic states give rise to additional intensity contributions to their  $2p$  spectra due to a multiplet splitting and these contributions are not normally considered in most data bases [161].
2. Their structural disorder creates an additional electronic heterogeneity. The existence of disordered vacancies can be interpreted as perturbations to the system energy states.
3. XPS is a surface technique. To prepare the sample, usually, the surface is etched using an Ar ion beam. These ions can reduce oxidised surfaces (as MnHCC and CoHCC ozonized samples), making the identification of the chemical states difficult.
4. All bond strengths change after ozonization, making difficult to determine an invariant energy reference to compare new ozonized peaks position with the positions in the as-synthesized materials.

In this Chapter, these difficulties have been considered carefully during the data interpretation: all experimental samples were measured without edging to avoid electric reduction, the correlation between the structural disorder and the increased resolution of the peaks (FWHM) is being discussed and multiplet splitting have been assigned to both transition metals orbitals. The energy reference was taken from Co 2p<sub>3/2</sub> orbital in K<sub>3</sub>[Co(CN)<sub>6</sub>] because this material does not have vacancies to perturb the bond energies distribution function<sup>1</sup>. Additionally, Density Of States calculations (DOS) were performed on as-synthesized materials to support the conclusions about the changes in the valence band due to ozonization.

The experimental results of XPS, measured in ozonized MnHCC and CoHCC samples, reveal changes in their electronic structure related to the oxidation process. These results are discussed in the following sections.

## 6.1 Elemental composition

The semi-quantitative analysis of XPS spectra, measured in all samples, indicates that only the stoichiometric elements are present (See Appendix C, Figure C.2). The elemental composition was evaluated from core levels high resolution spectra, using the atomic sensitivity factors: Co 2p (3.529), Mn 2p (2.688), O 1s (0.733), C 1s (0.314) and N 1s (0.499) taken from reference [139]. The values of the elements atomic fractions in the samples are listed in Appendix C, Table C.1. There is a general excess of carbon, due to atmospheric deposits. These deposits could not been totally eliminated because the samples were not etched using an Ar ion beam, to prevent the reduction of the metal cations and to prevent the destruction of bonds. The amount of water molecules increases in ozonized frameworks, which is consistent with the strengthening of the local electric field around the external cations Mn<sup>2+</sup> and Co<sup>2+</sup> due to their oxidation.

## 6.2 MnHCC as-synthesized and ozonized

Ozone is a powerful oxidant. In general, it can increase the oxidation state of metals. The XPS spectrum of MnHCC suggests the oxidation of manganese

---

<sup>1</sup>The survey spectrum for K<sub>3</sub>[Co(CN)<sub>6</sub>] sample with the corresponding core level assignments is in Appendix C, Figure C.1.

open metal sites by ozone via the reduction of the electronic population near 0 eV (Figure 6.1).

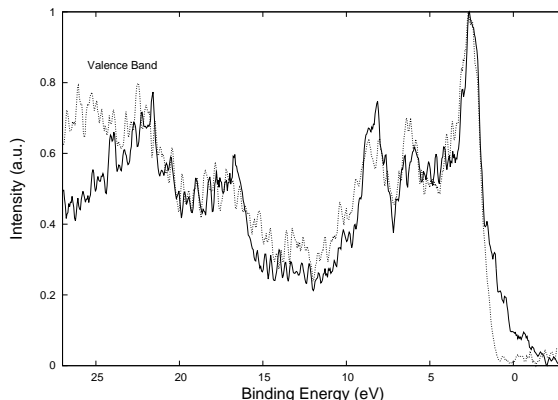


Figure 6.1: XPS spectra valence band of MnHCC as-synthesized (black line) and ozonized (dashed line).

DOS calculations support this conclusion (Figure 6.2). The valence to conduction band transition is primarily influenced by  $d$  orbitals from the transition metals inside the structures. The electronic population near the Fermi level (0 eV), highlighted with a dotted line, belongs entirely to  $\text{Mn}^{2+}$   $3d$  orbitals (blue line). The  $\text{Co}^{3+}$   $3d$  orbitals peak has no contribution to the conduction band because there are no electrons at the Fermi level. Taking the latter into consideration, changes in the electronic structure after ozonization can be explained as follows. The interaction of the ozone molecule with the framework occurs directly at the  $\text{Mn}^{2+}$  exposed metal sites, causing them to oxidise. As a result of the increment of the positive electric field around the Mn cations, electrons in the conduction band in the as-synthesized MnHCC are now more localized, which decreases the electronic population near 0 eV.

All core levels peaks shift after ozonization (Figures 6.3, Table 6.1), except those related to the Co  $2p_{3/2}$  orbital which was taken as a reference. The core level Mn  $2p_{3/2}$  shifts 0.23 eV to higher energies (Table 6.1). This increase in bonding energy is related to a population reduction in the valence band which increases the effective charge of the nucleus and hence the binding energy of core level Mn 2p electrons.

The core level N 1s in ozonized MnHCC shifts to higher energies (Figure 6.3). Binding energies of the N–Mn and N≡C bonds, were estimated by deconvolution of core level N 1s (Appendix C, Figure C.6). They both

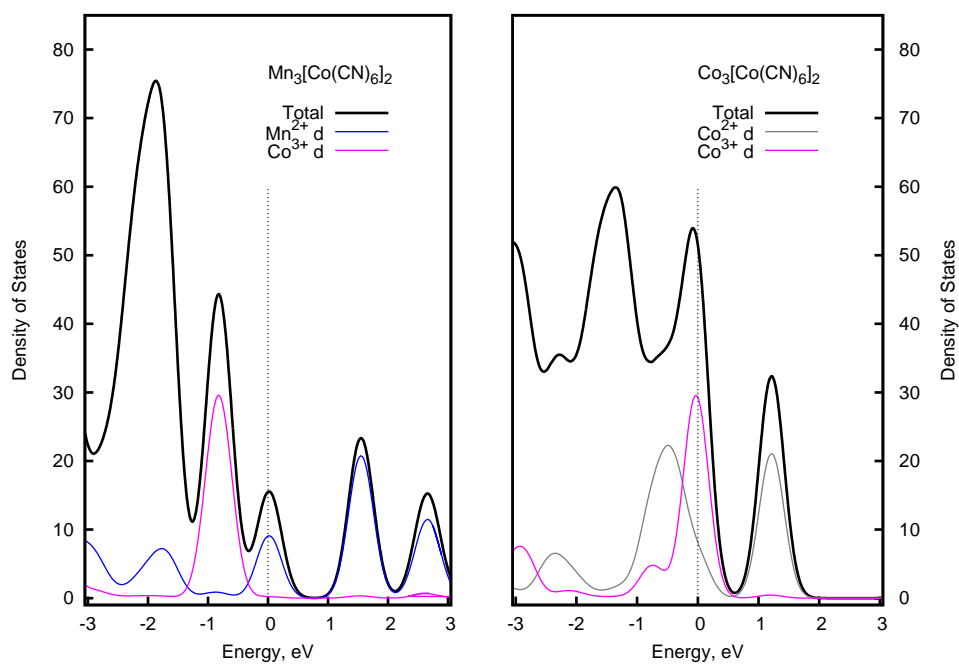


Figure 6.2: Total and partial density of states plot for as-synthesized MnHCC and CoHCC samples: Total electronic contribution to the valence band (black continuous line),  $d\text{Mn}^{2+}$  (blue lines),  $d\text{Co}^{2+}$  (gray line) and  $d\text{Co}^{3+}$  (pink line). The level of 0 eV is highlighted with a dashed line.

Table 6.1: Binding energies (BE) and energies resolution (FWHM) for MnHCC as-synthesized and ozonized samples\* .

Core level	Bond	as-synthesized		ozonized		$\Delta$ BE (eV)	$\Delta$ FWHM (eV)
		BE (eV)	FWHM (eV)	BE (eV)	FWHM (eV)		
Co 2 p <sub>3/2</sub>	Co–C	781.90	1.25	781.90	1.25	0.00	0.00
Mn 2 p <sub>3/2</sub>	Mn–N	641.68	2.90	641.91	2.80	0.23	–0.10
N 1s	N–Mn	398.71	1.61	398.93	1.45	0.22	–0.16
	N≡C	398.27	1.15	398.33	1.19	0.06	0.04
C 1s	C≡N	285.17	1.12	285.10	1.27	–0.7	0.15
	C–Co	284.45	1.63	284.70	1.76	0.25	0.13

\* Error estimated for energy values is 5% including background extraction and deconvolution peaks. All statistic errors in deconvolution peaks (reduced  $\chi^2$ ) are less than 2%.

increase after ozonization (table 6.1). The electron density of nitrogen  $p$  orbitals decreases in N–Mn bond after ozonization due to the reduction of Mn atoms capacity to donate charge through  $\pi$  back-bonding donation. The geometry of the  $p$  orbitals allows their electrons to stay close to the nucleus and to shield the nucleus interaction with 1s electrons. The reduction of  $p$  orbitals shielding, increases the electric interaction between the 1s electrons and the nucleus, increasing the binding energy. The binding energy of the peak assigned to N≡C bonds slightly rises after ozonization. The reduction of the  $\pi$  back-bonding donation of manganese atom to the antibonding C≡N orbitals after ozonization strengthens the C≡N bond making it shorter. This result is consistent with evidence provided by infrared and total diffraction experiments (sections 5.1 and 5.2). Both, nitrogen and carbon has  $sp$  hybridization in this bond. The  $sp$  orbitals form a  $\sigma$  bond. In addition, each atom has two half-occupied  $p$  orbitals oriented at right angles to each other and to the interatomic axis. These two sets of parallel and adjacent  $p$  orbitals merge into two sets of  $\pi$  orbitals. The reduction of C≡N bond distance confine the  $\sigma$  and  $\pi$  bonds to smaller volumes causing an increase in the shielding of nitrogen and carbon 1s orbitals. However, part of the electron density of nitrogen atom is transferred to manganese atom. The result of both processes combined is a small increase in binding energy (Table 6.1, Figure C.6).

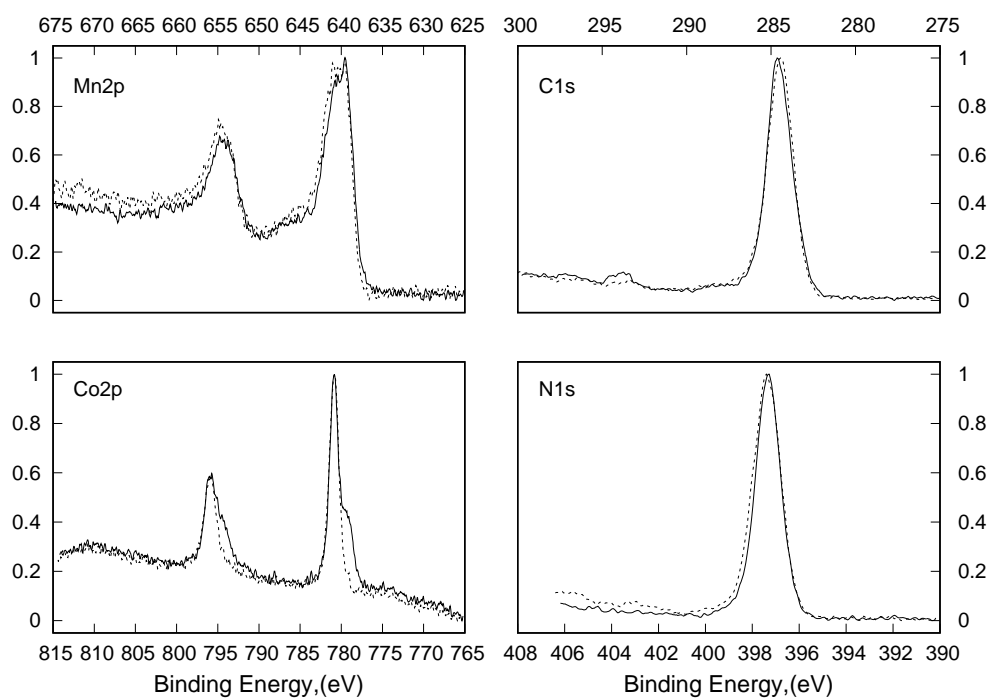


Figure 6.3: XPS spectra of: C 1s, N 1s, Mn 2p and Co 2p in MnHCC as-synthesized (continuous line) and ozonized (dashed line).

The core level C 1s in carbon atoms shifts to a lower energy (Figure 6.3). Deconvoluted curves assigned to the binding energies for C–Co and C≡N bonds show different behaviours after ozonization (see Figure C.5 and Table 6.1). The binding energy for cobalt atom in C≡N bonds decreases. The strengthening of the C≡N bonds confine the  $\sigma$  and  $\pi$  bonds to smaller volumes causing an increase in the shielding of carbon 1s orbitals, decreasing the C≡N curve binding energy. To explain the increase in the binding energy of C–Co curve, the total diffraction experimental evidence in section 5.2 must be considered. This evidence indicates a weakening of the Co–C bond. When Co–C bond is elongated, the  $\pi$  back-bonding donation from cobalt  $d$  electrons is reduced, the shielding effect of  $d$  electrons to 1s electrons is also reduced and hence, the binding energy of the C–Co bond increases. This result is consistent with the decrease of the energy resolution of the core level Co  $2p_{3/2}$  for the MnHCC ozonized sample, compared to the corresponding peak in the as-synthesized one: when the covalent Co–C bond becomes weaker, its polarization increases and as a consequence, there is an increase in the effective positive charge of the Co ion. Due to this increase, the core electrons of the Co ion are more strongly attracted by the nucleus, which explains the disappearance of Co  $2p_{3/2}$  shoulder in Figure 6.3.

### 6.3 CoHCC as-synthesized and ozonized samples

As in the MnHCC case, the CoHCC spectrum indicates the oxidation of cobalt open metal sites by ozone as well as a reduction of the electronic population near 0 eV (Figure 6.4, Valence Band). This experimental observation is supported by DOS calculations (Figure 6.2). The transition of the valence band to the conduction band in this materials, is primarily influenced by the Co<sup>3+</sup>  $3d$  and Co<sup>2+</sup>  $3d$  orbitals. Both contribute to the Fermi level but the most significant contribution comes from the Co<sup>3+</sup>  $3d$  orbital. This phenomenon can be understood considering that Co<sup>3+</sup> ([Ar]  $3d^6$  with a low spin configuration) has six electrons in only three mixed orbitals, which increases the electron repulsion as opposed to the repulsion in the Co<sup>2+</sup> orbitals ([Ar]  $3d^7$ ), where electrons are distributed among the five  $d$  orbitals (high spin configuration). Therefore, the  $d$  electrons in the Co<sup>2+</sup> cations have less energy than the electrons in the Co<sup>3+</sup> cations. As a consequence  $d$  electrons from Co<sup>2+</sup> are more distant from the Fermi level than those from Co<sup>3+</sup>.

As was previously explained for MnHCC, ozone interact only with the

$\text{Co}^{2+}$  cations due to the framework steric factor impediment to access the  $\text{Co}^{3+}$  sites. However, the experimental data (Figure 6.4, Valence band) suggests a reduction of the electronic population of  $d$  orbitals for both cations (Figure 6.2). The electronic population of  $\text{Co}^{2+}$   $d$  orbitals is reduced by a direct interaction with ozone molecules. In the  $\text{Co}^{3+}$  case, the reduction of the  $d$  orbitals population is an indirect consequence of the reaction with ozone. The oxidation of  $\text{Co}^{2+}$  cations shifts the electron density of nitrogen atoms towards the  $\text{Co}^{2+}$  cations via  $\sigma$  bond. This shift increases the electronegativity of carbon atoms in the CN ligands, favouring the ionic character of the C–Co bonds. The increase of the bond’s ionic character, results in the reduction of the population of  $d$  electrons from the  $\text{Co}^{3+}$  sites, and is consistent with the C–Co bond weakening (section 5.2).

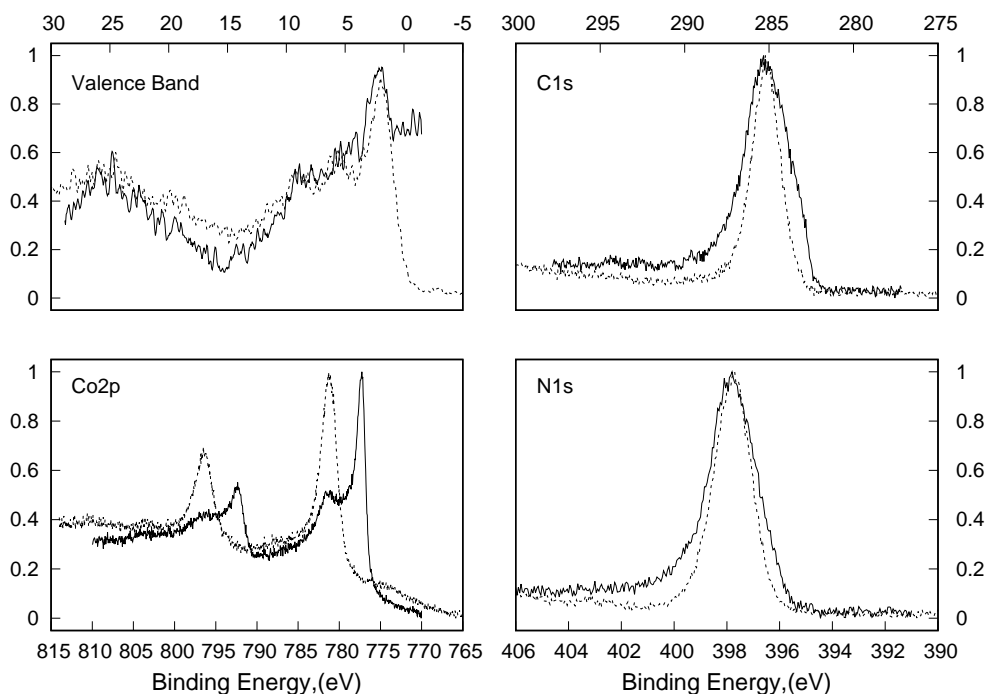


Figure 6.4: XPS spectra of: C 1s, N 1s, valence band and Co 2p in CoHCC as-synthesized (continuous line) and ozonized (dashed line).

The core level  $\text{Co}2p_{3/2}$  for as-synthesized CoHCC sample shows two peaks (Figure 6.4, Table 6.2), one at 777 eV (assigned to  $\text{Co}^{2+}$ ) and the other at

Table 6.2: Binding energies (BE) and energies resolution (FWHM) for as-synthesized and ozonized CoHCC samples\*.

Core level	Bond	as-synthesized		ozonized		$\Delta$ BE (eV)	$\Delta$ FWHM (eV)
		BE (eV)	FWHM (eV)	BE (eV)	FWHM (eV)		
Co 2p <sub>3/2</sub>	Co–C	781.90	1.85	781.90	1.85	0.00	0.00
	Co–N	777.79	1.30	-	-	-	-
N 1s	N–Co	399.07	2.07	399.18	1.50	0.11	–0.57
	N≡C	398.10	1.89	398.32	1.48	0.22	–0.41
C 1s	C≡N	285.23	1.95	285.27	1.37	0.04	–0.58
	C–Co	283.81	2.21	284.60	1.63	0.79	–0.58

\* Error estimated for energy values is 5% including background extraction and deconvolution peaks. All statistic errors in deconvolution peaks (reduced  $\chi^2$ ) are less than 2%.

782 eV (assigned to Co<sup>3+</sup>) [161]. After ozonization, the peak assigned to Co<sup>2+</sup> disappears and the only oxidation state for cobalt ions has Co<sup>3+</sup> binding energy. This experimental observation confirm the total oxidation of Co<sup>2+</sup> to Co<sup>3+</sup>.

The core level N 1s in the ozonized CoHCC, does not significantly shifts to higher energies (Figure 6.4). Deconvoluted binding energies for N–Co and N≡C bonds (Figure C.6), increase after ozonization (table 6.2). As in the MnHCC case, the electron density of nitrogen *p* orbitals decreases in N–Co bond after ozonization due to the reduction of Co atoms capacity to donate charge through  $\pi$  back-bonding donation. The reduction of the *p* orbitals shielding, increases the electric interaction between 1s electrons and the nucleus, thus increasing the binding energy. The increase of the binding energy of the N≡C bonds can be explained by a reduction of the  $\pi$  back-bonding donation of the cobalt atom to the antibonding C≡N orbitals after ozonization. This reduction strengthens the C≡N bond making it shorter. This result is consistent with evidence provided by IR experiments (sections 5.1). The reduction of the C≡N bond distance confines the  $\sigma$  and  $\pi$  bonds to smaller volumes causing an increase in the shielding of nitrogen and carbon 1s orbitals. However, part of the electron density of nitrogen atom is transferred to the manganese atom resulting in an increase in the binding energy.

In the C 1s core level, both C $\equiv$ N and C–Co binding energies, increase with ozonization (Table 6.2 and Figure C.5). Probably, the electronic population of the *d* orbitals is reduced after the combined action of the C $\equiv$ N bond contraction and the C–Co bond elongation.

Core levels C1s and N1s show a decrease of the energy resolution (FWHM) after ozonization (Figure 6.4, Table 6.2), indicating an increase in the local symmetry around the CN ligands. The fact that C 1s and N 1s core level peaks were wider in as-synthesized samples can be explained as follows. Even when the structural chain Co<sup>3+</sup>–C $\equiv$ N–Co<sup>2+</sup> is consistent with the stoichiometry in the as-synthesized sample, it just explains the average structure. Considering that both metal cations are relatively close electronic variations of the same element (Co), and that CN bridges are able to transport charge from one cation to the other, then it is possible to assume that the structural disorder will generate a wide range of possible intermediate states with  $2 < n < 3$  for Co<sup>*n*</sup> cobalt ions. After ozonization, the formation of a metastable state with the average structure Co<sup>*m*</sup>–C $\equiv$ N–Co<sup>*m*</sup> ( $m \approx 3$ ), can explain the increase in the local symmetry around CN ligands and hence, explain the stretching of C1s and N1s peaks observed in CoHCC ozonized spectrum (Figure 6.4).

# Conclusions

1. An experimental setup to conduct a post-synthesis modification of oxidation states of open metal sites in MnHCC and CoHCC frameworks was designed and implemented. The samples were degassed, ozonized and saturated with methanol in the system, preventing any exposure to the atmosphere.
2. The framework of both MnHCC and CoHCC, interacts with a mixture of dry air and ozone. Ozone molecules oxidize the metals coordinated to the nitrogen end of the cyano ligands. The Mb–N bond distance decreases and Co–C bond distance increases after ozonization. The net effect is the reduction of the unit cell volume.
3. The interaction with ozone shifted the desolvation events of water and methanol to higher temperatures overlapping with the corresponding decomposition events. This overlapping prevented a complete framework degassing without compromising the integrity of the crystal lattice. The shift in the desolvation temperatures suggested a modification of the Adsorption Energy Distribution.
4. The MnHCC isobaric thermal expansion coefficient in the partially dehydrated is a linear function of temperature: negative from 275 K to 382 K, zero at 382 K, and positive from 382 K to 450 K.
5. An adsorption isotherm, able to describe experimental data in these systems was proposed. The energy parameters of this isotherm allowed the estimation, from a single isotherm, of the molar partial enthalpy of adsorption curve as a function of the volume filling.
6. The limiting capacity of H<sub>2</sub> and CO<sub>2</sub> retention, on both materials, was reduced with ozonization. This reduction was caused by a partial

occupation of the adsorption sites by solvent molecules, and a decrease of the unit cell volume. The partial molar enthalpy of CO<sub>2</sub> adsorption does not change significantly, while that of H<sub>2</sub> in MnHCC increases. The coordinated solvent molecules modify the Pore Size Distribution.

7. The electronic density of both MnHCC and CoHCC, changed after ozonization. All Co<sup>2+</sup> cations were oxidized to Co<sup>3+</sup> in CoHCC sample. An energy resolution decrease in C 1s and N 1s core levels suggested an increase in the local symmetry around C≡N ligands. The Mn<sup>2+</sup> cations in MnHCC open metal sites were also oxidized. The oxidation of transition metal cations shifted the Adsorption Energy Distribution of both samples to higher values.

# Bibliography

- [1] P. Azadi, O. R. Inderwildi, R. Farnood, and D. A. King. Liquid fuels, hydrogen and chemicals from lignin: A critical review. *Renewable and Sustainable Energy Reviews*, 21:506–523, 2013.
- [2] C. Song. Global challenges and strategies for control, conversion and utilization of CO<sub>2</sub> for sustainable development involving energy, catalysis, adsorption and chemical processing. *Catalysis today*, 115(1):2–32, 2006.
- [3] G. Marbán and T. Valdés-Solís. Towards the hydrogen economy? *International Journal of Hydrogen Energy*, 32(12):1625–1637, 2007.
- [4] T. J. Barton, L. M. Bull, W. G. Klemperer, D. A. Loy, B. McEnaney, M. Misono, P. A. Monson, G. Pez, G. W. Scherer, J. C. Vartuli, and O. M. Yaghi. Tailored Porous Materials. *Chemistry of Materials*, 11(10):2633–2656, 1999.
- [5] M. Pentimalli, E. Imperi, M. Bellusci, C. Alvani, A. Santini, and F. Padella. Silica–Metal composite for hydrogen storage applications. *Crystals*, 2(2):690–703, 2012.
- [6] J. Li, J. Sculley, and H. Zhou. Metal-Organic Frameworks for separations. *Chemical Reviews*, 112(2):869–932, 2012. PMID: 21978134.
- [7] C. Li, S. Yang, Y. Tsou, J. Lee, and C. Hsieh. Newly designed copolymers for fabricating particles with highly porous architectures. *Chemistry of Materials*, 28(17):6089–6095, 2016.
- [8] J. Breternitz and D. H. Gregory. The search for hydrogen stores on a large scale; a straightforward and automated Open database analysis as a first sweep for candidate Materials. *Crystals*, 5(4):617–633, 2015.

- [9] N. S. Bobbitt, J. Chen, and R. Q. Snurr. High-throughput screening of Metal-Organic Frameworks for hydrogen storage at cryogenic temperature. *The Journal of Physical Chemistry C*, 120(48):27328–27341, 2016.
- [10] M. P. Suh, H. J. Park, T. K. Prasad, and D. Lim. Hydrogen storage in Metal-Organic Frameworks. *Chemical Reviews*, 112(2):782–835, 2012.
- [11] E. S. Sanz-Pérez, C. R. Murdock, S. A. Didas, and C. W. Jones. Direct capture of CO<sub>2</sub> from ambient air. *Chemical Reviews*, 116(19):11840–11876, 2016. PMID: 27560307.
- [12] K. Sumida, D. L. Rogow, J. A. Mason, T. M. McDonald, E. D. Bloch, Z. R. Herm, T. Bae, and J. R. Long. Carbon dioxide capture in Metal-Organic Frameworks. *Chemical Reviews*, 112(2):724–781, 2012. PMID: 22204561.
- [13] A. Züttel, A. Borgschulte, and L. Schlapbach. *Hydrogen as a future energy carrier*. John Wiley & Sons, 2011.
- [14] J. C. Orr, V. J. Fabry, O. Aumont, L. Bopp, S. C. Doney, R. A. Feely, A. Gnanadesikan, N. Gruber, A. Ishida, F. Joos, et al. Anthropogenic ocean acidification over the twenty-first century and its impact on calcifying organisms. *Nature*, 437(7059):681–686, 2005.
- [15] Y. H. Hu and L. Zhang. Hydrogen storage in Metal-Organic Frameworks. *Advanced Materials*, 22(20), 2010.
- [16] H. Shue. Subsistence emissions and luxury emissions. *Law & Policy*, 15(1):39–60, 1993.
- [17] D. A. Keen and A. L. Goodwin. The crystallography of correlated disorder. *Nature*, 521(7552):303–309, 2015.
- [18] C. A. Young and A. L. Goodwin. Applications of pair distribution function methods to contemporary problems in materials chemistry. *Journal of Materials Chemistry*, 21(18):6464–6476, 2011.
- [19] T. R. Welberry. In *Diffuse X-ray scattering and models of disorder*, volume 16 of *IUCr Monograph on Crystallography*. Oxford University Press, 2004.

- [20] M. Dinca and J. R. Long. Hydrogen storage in Microporous Metal-Organic Frameworks with exposed Metal Sites. *Angewandte Chemie International Edition*, 47(36):6766–6779, 2008.
- [21] G. W. Beall, W. O. Milligan, J. A. Petrich, and Basil I. Swanson. Crystal structure and Raman spectral study of ligand substitution in  $\text{Mn}_3[\text{Co}(\text{CN})_6]_2 \cdot x\text{L}$ . *Inorganic Chemistry*, 17(11):2978–2981, 1978.
- [22] J. Roque, E. Reguera, J. Balmaseda, J. Rodríguez-Hernández, L. Reguera, and L.F. Del Castillo. Porous hexacyanocobaltates (iii): Role of the metal on the framework properties. *Microporous and Mesoporous Materials*, 103(1):57–71, 2007.
- [23] M. Ávila, L. Reguera, J. Rodríguez-Hernández, J. Balmaseda, and E. Reguera. Porous framework of  $\text{T}_2[\text{Fe}(\text{CN})_6] \cdot \text{H}_2\text{O}$  with  $\text{T} = \text{Co}$ ,  $\text{Ni}$ ,  $\text{Cu}$ ,  $\text{Zn}$ , and  $\text{H}_2$  storage. *Journal of Solid State Chemistry*, 181(11):2899–2907, 2008.
- [24] L. Reguera, E. Reguera, J. Balmaseda, J. Rodríguez-Hernández, and H. Yee-Madeira. Mixed valences system in cobalt iron cyanide. Microporous structure stability. *Journal of Porous Materials*, 15(6):719–729, 2008.
- [25] L. Reguera, J. Balmaseda, C. P. Krap, M. Avila, and E. Reguera. Hydrogen storage in zeolite-like hexacyanometallates: Role of the building block. *Journal of Physical Chemistry C*, 112(44):17443–17449, 2008.
- [26] L. Reguera, C. P. Krap, J. Balmaseda, and E. Reguera. Hydrogen storage in copper prussian blue analogues: Evidence of  $\text{H}_2$  coordination to the copper atom. *Journal of Physical Chemistry C*, 112(40):15893–15899, 2008.
- [27] L. Reguera, J. Balmaseda, L. F. del Castillo, and E. Reguera. Hydrogen storage in porous cyanometalates: Role of the exchangeable alkali Metal. *Journal of Physical Chemistry C*, 112(14):5589–5597, 2008.
- [28] J. Rodríguez-Hernández, E. Reguera, E. Lima, J. Balmaseda, R. Martínez-García, and H. Yee-Madeira. An atypical coordination in hexacyanometallates: Structure and properties of hexagonal zinc phases. *Journal of Physics and Chemistry of Solids*, 68(9):1630–1642, 2007.

- [29] R. Martínez-García, E. Reguera, J. Balmaseda, G. Ramos, and H. Yee-Madeira. On the of some nickel hexacyanoferrates (II,III). *Powder Diffraction*, 19(3):284–291, 2004.
- [30] R. Martínez-García, E. Reguera, J. Rodríguez, J. Balmaseda, and J. Roque. Crystal structures of some manganese (II) and cadmium hexacyanoferrates (II,III) and structural transformations related to the sorption of cesium. *Powder Diffraction*, 19(3):255–264, 2004.
- [31] A. Yuan, C. Chu, H. Zhou, P. Yuan, K. Liu, L. Li, Q. Zhang, X. Chen, and Y. Li. Syntheses, Crystal Structures and Gas Sorption Properties of Prussian Blue Analogues Constructed from  $[\text{Cr}(\text{CN})_6]^{-3}$  building blocks. *European Journal of Inorganic Chemistry*, 2010(6):866–871, 2010.
- [32] B. Zamora, M. Autie, J. L. Contreras, M. Centeno, and E. Reguera. Separation of Oxygen and Nitrogen by Porous Cyanometallates. *Separation Science and Technology*, 45(5):692–699, 2010.
- [33] J. Song, L. Wang, Y. Lu, J. Liu, B. Guo, P. Xiao, J. Lee, X. Yang, G. Henkelman, and J. B. Goodenough. Removal of interstitial  $\text{H}_2\text{O}$  in hexacyanometallates for a superior cathode of a sodium-ion battery. *Journal of the American Chemical Society*, 137(7):2658–2664, 2015. PMID: 25679040.
- [34] R. Poloni, K. Lee, R. F. Berger, B. Smit, and J. B. Neaton. Understanding trends in  $\text{CO}_2$  adsorption in Metal-Organic Frameworks with Open-Metal Sites. *The Journal of Physical Chemistry Letters*, 5(5):861–865, 2014. PMID: 26274079.
- [35] P. K. Thallapally, R. K. Motkuri, C. A. Fernández, B. P. McGrail, and G. S. Behrooz. Prussian blue analogues for  $\text{CO}_2$  and  $\text{SO}_2$  capture and separation applications. *Inorganic Chemistry*, 49(11):4909–4915, 2010. PMID: 20166714.
- [36] G. Autie-Castro, M. Autie, E. Reguera, J. Santamaría-González, R. Moreno-Tost, E. Rodríguez-Castellón, and A. Jiménez-López. Adsorption and separation of light alkane hydrocarbons by porous hexacyanocobaltates (III). *Surface and Interface Analysis*, 41(9):730–734, 2009.

- [37] H. K. Kim, W. S. Yun, M. B. Kim, J. Y. Kim, Y. S. Bae, J. Lee, and N. C. Jeong. A chemical route to activation of Open Metal Sites in the copper-based Metal-Organic Framework Materials hkust-1 and cu-mof-2. *Journal of the American Chemical Society*, 137(31):10009–10015, 2015. PMID: 26197386.
- [38] A. Takahashi, H. Tanaka, D. Parajuli, T. Nakamura, K. Minami, Y. Sugiyama, Y. Hakuta, S. Ohkoshi, and T. Kawamoto. Historical pigment exhibiting ammonia gas capture beyond standard adsorbents with adsorption Sites of two kinds. *Journal of the American Chemical Society*, 138(20):6376–6379, 2016. PMID: 27147127.
- [39] S. K. Nune, P. K. Thallapally, B. P. McGrail, H. V. Annapureddy, L. X. Dang, D. Mei, N. Karri, K. J. Alvine, M. J. Olszta, B. W. Arey, and A. Dohnalkova. Adsorption kinetics in nanoscale porous coordination polymers. *ACS Applied Materials & Interfaces*, 7(39):21712–21716, 2015. PMID: 26333118.
- [40] B. I. Swanson. Aspects of the structure and bonding in Prussian Blues. Single-Crystal Raman study of trimanganese hexacyanocobaltate hydrate ( $\text{Mn}_3[\text{Co}(\text{CN})_6] \cdot x\text{H}_2\text{O}$ ) and tricadmium bis(hexacyanocobaltate) hydrate ( $\text{Cd}_3[\text{Co}(\text{CN})_6]_2 \cdot x\text{H}_2\text{O}$ ). *Inorganic Chemistry*, 15(2):253–259, 1976.
- [41] J. Fernández Bertrán, J. Blanco Pascual, and E. Reguera Ruiz. The CN stretch of hexacyanometallates as a sensor of ligand-outer cation interactions—I. ferricyanides and cobalticyanides. *Spectrochimica Acta Part A: Molecular Spectroscopy*, 46(5):685 – 689, 1990.
- [42] E. Reguera, JF Bertrán, C. Díaz, J. Blanco, and S. Rondón. Mössbauer and infrared spectroscopic studies of novel mixed valence states in cobaltous ferrocyanides and ferricyanides. *Hyperfine Interactions*, 53(1):391–395, 1990.
- [43] E. Reguera, J. Fernández-Bertrán, C. Díaz, and J. Molerio. Behaviour of prussian blue during its interaction with ozone. *Hyperfine Interactions*, 73(3):285–294, 1992.
- [44] E. Reguera and J. Fernández-Bertrán. Study of the interaction of Ozone with solid ferrocyanides. *European Journal of Solid State and Inorganic Chemistry*, 31:1021–1027, 1994.

- [45] E. Reguera, J. Fernández-Bertrán, and J. Duque. On the interactions of ozone with manganous hexacyanoferrates. *Polyhedron*, 13(3):479–484, 1994.
- [46] P. Moeck, Waseda Y., E. Matsubara, and K. Shinoda. X-ray diffraction crystallography. *Crystal Research and Technology*, 47(11):1210–1211, 2012.
- [47] C. Giacovazzo. *Fundamentals of Crystallography*. Oxford University Press, 2011.
- [48] J. Cartwright and A. Mackay. Beyond crystals: the dialectic of materials and information, 2012.
- [49] W. Clegg A. J. Blake. International union of crystallography texts on crystallography. In *Crystal Structure Analysis: Principles and Practice*, volume 13. Oxford University Press, 2009.
- [50] J.D. Bernal and R.H. Fowler. A theory of water and ionic solution, with particular reference to hydrogen and hydroxyl ions. *The Journal of Chemical Physics*, 1(8):515–548, 1933.
- [51] L. Pauling. The structure and entropy of ice and of other crystals with some randomness of atomic arrangement. *Journal of the American Chemical Society*, 57(12):2680–2684, 1935.
- [52] E. H. Lieb. Residual entropy of square ice. *Physical Review*, 162(1):162, 1967.
- [53] I. D. Glover, G. W. Harris, J. R. Helliwell, and D. S. Moss. The variety of X-ray diffuse scattering from macromolecular crystals and its respective components. *Acta Crystallographica Section B*, 47(6):960–968, Dec 1991.
- [54] Y. Wu, A. Kobayashi, G. J. Halder, V. K. Peterson, K. W. Chapman, N. Lock, P. D. Southon, and C. J. Kepert. Negative Thermal Expansion in the Metal–Organic Framework material  $\text{Cu}_3(1,3,5\text{-benzenetricarboxylate})_2$ . *Angewandte Chemie International Edition*, 47(46):8929–8932, 2008.

- [55] W. Zhou, H. Wu, T. Yildirim, J. R. Simpson, and A.R. Walker. Origin of the exceptional negative thermal expansion in metal-organic framework-5  $\text{Zn}_4\text{O}(1,4\text{-benzenedicarboxylate})_3$ . *Physical Review B*, 78(5):054114, 2008.
- [56] N. Lock, Y. Wu, M. Christensen, L. J. Cameron, V. K. Peterson, A. J. Bridgeman, C. J. Kepert, and B. B. Iversen. Elucidating negative thermal expansion in mof-5. *The Journal of Physical Chemistry C*, 114(39):16181–16186, 2010.
- [57] N. Lock, M. Christensen, Y. Wu, V. K. Peterson, M. K. Thomsen, R. O. Piltz, A. J. Ramirez-Cuesta, G. J. McIntyre, K. Norén, R. Kutteh, et al. Scrutinizing negative thermal expansion in mof-5 by scattering techniques and ab initio calculations. *Dalton Transactions*, 42(6):1996–2007, 2013.
- [58] A. L. Goodwin, M. Calleja, M. J. Conterio, M. T. Dove, J. S. O. Evans, D. A. Keen, L. Peters, and M. G. Tucker. Colossal positive and negative thermal expansion in the framework material  $\text{Ag}_3[\text{Co}(\text{CN})_6]$ . *Science*, 319(5864):794–797, 2008.
- [59] A. D. Fortes, E. Suard, and K. S. Knight. Negative linear compressibility and massive anisotropic thermal expansion in methanol monohydrate. *Science*, 331(6018):742–746, 2011.
- [60] S. Bourrelly, P. L. Llewellyn, C. Serre, F. Millange, T. Loiseau, and G. Férey. Different adsorption behaviors of methane and carbon dioxide in the isotopic nanoporous metal terephthalates mil-53 and mil-47. *Journal of the American Chemical Society*, 127(39):13519–13521, 2005.
- [61] K. L. Mulfort, O. K. Farha, C. D. Malliakas, M. G. Kanatzidis, and J. T. Hupp. An interpenetrated framework material with hysteretic  $\text{CO}_2$  uptake. *Chemistry—A European Journal*, 16(1):276–281, 2010.
- [62] D. W. Bruce, D. O’Hare, and R. I Walton. *Porous materials*, volume 13. John Wiley & Sons, 2011.
- [63] M. J. Cliffe and A. L. Goodwin. PASCAL: a principal axis strain calculator for thermal expansion and compressibility determination. *Journal of Applied Crystallography*, 45(6):1321–1329, 2012.

- [64] R.I. Belousov and S.K. Filatov. Algorithm for calculating the thermal expansion tensor and constructing the thermal expansion diagram for crystals. *Glass Physics and Chemistry*, 33(3):271–275, 2007.
- [65] J. F. Nye. *Physical Properties of Crystals: Their Representation by Tensors and Matrices*. Oxford University Press, 2006.
- [66] Herbert B. Callen. *Thermodynamics and an Introduction to Thermostatistics*. John Wiley and Sons, 1985.
- [67] H. J. Buser, D. Schwarzenbach, W. Petter, and A. Ludi. The crystal structure of prussian blue:  $\text{Fe}_4[\text{Fe}(\text{CN})_6]_3\text{xH}_2\text{O}$ . *Inorganic Chemistry*, 16(11):2704–2710, 1977.
- [68] J. Balmaseda, E. Reguera, J. Rodríguez-Hernández, L. Reguera, and M. Autie. Behavior of transition metals ferricyanides as microporous materials. *Microporous and Mesoporous Materials*, 96(1):222–236, 2006.
- [69] M. Jiang, X. Zhou, and Z. Zhao. Cobalt(II) cyanometallates as new inorganic polymeric Materials for Surface-modification of some conducting substrates. *Berichte der Bunsengesellschaft für physikalische Chemie*, 95(6):720–727, 1991.
- [70] L. Reguera, J. Balmaseda, L.F. Del Castillo, and E. Reguera. Hydrogen storage in porous cyanometalates: role of the exchangeable alkali metal. *The Journal of Physical Chemistry C*, 112(14):5589–5597, 2008.
- [71] J. Rodríguez-Hernández, E. Reguera, E. Lima, J. Balmaseda, R. Martínez-García, and H. Yee-Madeira. An atypical coordination in hexacyanometallates: Structure and properties of hexagonal zinc phases. *Journal of Physics and Chemistry of Solids*, 68(9):1630–1642, 2007.
- [72] C.P. Krap, B. Zamora, L. Reguera, and E. Reguera. Stabilization of cubic and rhombohedral phases of zinc hexacyanocobaltate (III). *Microporous and Mesoporous Materials*, 120(3):414–420, 2009.
- [73] S. S. Kaye and J. R. Long. Hydrogen storage in the dehydrated prussian blue analogues  $\text{M}_3[\text{Co}(\text{CN})_6]_2$  ( $\text{M} = \text{Mn, Fe, Co, Ni, Cu, Zn}$ ). *Journal of the American Chemical Society*, 127(18):6506–6507, 2005.

- [74] S. S. Kaye and J. R. Long. The role of vacancies in the hydrogen storage properties of prussian blue analogues. *Catalysis today*, 120(3):311–316, 2007.
- [75] B. Zamora, A.A. Al-Hajjaj, A.A. Shah, D.V. Bavykin, and E. Reguera. Kinetic and thermodynamic studies of hydrogen adsorption on titanate nanotubes decorated with a prussian blue analogue. *International Journal of Hydrogen Energy*, 38(15):6406–6416, 2013.
- [76] J. Jiménez-Gallegos, J. Rodríguez-Hernández, H. Yee-Madeira, and E. Reguera. Structure of porous copper prussian blue analogues: nature of their high h<sub>2</sub> storage capacity. *The Journal of Physical Chemistry C.*, 114(11):5043–5048, 2010.
- [77] G. W. Beall, W. O. Milligan, J. Korp, and I. Bernal. Crystal structure of trimanganese bis(hexakis(cyano)cobaltate) dodecahydrate and tricadmium bis(hexakis(cyano)cobaltate) dodecahydrate by neutron and X-ray diffraction. *Inorganic Chemistry*, 16(11):2715–2718, 1977.
- [78] J.F. Keggin and F.D. Miles. Structures and formulae of the prussian blues and related compounds. *Nature*, 137(7):577–578, 1936.
- [79] A. Ludi, H. U. Guedel, and M. Rugg. Structural chemistry of Prussian blue analogs. Single-Crystal study of Manganese (II) Hexacyanocobaltate (III),  $\text{Mn}_3[\text{Co}(\text{CN})_6]_2 \cdot x\text{H}_2\text{O}$ . *Inorganic Chemistry*, 9(10):2224–2227, 1970.
- [80] A. Sourav, L. L. Daemen, M. Hartl, D. Williams, J. Summerhill, and H. Nakotte. Thermal expansion in 3d-metal prussian blue analogs. a survey study. *Journal of Solid State Chemistry*, 184(11):2854–2861, 2011.
- [81] A. Ludi and H.U. Güdel. Die struktur der hydrate von  $\text{Co}_3[\text{Co}(\text{CN})_6]_2$  und  $\text{Cd}_3[\text{Co}(\text{CN})_6]_2$ . *Helvetica Chimica Acta*, 51(8):2006–2016, 1968.
- [82] C.P. Krap, J. Balmaseda, L.F. Del Castillo, B. Zamora, and E. Reguera. Hydrogen storage in prussian blue analogues: H<sub>2</sub> interaction with the metal found at the cavity surface. *Energy & Fuels*, 24(1):581–589, 2009.
- [83] J. D. Jackson. *Classical Electrodynamics*. John Wiley & Sons, Inc., 1999.

- [84] J. Roque, B. Zamora, and E. Reguera. Almacenamiento de hidrógeno en nanocavidades: papel de las diferentes fuerzas de adsorción. 2013.
- [85] F. Karadas, H. El-Faki, E. Deniz, C.T. Yavuz, S. Aparicio, and M. Atilhan. {CO<sub>2</sub>} adsorption studies on prussian blue analogues. *Microporous and Mesoporous Materials*, 162, 2012.
- [86] D. R. Lide, editor. *Handbook of Chemistry and Physics*. CRC Press, 2003.
- [87] E. Reguera. Almacenamiento de hidrógeno en nanocavidades. *Revista Cubana de Física*, 26(1):3–14, 2009.
- [88] Y. Zhao, Y. Kim, A.C. Dillon, M.J. Heben, and S.B. Zhang. Hydrogen storage in novel organometallic buckyballs. *Physical review letters*, 94(15):155504, 2005.
- [89] S. Natesakhawat, J. T. Culp, C. Matranga, and B. Bockrath. Adsorption properties of hydrogen and carbon dioxide in prussian blue analogues  $M_3[Co(CN)_6]_2$ , m=co,zn. *The Journal of Physical Chemistry C*, 111(2):1055–1060, 2007.
- [90] K. W. Chapman, P. J. Chupas, E. R. Maxey, and J. W. Richardson. Direct observation of adsorbed H<sub>2</sub>–framework interactions in the prussian blue analogue  $Mn_3^{II}[Co^{III}(CN)_6]_2$ : The relative importance of accessible coordination sites and van der waals interactions. *Chem. Commun.*, pages 4013–4015, 2006.
- [91] M. R. Hartman, V. K. Peterson, Y. Liu, S. S. Kaye, and J. R. Long. Neutron diffraction and neutron vibrational spectroscopy studies of hydrogen adsorption in the prussian blue analogue  $Cu_3[Co(CN)_6]_2$ . *Chemistry of Materials*, 18(14):3221–3224, 2006.
- [92] P. Atkins and J. de Paula. *Physical Chemistry*. W. H. Freeman and Company, seventh edition, 2002.
- [93] O. Knacke, O. Kubaschewski, K. Hesselmann, et al. *Thermochemical properties of inorganic substances*, volume 1. Springer Berlin, 1991.
- [94] K. Jones, J.C. Bailar, et al. *Comprehensive Inorganic Chemistry*. by A.F. Trotman-Dickenson, Pergamon Press, Oxford, 2:323, 1973.

- 
- [95] Robert C. Weast, M. J. Astle, W. H. Beyer, et al. *CRC handbook of chemistry and physics*, volume 1990. CRC press, Boca raton FL, 1989.
- [96] R. Trambarulo, S.N. Ghosh, C.A. Burrus Jr., and W. Gordy. The molecular structure, dipole moment, and g factor of ozone from its microwave spectrum. *The Journal of Chemical Physics*, 21(5):851–855, 1953.
- [97] K. M. Mack and J.S. Muentner. Stark and Zeeman properties of ozone from molecular beam spectroscopy. *The Journal of Chemical Physics*, 66(12):5278–5283, 1977.
- [98] T. Y. Takeshita, B. A. Lindquist, and Dunning Jr. Insights into the Electronic Structure of Ozone and Sulfur Dioxide from Generalized Valence Bond Theory: Bonding in O<sub>3</sub> and SO<sub>2</sub>. *The Journal of Physical Chemistry A.*, 119(28):7683–7694, 2015.
- [99] H. Selig and H. H. Claassen. Raman spectrum of ozone. *Israel Journal of Chemistry*, 6(4):499–500, 1968.
- [100] L.T. Molina and M.J. Molina. Absolute absorption cross sections of ozone in the 185 nm to 350 nm wavelength range. *Journal of Geophysical Research: Atmospheres*, 91(D13):14501–14508, 1986.
- [101] E. Vigroux. Determination des coefficients moyen d'absorption de l'ozone. *Ann. Phys*, 8:709–762, 1953.
- [102] A.C. Aikin, B. Woodgate, and HJP. Smith. Atmospheric ozone determination by solar occultation using the UV spectrometer on the solar maximum mission. *Applied optics*, 21(13):2421–2424, 1982.
- [103] R. Atkinson, D.L. Baulch, RA Cox, R.F. Hampson Jr., J.A. Kerr, M.J. Rossi, and J. Troe. Evaluated kinetic, photochemical and heterogeneous data for atmospheric chemistry: Supplement v. iupac subcommittee on gas kinetic data evaluation for atmospheric chemistry. *Journal of Physical and Chemical Reference Data*, 26(3):521–1011, 1997.
- [104] S. T. Oyama. Chemical and catalytic properties of ozone. *Catalysis Reviews*, 42(3):279–322, 2000.

- [105] W. H. Koppenol. The reduction potential of the couple  $O_3/O_3^{\cdot-}$ : Consequences for mechanisms of ozone toxicity. *FEBS letters*, 140(2):169–172, 1982.
- [106] M. H. William, D.R. Lide, and T.J. Bruno. Crc handbook of chemistry and physics, 2012.
- [107] E. Reguera, J. Fernández-Bertrán, C. Díaz, and J. Molerio. Behaviour of prussian blue during its interaction with ozone. *Hyperfine Interactions*, 73(3):285–294, 1992.
- [108] E. Reguera and J. Fernández-Bertrán. Study of the interaction of ozone with solid ferrocyanides. *European journal of solid state and inorganic chemistry*, 31(11):1021–1027, 1994.
- [109] E. Reguera, J. Fernández-Bertrán, and J. Duque. On the interactions of ozone with manganous hexacyanoferrates. *Polyhedron*, 13(3):479–484, 1994.
- [110] E. Reguera, J.F. Bertrán, C. Díaz, J. Blanco, and S. Rondon. Mössbauer and infrared spectroscopic studies of novel mixed valence states in cobaltous ferrocyanides and ferricyanides. *Hyperfine Interactions*, 53(1):391–395, 1990.
- [111] G. J. Long and F. Grandjean. *Mössbauer spectroscopy applied to inorganic chemistry*, volume 3. Springer Science & Business Media, 2013.
- [112] J. Chastain, R. C. King, and J. F. Moulder. *Handbook of X-ray photoelectron spectroscopy: a reference book of standard spectra for identification and interpretation of XPS data*. Physical Electronics Eden Prairie, MN, 1995.
- [113] C.D. Wagner, A.V. Naumkin, A. Kraut-Vass, J.W. Allison, C.J. Powell, and Rumble J. R. Nist standard reference database 20, version 3.4 (web version). *National Institute of Standards and Technology: Gaithersburg, MD*, 20899, 2003.
- [114] J. F. Moulder, W. F. Stickle, P. E. Sobol, and K. D. Bomben. *Handbook of X-ray Photoelectron Spectroscopy*. Physical Electronic, Inc., 1995.

- [115] B. V. Crist. *Handbooks of monochromatic XPS spectra*. XPS International, 1999.
- [116] D. Briggs and M.P. Seah. *Practical Surface Analysis: Auger and X-ray photoelectron spectroscopy*. Practical Surface Analysis. Wiley, 1990.
- [117] PAW Van der Heide. Multiplet splitting patterns exhibited by the first row transition metal oxides in X-ray photoelectron spectroscopy. *Journal of Electron Spectroscopy and Related Phenomena*, 164(1):8–18, 2008.
- [118] J.H. Van Vleck. The dirac vector model in complex spectra. *Physical Review*, 45(6):405, 1934.
- [119] R. P. Gupta and S. K. Sen. Calculation of multiplet structure of core p-vacancy levels. ii. *Physical Review B*, 12(1):15, 1975.
- [120] M. C. Biesinger, B. P. Payne, A. P. Grosvenor, L. W.M. Lau, A. R. Gerson, and R. St.C. Smart. Resolving surface chemical states in XPS analysis of first row transition metals, oxides and hydroxides: Cr, Mn, Fe, Co and Ni. *Applied Surface Science*, 257(7):2717 – 2730, 2011.
- [121] M. Oku, K. Hirokawa, and S. Ikeda. X-ray photoelectron spectroscopy of manganese-oxygen systems. *Journal of Electron Spectroscopy and Related Phenomena*, 7(5):465–473, 1975.
- [122] H. W. Nesbitt and D. Banerjee. Interpretation of XPS Mn<sub>2p</sub> spectra of mn oxyhydroxides and constraints on the mechanism of MnO<sub>2</sub> precipitation. *American Mineralogist*, 83(3-4):305–315, 1998.
- [123] D. Banerjee and H.W. Nesbitt. XPS study of dissolution of birnessite by humate with constraints on reaction mechanism. *Geochimica et Cosmochimica Acta*, 65(11):1703–1714, 2001.
- [124] D. Banerjee and H.W. Nesbitt. XPS study of reductive dissolution of birnessite by oxalate: Rates and mechanistic aspects of dissolution and redox processes. *Geochimica et Cosmochimica Acta*, 63(19):3025–3038, 1999.
- [125] D. Banerjee and H. W. Nesbitt. Oxidation of aqueous Cr(III) at birnessite surfaces: Constraints on reaction mechanism. *Geochimica et Cosmochimica Acta*, 63(11):1671–1687, 1999.

- [126] J. Ch. Dupin, D. Gonbeau, H. Benqlilou-Moudden, Ph. Vinatier, and A. Levasseur. XPS analysis of new lithium cobalt oxide thin-films before and after lithium deintercalation. *Thin Solid Films*, 384(1):23–32, 2001.
- [127] A. Foelske and H. H. Strehblow. Passivity of cobalt in borate buffer at pH 9.3 studied by x-ray photoelectron spectroscopy. *Surface and interface analysis*, 29(8):548–555, 2000.
- [128] A. P. Grosvenor, S. D. Wik, R. G. Cavell, and A. Mar. Examination of the bonding in binary transition-metal monophosphides mp (M = Cr, Mn, Fe, Co) by X-ray photoelectron spectroscopy. *Inorganic chemistry*, 44(24):8988–8998, 2005.
- [129] N.S. McIntyre and M.G. Cook. X-ray photoelectron studies on some oxides and hydroxides of cobalt, nickel, and copper. *Analytical chemistry*, 47(13):2208–13, 1975.
- [130] J. Van Elp, J.L. Wieland, H. Eskes, P. Kuiper, G.A. Sawatzky, F.M.F. De Groot, and T.S. Turner. Electronic structure of  $\text{CoO}$ , Li-doped  $\text{CoO}$ , and  $\text{LiCoO}_2$ . *Physical Review B*, 44(12):6090, 1991.
- [131] M.A. Langell, F. Gevrey, and M.W. Nydegger. Surface composition of  $\text{Mn}_x\text{Co}_{1-x}\text{O}$  solid solutions by X-ray photoelectron and auger spectroscopies. *Applied Surface Science*, 153(2):114–127, 2000.
- [132] V. M. Jiménez, J. P. Espinós, and A. R. González-Elipe. Control of the stoichiometry in the deposition of cobalt oxides on  $\text{SiO}_2$ . *Surface and interface analysis*, 26(1):62–71, 1998.
- [133] H. Yang, J. Ouyang, and A. Tang. Single step synthesis of high-purity  $\text{CoO}$  nanocrystals. *The Journal of Physical Chemistry B*, 111(28):8006–8013, 2007.
- [134] J. Yang, H. Liu, W. N. Martens, and R. L. Frost. Synthesis and characterization of cobalt hydroxide, cobalt oxyhydroxide, and cobalt oxide nanodiscs. *The Journal of Physical Chemistry C*, 114(1):111–119, 2009.
- [135] W. Clegg, A.J. Blake, J.M. Cole, J.S.O. Evans, P. Main, S. Parsons, and D.J. Watkin. *Crystal Structure Analysis: Principles and Practice*.

- International Union of Crystallography Texts on Crystallography. OUP Oxford, 2009.
- [136] K. Rakness, G. Gordon, B. Langlais, W. Masschelein, N. Matsumoto, Y. Richard, C. Michael Robson, and I. Somiya. Guideline for measurement of Ozone concentration in the process gas from an Ozone generator. *Ozone: Science & Engineering*, 18(3):209–229, 1996.
- [137] A. Boultif and D. Louër. Powder pattern indexing with the dichotomy method. *Journal of Applied Crystallography*, 37(5):724–731, 2004.
- [138] C. L. Farrow, P. Juhas, J. W. Liu, D. Bryndin, E. S. Božin, J. Bloch, Th. Proffen, and S. J. L. Billinge. Pdffit2 and pdfgui: computer programs for studying nanostructure in crystals. *Journal of Physics: Condensed Matter*, 19(33):335219, 2007.
- [139] JH Scofield. Hartree-slater subshell photoionization cross-sections at 1254 and 1487 ev. *Journal of Electron Spectroscopy and Related Phenomena*, 8(2):129–137, 1976.
- [140] ulvac phi.com. ULVAC-PHI, INC. v9.6.0.15, 2016.
- [141] XPS International LLC. Spectral Data Processor v4.1, 2004.
- [142] B. Delley. An all-electron numerical method for solving the local density functional for polyatomic molecules. *The Journal of chemical physics*, 92(1):508–517, 1990.
- [143] B. Delley. From molecules to solids with the dmol 3 approach. *The Journal of chemical physics*, 113(18):7756–7764, 2000.
- [144] J. P. Perdew, K. Burke, and M. Ernzerhof. Generalized gradient approximation made simple. *Physical review letters*, 77(18):3865, 1996.
- [145] H. J. Monkhorst and J. D. Pack. Special points for brillouin-zone integrations. *Physical review B*, 13(12):5188, 1976.
- [146] T. Suzuki, A. Omote, and J. Kuwata. Zero thermal expansion material, November 2 2004. US Patent 6,812,178.
- [147] J.Z. Tao and A.W. Sleight. Very low thermal expansion in TaO<sub>2</sub>F. *Journal of Solid State Chemistry*, 173(1):45–48, 2003.

- [148] J. Evans. Negative thermal expansion materials. *Journal of the Chemical Society, Dalton Transactions*, (19):3317–3326, 1999.
- [149] J.S.O. Evans, T.A. Mary, T. Vogt, M.A. Subramanian, and A.W. Sleight. Negative thermal expansion in  $\text{ZrW}_2\text{O}_8$  and  $\text{HfW}_2\text{O}_8$ . *Chemistry of materials*, 8(12):2809–2823, 1996.
- [150] J. Garai. Physics behind the Debye temperature. *arXiv:physics/0703001v2*, 2009.
- [151] K. W. Chapman, P. J. Chupas, and C. J. Kepert. Direct observation of a transverse vibrational mechanism for negative thermal expansion in  $\text{Zn}(\text{CN})_2$ : An atomic pair distribution function analysis. *Journal of the American Chemical Society*, 127(44):15630–15636, 2005.
- [152] A. L. Goodwin, Karena W. Chapman, and C. J. Kepert. Guest-dependent negative Thermal expansion in nanoporous prussian blue analogues  $\text{M}^{\text{II}}\text{Pt}^{\text{IV}}(\text{CN})_6 \cdot \text{H}_2\text{O}$  ( $0 \leq x \leq 2$ );  $\text{M} = \text{Zn}, \text{Cd}$ . *Journal of the American Chemical Society*, 127(51):17980–17981, 2005.
- [153] B. P. Bering and V. V. Serpinskii. The theory of adsorption equilibrium, based on the thermodynamics of vacancy solutions. *Bulletin of the Academy of Sciences of the USSR, Division of chemical science*, 23(11):2342–2353, 1974.
- [154] A. P. Terzyk, S. Koter, S. Furmaniak, and P. A. Gauden. Incorporating heterogeneity into the Osmotic Theory of Adsorption. *Annales Universitatis Mariae Curie-Skłodowska, SECTIO AA*, LXII(15):156–180, 2007.
- [155] R. Roque-Malherbe. *Adsorption and Diffusion in Nanoporous Materials*. CRC Press, Boca Raton, 2007.
- [156] H. B. Callen. *Thermodynamics and an Introduction to Thermostatistics*. John Wiley & Sons, 1985.
- [157] K. Nakamoto. *Infrared and Raman Spectra of Inorganic and Coordination Compounds, Part B: Applications in Coordination, Organometallic, and Bioinorganic Chemistry*, volume B. John Wiley & Sons, Inc., sixth edition, 2009.

- [158] D. W. Smith. Ionic hydration enthalpies. *Journal of Chemical Education*, 54(9):540, 1977.
- [159] S. Natesakhawat, J. T. Culp, C. Matranga, and B. Bockrath. Adsorption properties of hydrogen and carbon dioxide in prussian blue analogues  $M_3[Co(CN)_6]_2$ ,  $M = Co, Zn$ . *The Journal of Physical Chemistry C*, 111(2):1055–1060, 2007.
- [160] A. Flambard, F. H. Köhler, R. Lescouëzec, and B. Revel. Probing spin density and local structure in the prussian blue analogues  $CsCd[FeCo(CN)_6] \cdot 0.5 H_2O$  and  $Cd_3[FeCo(CN)_6]_2 \cdot 15 H_2O$  with solid-state MAS NMR spectroscopy. *Chemistry – A European Journal*, 17(41):11567–11575, 2011.
- [161] A. Kraut-Vass A. V. Naumkin. Nist standard reference database 20 version 4.1. <https://srdata.nist.gov/xps/Default.aspx>, 2000.
- [162] A. Petric and H. Ling. Electrical conductivity and Thermal expansion of spinels at elevated temperatures. *Journal of the American Ceramic Society*, 90(5):1515–1520, 2007.

# Appendix

# Appendix A

## Complementary results: Single Crystals Diffraction of MnHCC

APPENDIX A. MNHCC SINGLE CRYSTALS DIFFRACTION

---

Table A.1: Experimental unit cell parameter ( $a$ ) and calculated unit cell volume ( $V_c$ ) at different temperatures in MnHCC single crystals. Here,  $n$  is the experiment number. Cooling and heating processes are delimited by horizontal lines: Cooling points (1-7),(23-39) and Heating (7-23),(39-47) points. Points with a zero value for ( $a$ ) indicate a low resolution of the diffraction pattern that prevented its determination.

$n$	$T$ (K)	$a$ (Å)	$V_c$ (Å <sup>3</sup> )
1	250	10.426(4)	1133(1)
2	225	10.412(4)	1129(1)
3	200	10.406(3)	1127(1)
4	175	10.383(3)	1119(1)
5	150	10.383(3)	1119(1)
6	125	10.376(3)	1117(1)
7	100	10.3675(4)	1114.4(1)
8	125	10.373(3)	1116(1)
9	150	10.38(3)	1118(1)
10	175	10.388(4)	1121(1)
11	200	10.401(4)	1125(1)
12	225	10.409(4)	1128(1)
13	250	10.429(4)	1134(1)
14	275	10.437(4)	1137(1)
15	300	10.4135(9)	1129.2(3)
16	325	10.405(4)	1126(1)
17	350	10.383(4)	1119(1)
18	375	10.285(14)	1088(4)
19	400	10.250(9)	1077(3)
20	425	10.229(15)	1070(5)
21	450	10.27(2)	1083(6)
22	475	10.25(1)	1077(3)
23	500	10.223(4)	1068(1)
24	475	0	0
25	450	0	0
26	425	10.261(17)	1080(5)
27	400	0	0
28	375	0	0
29	350	0	0
30	325	0	0
31	300	10.248(5)	1076(2)
32	275	10.259(17)	1080(5)
33	250	10.226(11)	1069(3)
34	225	0	0
35	200	10.221(12)	1068(4)
36	175	10.22(2)	1067(6)
37	150	10.26(1)	1081(3)
38	125	10.254(15)	1078(5)
39	100	10.274(3)	1084(1)
40	125	10.248(12)	1076(4)
41	150	10.261(9)	1080(3)
42	175	10.257(11)	1079(3)
43	200	10.284(16)	1088(5)
44	225	0	0
45	250	0	0
46	275	0	0
47	300	10.245(3)	1075.3(9)

APPENDIX A. MNHCC SINGLE CRYSTALS DIFFRACTION

---

Table A.2: Comparison between linear, polynomial and exponential fitting for  $\ln V$  vs.  $T$  experimental points in hydrated and partially dehydrated phases of MnHCC single crystals. The difference between the experimental values for  $\ln(V_{\text{exp}})$  and calculated ones from the fittings are in the order of the experimental error.

T (K)	$\ln(V_{\text{exp}})$	$\delta \ln(V_{\text{exp}})$ $10^{-3}$	$\ln(V_l)$	$\delta \ln(V_{l-\text{exp}})$ $10^{-3}$	$\ln(V_p)$	$\delta \ln(V_{p-\text{exp}})$ $10^{-3}$	$\ln(V_e)$	$\delta \ln(V_{e-\text{exp}})$ $10^{-3}$
Hydrated								
100	7.016028	0.116	7.014441	-1.586	7.015892	-0.136	7.015711	-0.317
125	7.017619	0.868	7.0174167	-0.202	7.017623	0.00453	7.017659	0.04021
150	7.019643	0.867	7.020392	0.749	7.019770	0.127	7.019884	0.241
175	7.021954	1.155	7.023367	1.414	7.022330	0.376	7.022424	0.470
200	7.025706	1.154	7.026343	0.637	7.025306	-0.400	7.025323	-0.382
225	7.028012	1.153	7.029318	1.306	7.028696	0.683	7.028634	0.622
250	7.033771	1.151	7.032293	-1.478	7.032500	-1.271	7.032414	-1.357
275	7.036072	1.150	7.035269	-0.803	7.036719	0.000648	7.036730	0.658
Partially dehydrated								
300	7.029309	0.259	7.032480	3.170	7.031090	1.781	7.032504	3.195
325	7.026859	1.153	7.025199	-1.661	7.025339	-1.520	7.025186	-1.674
350	7.020510	1.156	7.017918	-2.592	7.019151	-1.359	7.017878	-2.631
450	6.987681	5.842	6.988794	1.113	6.990027	2.346	6.988758	1.077
475	6.981833	2.927	6.981513	-0.320	6.981654	-0.180	6.981505	-0.328
500	6.973920	1.174	6.974233	0.312	6.972843	-1.077	6.974264	0.343

In order to compare our results,  $\alpha$  values for hydrated and dehydrated states were compared with the results obtained from the Pascal software [63].

$$\text{hydrated state: } \alpha_l = (39.7993 \pm 2.4514) \text{ MK}^{-1}$$

$$\alpha = (119 \pm 7) \text{ MK}^{-1}$$

$$\text{dehydrated state: } \alpha_l = (-12.4100 \pm 0.0574) \text{ MK}^{-1}$$

$$\alpha = (-37.2 \pm 0.2) \text{ MK}^{-1}$$

APPENDIX A. MNHCC SINGLE CRYSTALS DIFFRACTION

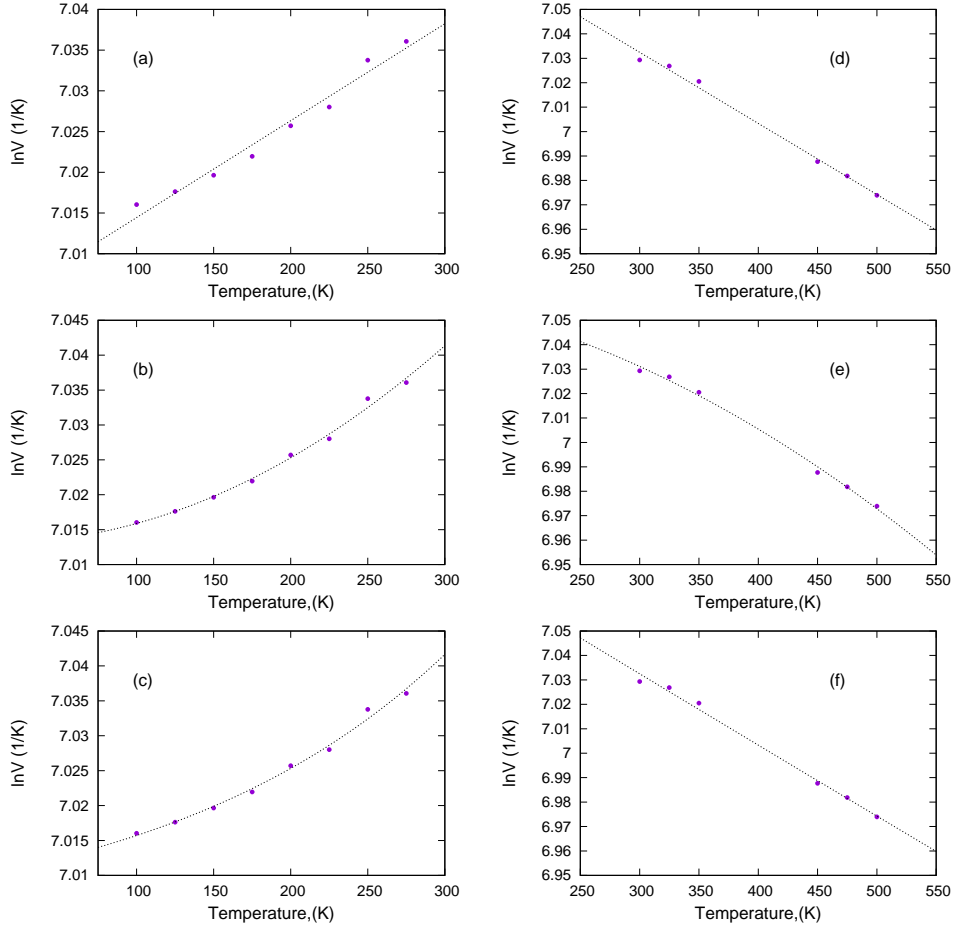


Figure A.1: Experimental points for hydrated phase (left column) and partially dehydrated state (right column) were fitted with different functions: Linear fitting  $[\ln(V) = b \cdot T + a]$  for (a) and (d); a second degree polynomial  $[\ln(V) = c \cdot T^2 + b \cdot T + a]$  in (b) and (e) and finally, exponential  $[\ln(V) = b \cdot e^{cT} + a]$  for (c) and (f).

## Appendix B

### Post-synthesis modification with ozone

## B.1 FTIR spectra of samples

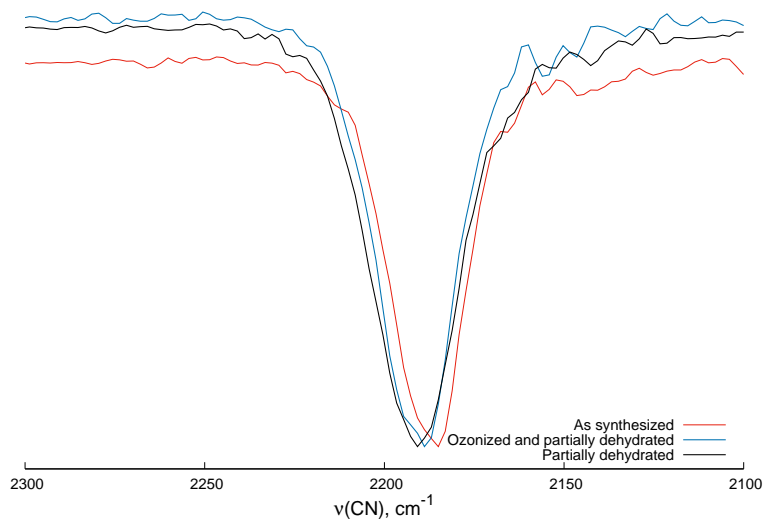


Figure B.1: Section of the  $\nu_{\text{CN}}$  bands of the CuHCC FTIR spectra.

APPENDIX B. POST-SYNTHESIS MODIFICATION WITH OZONE

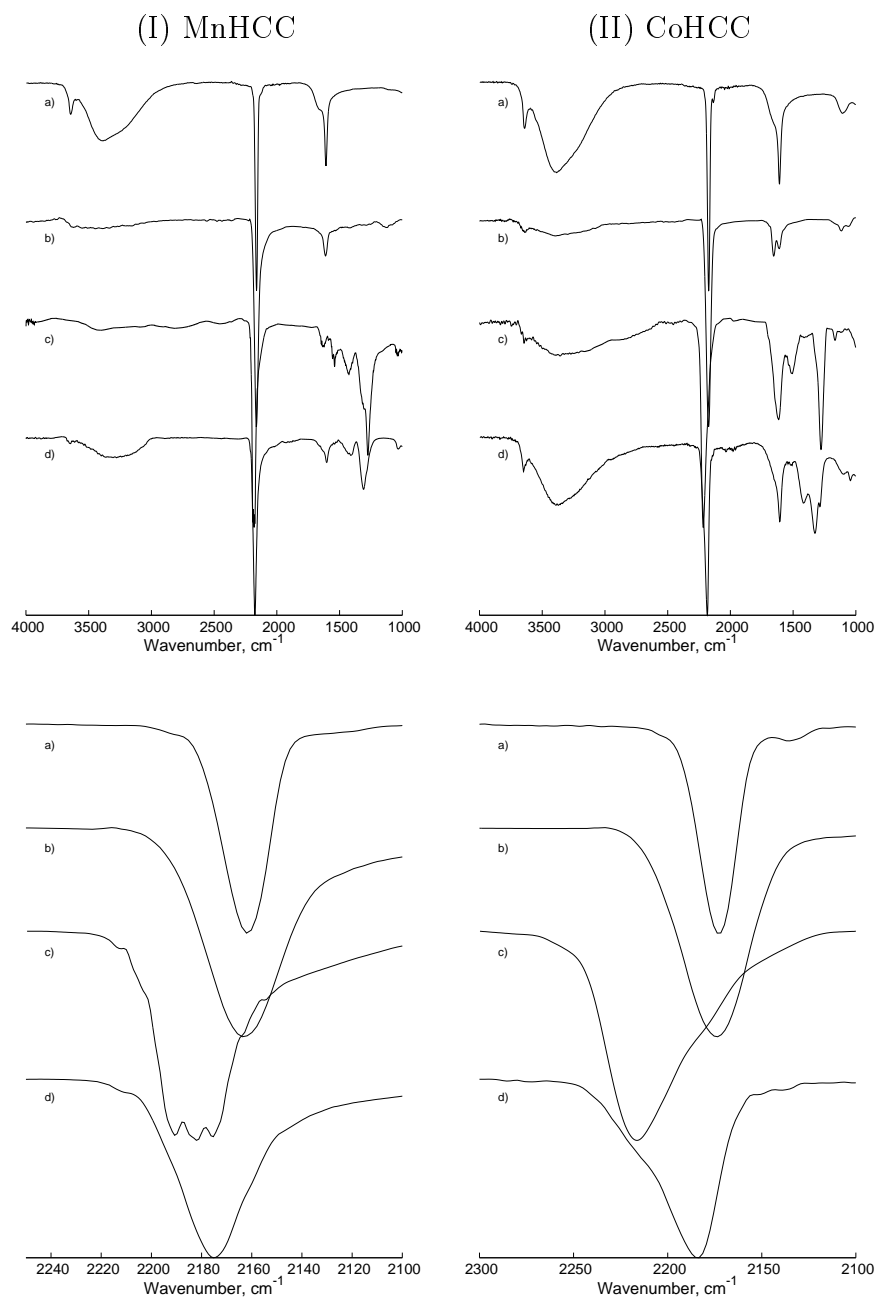


Figure B.2: FTIR spectra of the MnHCC [Column (I)] and the CoHCC [Column (II)] samples: a) as-synthesized, b) partially dehydrated, c) ozonized and partially dehydrated, d) ozonized and hydrated. Below the full spectra, sections of the  $\nu_{CN}$  bands are showed in the same order.

## B.2 Raman spectra of samples

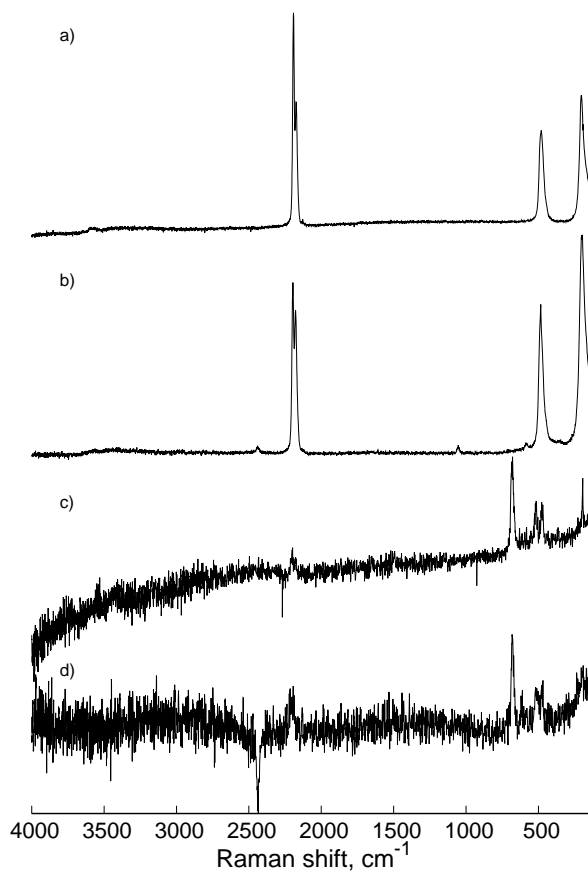


Figure B.3: Full Raman spectra of: a) MnHCC as-synthesized, b) MnHCCOz saturated with methanol and then saturated in a water vapor, c) CoHCC as-synthesized, d) CoHCCOz saturated with methanol and then saturated in a water vapor.

### B.3 X-ray diffraction powder patterns of samples

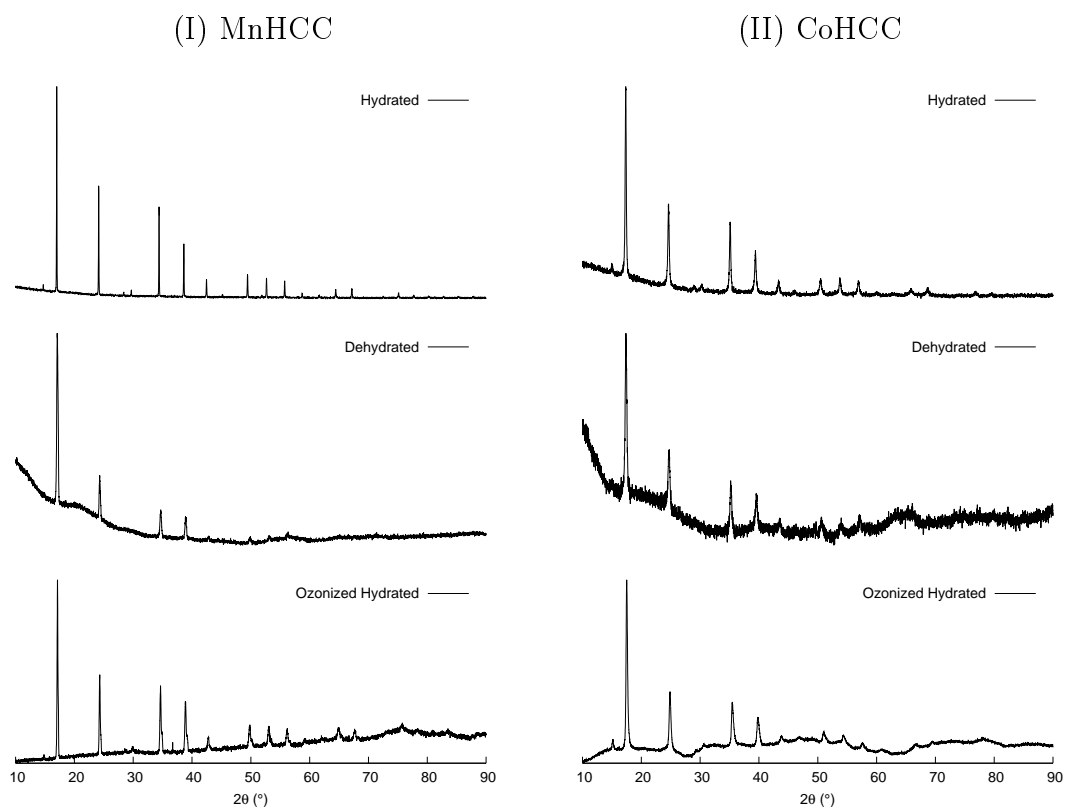


Figure B.4: X-ray diffraction powder patterns of MnHCC and CoHCC samples.

## B.4 Hydrogen and carbon dioxide adsorption

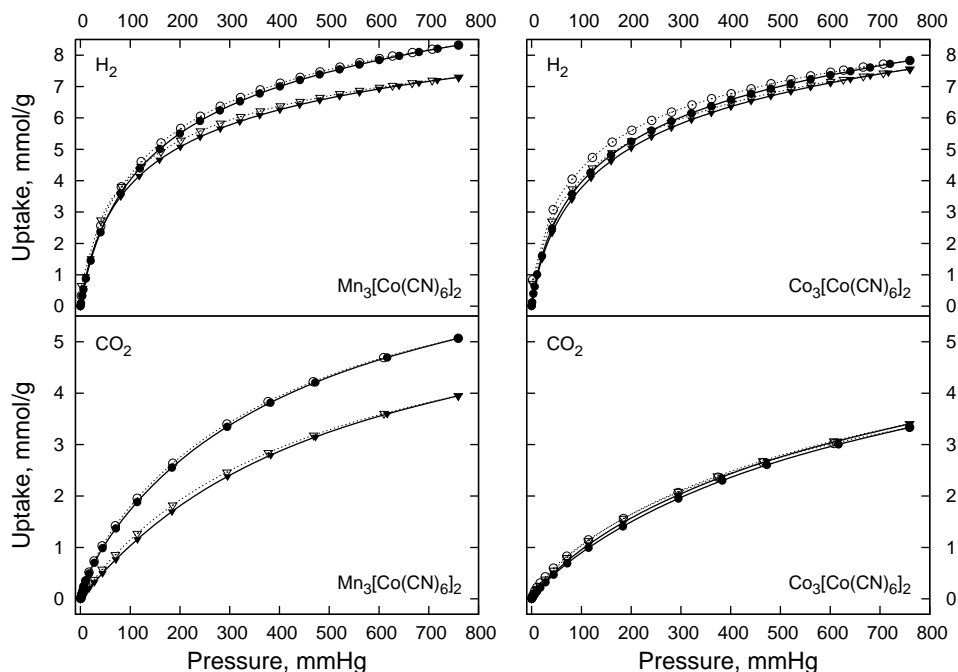


Figure B.5: Hydrogen adsorption isotherms at 77 K and carbon dioxide adsorption isotherms at 273.15 K for the degasified samples. Adsorption branch is plotted with filled symbols and desorption branch with open symbols. The isotherms on the unmodified samples is represented with circles and the isotherms of ozonized samples are represented by triangles. Lines are cubic spline of experimental data to guide the reader.

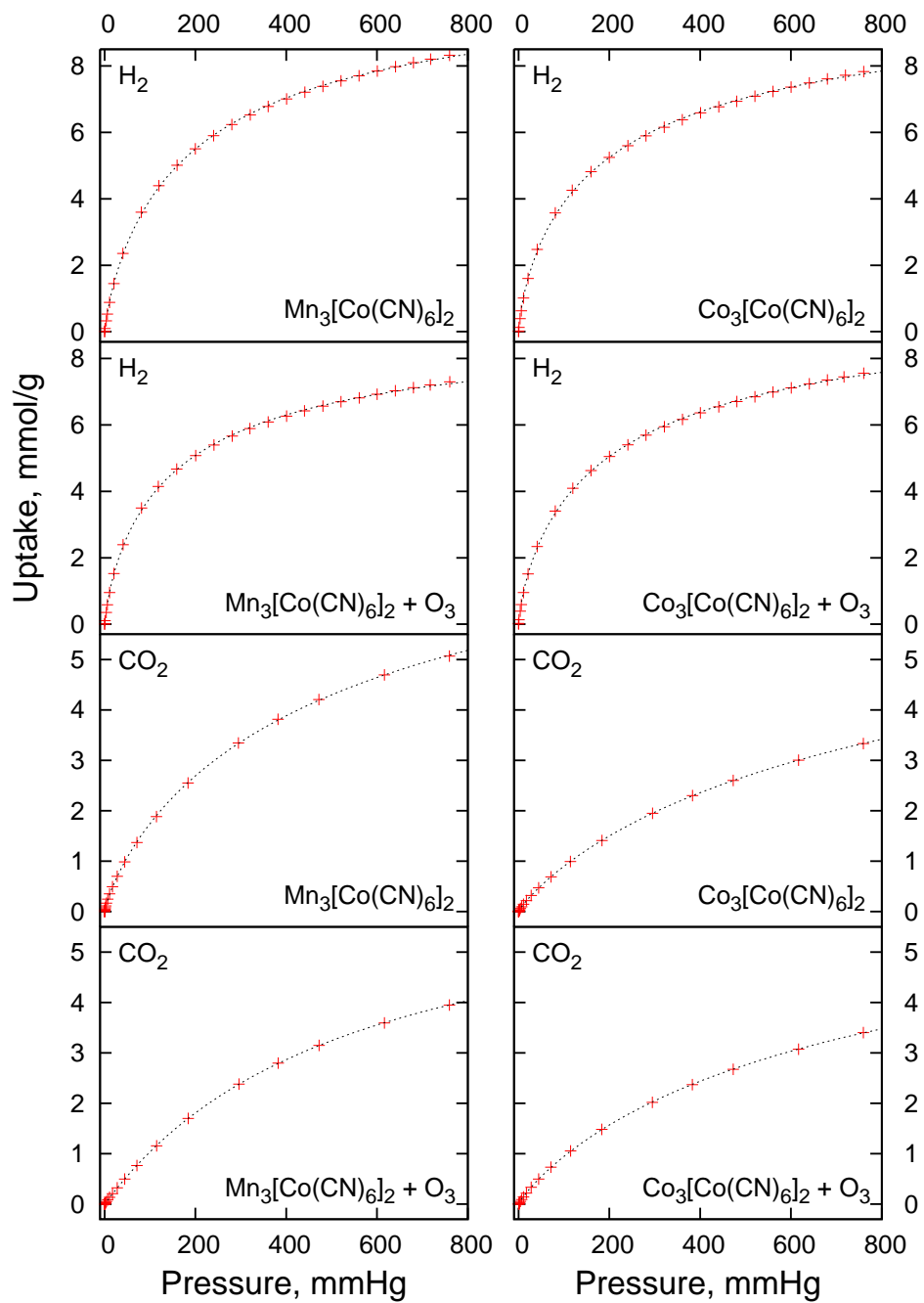


Figure B.6: Langmuir–Freundlich isotherm fit (dashed line) to experimental isotherms (red crosses).

## B.5 Thermogravimetric analysis

Hydrated MnHCC and CoHCC have 6 coordinated water molecules [77]. The number of uncoordinated water molecules changes with the environmental conditions the samples are submitted to. So, the molecular formula for each compound is:



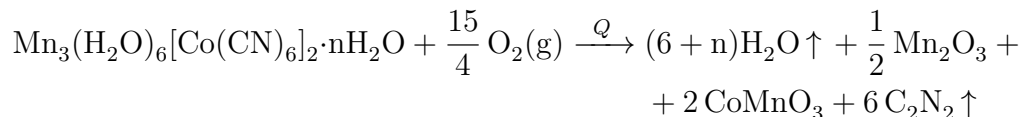
Thermal evolution is described by three events in each case.

### For M=Mn

Reaction of the thermal event	Description
$Mn_3(H_2O)_6[Co(CN)_6]_2 \cdot nH_2O \xrightarrow{Q} Mn_3(H_2O)_6[Co(CN)_6]_2 + nH_2O \uparrow$	Uncoord. $H_2O$
$Mn_3(H_2O)_6[Co(CN)_6]_2 \xrightarrow{Q} Mn_3[Co(CN)_6]_2 + 6 H_2O \uparrow$	Coord. $H_2O$
$Mn_3[Co(CN)_6]_2 + \frac{15}{4} O_2(g) \xrightarrow{Q} \frac{1}{2} \alpha-Mn_2O_3 + 2 CoMnO_3 + 6 C_2N_2 \uparrow$	Decomposition

The Co–Mn phase diagram at 400 °C and  $Co/(Co + Mn) = 0.4$ , suggest the formation of  $\alpha-Mn_2O_3$  and the intermetallic  $CoMnO_3$  [162, Figure 1].

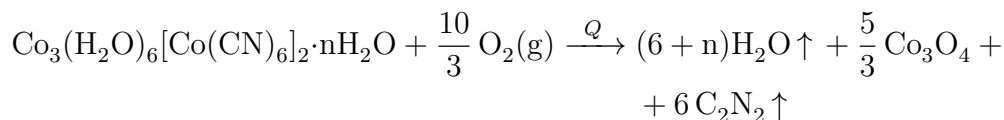
Global reaction is:



### For M=Co

Reaction of the thermal event	Description
$Co_3(H_2O)_6[Co(CN)_6]_2 \cdot nH_2O \xrightarrow{Q} Co_3(H_2O)_6[Co(CN)_6]_2 + nH_2O \uparrow$	Uncoord. $H_2O$
$Co_3(H_2O)_6[Co(CN)_6]_2 \xrightarrow{Q} Co_3[Co(CN)_6]_2 + 6 H_2O \uparrow$	Coord. $H_2O$
$Co_3[Co(CN)_6]_2 + \frac{10}{3} O_2(g) \xrightarrow{Q} \frac{5}{3} Co_3O_4 + 6 C_2N_2 \uparrow$	Decomposition

Global reaction:



APPENDIX B. POST-SYNTHESIS MODIFICATION WITH OZONE

The uncoordinated and coordinated water molecules evolve in one event from room temperature to 346.26 °C for MnHCC with a weight loss of 27.47 % (Figure B.7) and from room temperature to 313.10 °C for CoHCC, with a weight loss of 29.48 % (Figure B.7). The number of uncoordinated water molecules is given in Table B.1.

Table B.1: Molar mass of decomposition reaction components

Fomula	MW, g/mol
$\text{Co}_3(\text{H}_2\text{O})_6[\text{Co}(\text{CN})_6]_2$	714.965
$\text{Mn}_3(\text{H}_2\text{O})_6[\text{Co}(\text{CN})_6]_2$	702.987
$\text{Co}_3\text{O}_4$	240.797
$\text{CoMnO}_3$	161.868
$\text{Mn}_2\text{O}_3$	157.873
$\text{C}_2\text{N}_2$	52.036
$\text{H}_2\text{O}$	18.015
$\text{O}_2$	31.998

$$\frac{18.015(6 + n)}{702.987 + 18.015n} \times 100\% = 27.47\%$$

$$n = 6.51 \text{ uncoordinated H}_2\text{O molecules for MnHCC}$$

$$\frac{18.015(6 + n)}{714.965 + 18.015n} \times 100\% = 29.48\%$$

$$n = 8.08 \text{ uncoordinated H}_2\text{O molecules for CoHCC}$$

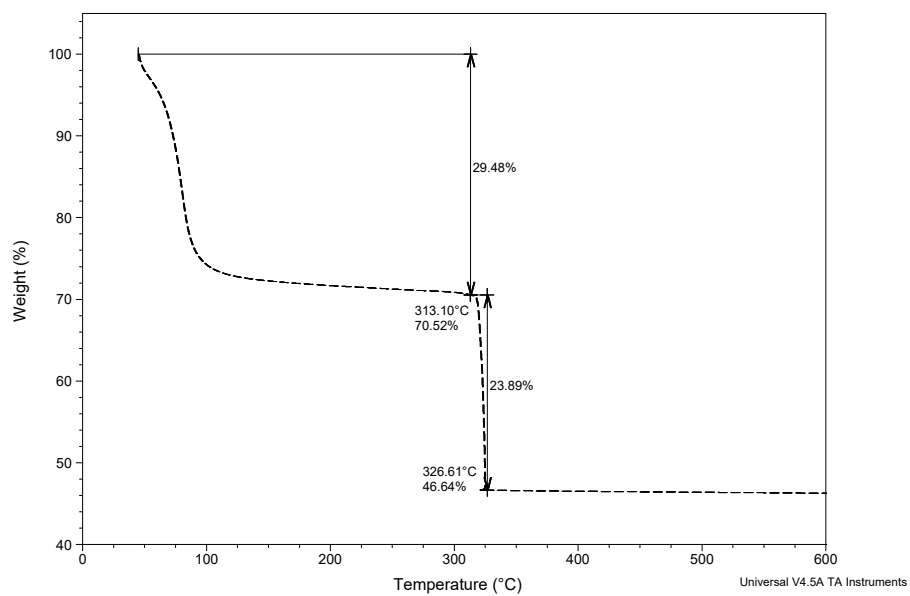
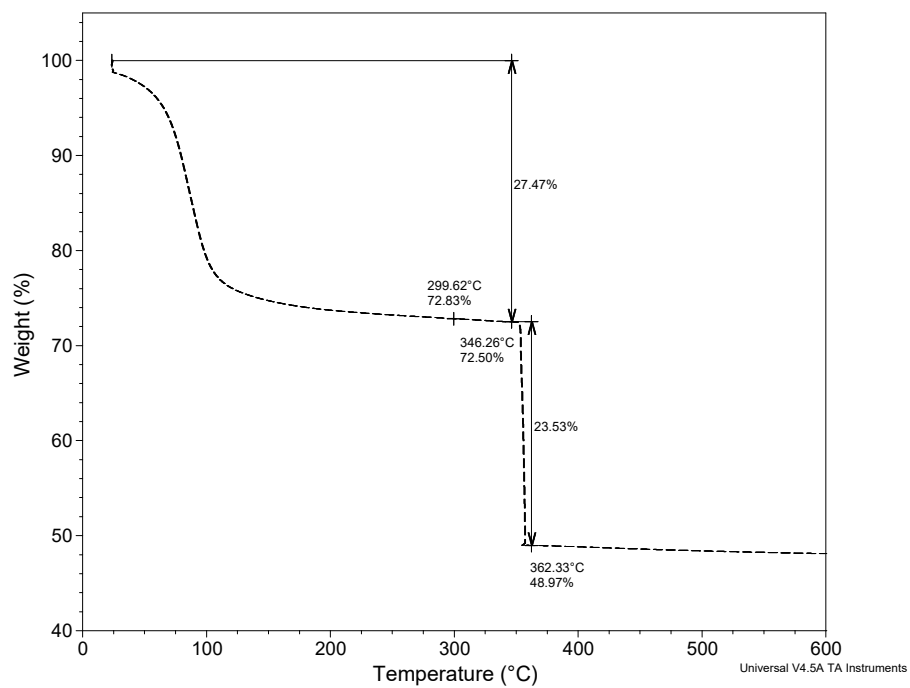
Substituting  $n$  in  $\text{M}_3(\text{H}_2\text{O})_6[\text{Co}(\text{CN})_6]_2 \cdot n\text{H}_2\text{O}$  and estimating the weight percent of the residue in each case:

For  $\text{M} = \text{Mn}$

$$\frac{\frac{1}{2}157.873 + 2 \times 161.868}{702.987 + 6.51 \times 18.015} \times 100\% = 49.09\%$$

The observed value at 362.33 °C was 48.97 % (Figure B.7) with a deviation of 0.24 %.

MnHCC



CoHCC

Figure B.7: TGA curves for as-synthesized MnHCC and CoHCC.

APPENDIX B. POST-SYNTHESIS MODIFICATION WITH OZONE

For M = Co

$$\frac{\frac{5}{3}240.797}{714.965 + 8.082 \times 18.015} \times 100 \% = 46.64 \%$$

The observed value at 326.61 °C was 46.64 % (Figure B.7) in agreement with our result.

To estimate the loss of C<sub>2</sub>N<sub>2</sub> due to the decomposition event, O<sub>2</sub> weight gain should be taken into account.

For M = Mn

$$\frac{6 \times 52.036 - \frac{15}{4}31.998}{702.987 + 6.51 \times 18.015} 100 \% = 23.43 \%$$

The observed weight loss between 346.26 °C and 362.33 °C was 23.53 %.

For M = Co

$$\frac{6 \times 52.036 - \frac{10}{3}31.998}{714.965 + 8.082 \times 18.015} 100 \% = 23.89 \%$$

The observed weight loss between 313.10 °C and 326.61 °C was 23.89 %.

The effect of the O<sub>3</sub> on M<sub>3</sub>[Co(CN)<sub>6</sub>]<sub>2</sub> is a charge transfer from M<sup>2+</sup> to Co<sup>3+</sup>. This charge transfer is reversed at decomposition temperature. So, while the charge transfer affect the thermal evolution of water it does not change the final products and the global reaction of thermal evolution is the same.

To analyze the ozonized thermogravimetric curves, it is important to consider that in these cases the thermal events corresponding to the water evolution and decomposition overlap. So, it is convenient to estimate *n* from the residue.

For M = Mn at 362.33 °C (49.82 %) (Figure B.8)

$$\frac{\frac{1}{2}157.873 + 2 \times 161.868}{702.987 + n \times 18.015} \times 100 \% = 49.82 \%$$

$$n = 5.84 \text{ uncoordinated H}_2\text{O molecules}$$

For M = Co at 266.03 °C (47.46 %)

$$\frac{\frac{5}{3}240.797}{714.965 + n \times 18.015} \times 100 \% = 47.46 \%$$

$$n = 7.25 \text{ uncoordinated H}_2\text{O molecules}$$

APPENDIX B. POST-SYNTHESIS MODIFICATION WITH OZONE

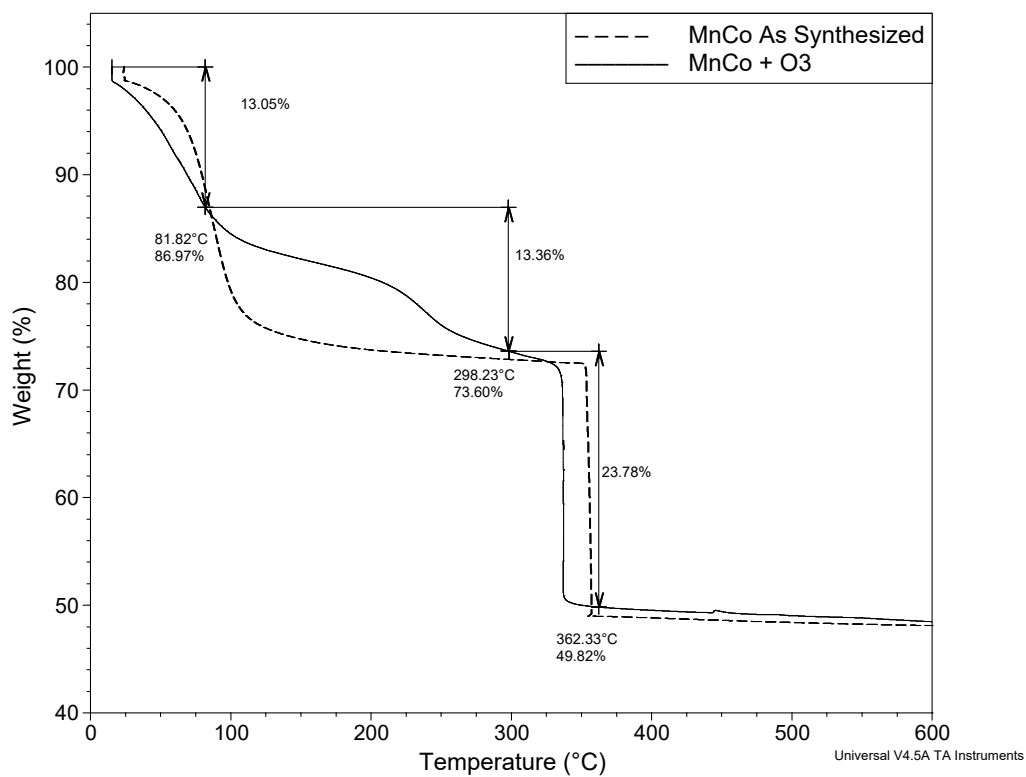


Figure B.8: Thermogram of MnHCC as-synthesized and ozonized.

## APPENDIX B. POST-SYNTHESIS MODIFICATION WITH OZONE

---

These results are consistent with the reduction of cell parameter due to ozonization. The accessible pore volume is reduced as a consequence of the cell parameter reduction. By calculating the weight loss associated to the evolution of  $C_2N_2$  we can estimate the temperature at which the decomposition starts.

For  $M = Mn$

$$\frac{6 \times 52.036 - \frac{15}{4}31.998}{702.987 + 5.84 \times 18.015} 100 \% = 23.78 \%$$

The decomposition process starts at  $298.23^\circ C$  according to Figure B.8. The weight loss due to the coordinated water molecules evolution in ozonized sample is:

$$\frac{6 \times 18.015}{702.987 + 5.84 \times 18.015} \times 100 \% = 13.37 \%$$

According to this value, the evolution of coordinated water molecules start at  $81.82^\circ C$  (Figure B.8).

For  $M = Co$

$$\frac{6 \times 52.036 - \frac{10}{3}31.998}{714.965 + 7.252 \times 18.015} 100 \% = 24.31 \%$$

The decomposition process starts at  $255.33^\circ C$  according to Figure B.9 and the weight loss due to the coordinate water molecules evolution in ozonized sample is:

$$\frac{6 \times 18.015}{714.965 + 7.252 \times 18.015} \times 100 \% = 12.782 \%$$

According to this value, the evolution of coordinated water molecules start at  $86.73^\circ C$ .

The thermogravimetric curves for both materials exhibit similar behaviour after ozonization: for temperatures above  $150^\circ C$ , the weight losses due to dehydration increase, and the decomposition processes begin at lower temperature compared with the corresponding ones in the as-synthesized samples (Figure B.8 and Figure B.9).

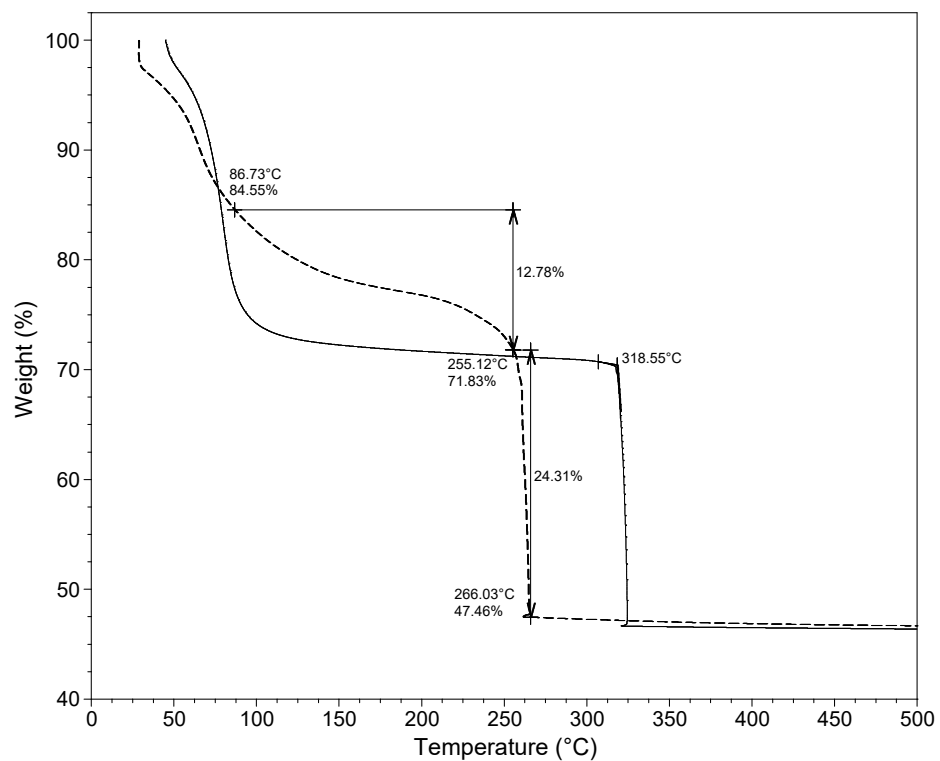
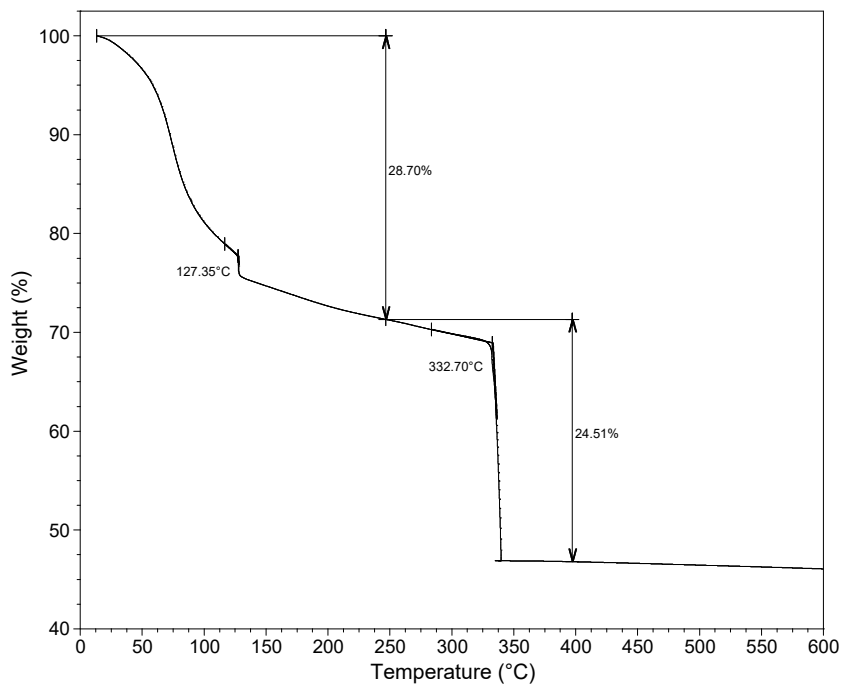
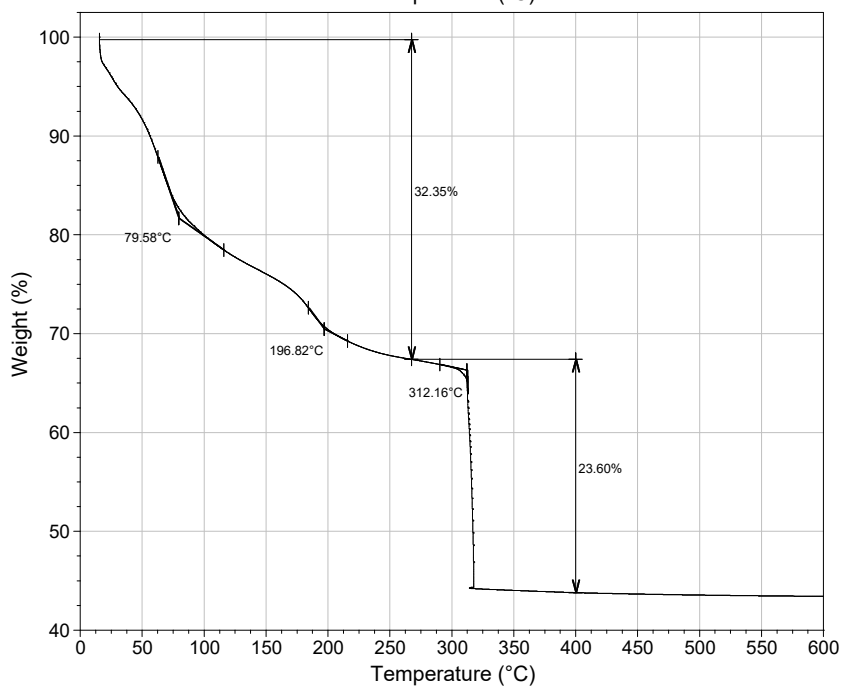


Figure B.9: Thermogram of CoHCC as-synthesized (continuous line) and ozonized (dashed line).

APPENDIX B. POST-SYNTHESIS MODIFICATION WITH OZONE



MnHCC



CoHCC

Figure B.10: TGA for MnHCCOz and CoHCCOz, saturated with methanol.

# Appendix C

## Complementary results: Photoelectron spectroscopy

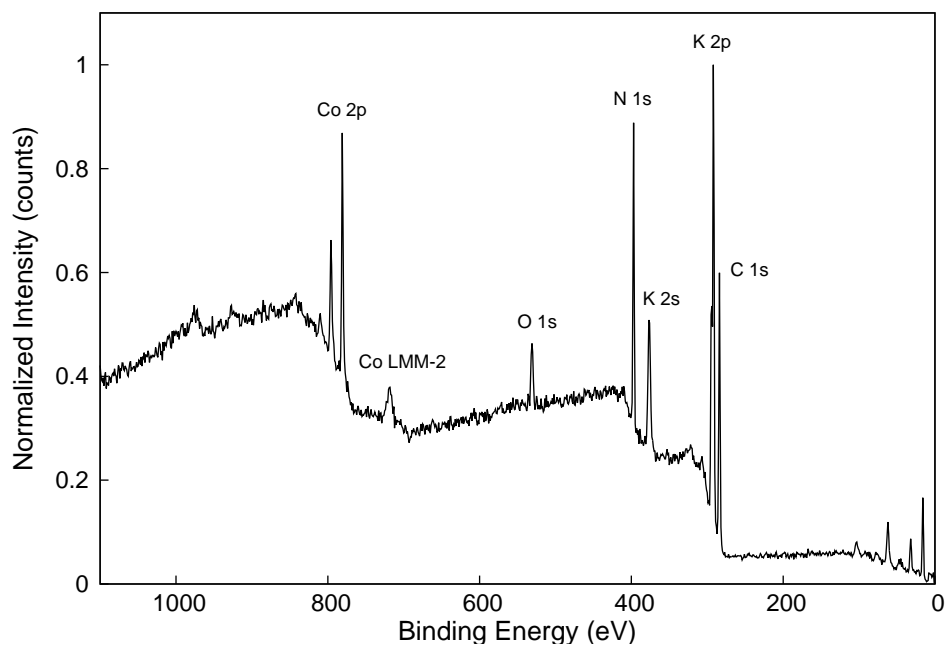


Figure C.1: Normalized survey spectra for  $K_3[Co(CN)_6]$ . The core level Co 2p was taken as a reference to adjust the binding energy positions.

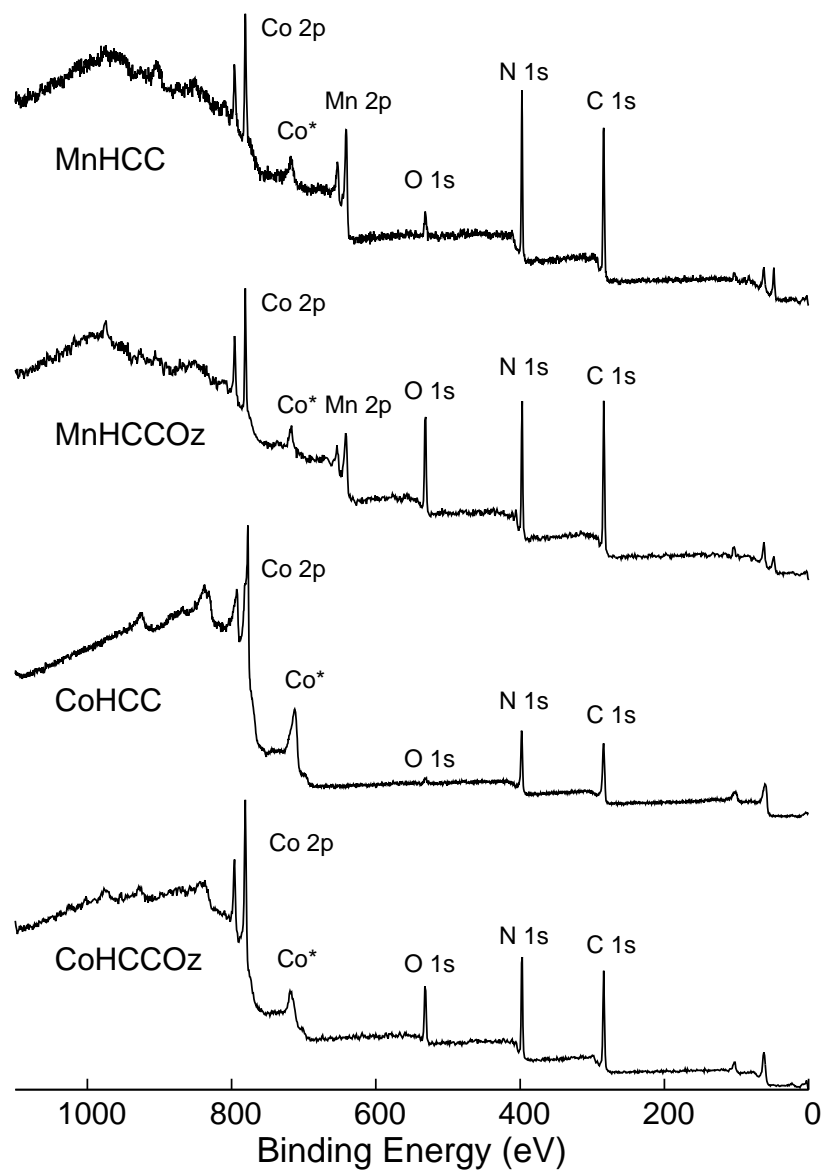


Figure C.2: Normalized XPS survey spectra for MnHCC and CoHCC before and after being ozonized. The peak Co\* states for Co LMM-2 emissions.

---

APPENDIX C. PHOTOELECTRON SPECTROSCOPY

---

Table C.1: Elemental composition of the experimental samples. This composition (Elemental %) was evaluated from core levels high resolution spectra, using the atomic sensitivity factors taken from reference [139]. The third column is the experimental number of atoms of each element per formula unit (Atoms pFU). The fourth column (Expected Atoms pFU) is the expected number of atoms of each element according to the samples stoichiometry. The fifth column ( $\delta_{rel}$ ) is the percentage deviation from the stoichiometric composition.

	Elemental %	Atoms pFU	Expected Atoms pFU	$\delta_{rel}$ %
MnHCC				
Co	7.6	1.8	2	10
Mn	12.4	3.0	3	0
N	25.0	6.0	12	50
C	50.9	12.3	12	2
O	4.2	1.0	-	-
MnHCCOz				
Co	5.6	2.2	2	10
Mn	7.5	3	3	0
N	28.0	11.2	12	7
C	47.6	19.4	12	62
O	11.2	4.5	-	-
CoHCC				
Co	14.9	5	5	0
N	25.7	8.6	12	28
C	56.6	19.0	12	58
O	2.8	0.9	-	-
CoHCCOz				
Co	12.6	5	5	0
N	31.1	12.3	12	2
C	43.0	17.1	12	42
O	13.3	5.3	-	-

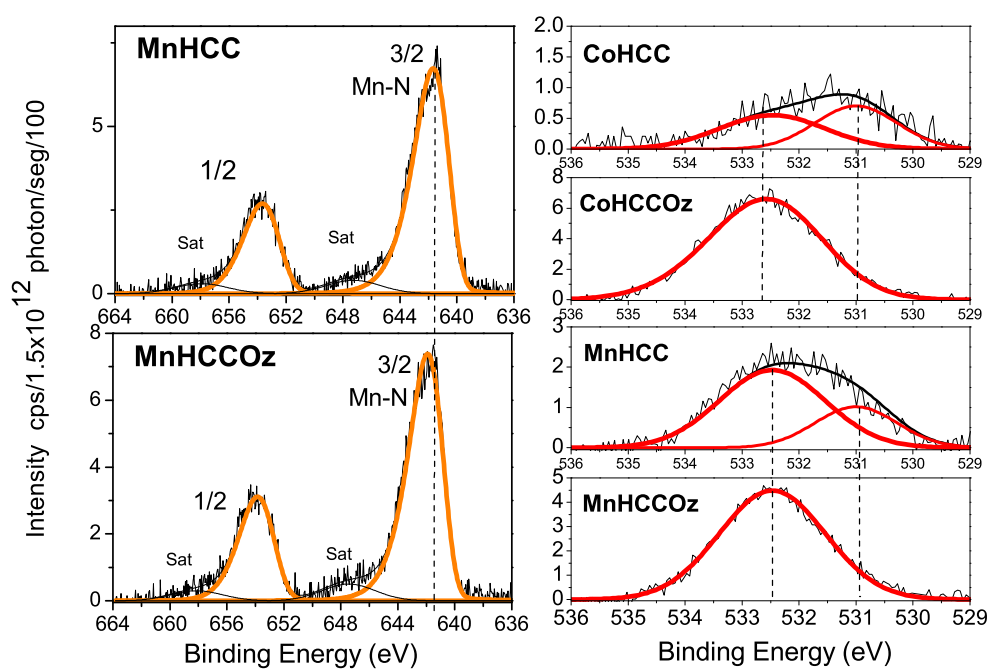


Figure C.3: The XPS deconvolution for Mn 2p and O 2p core levels in MnHCC and CoHCC as synthesized and ozonized samples.

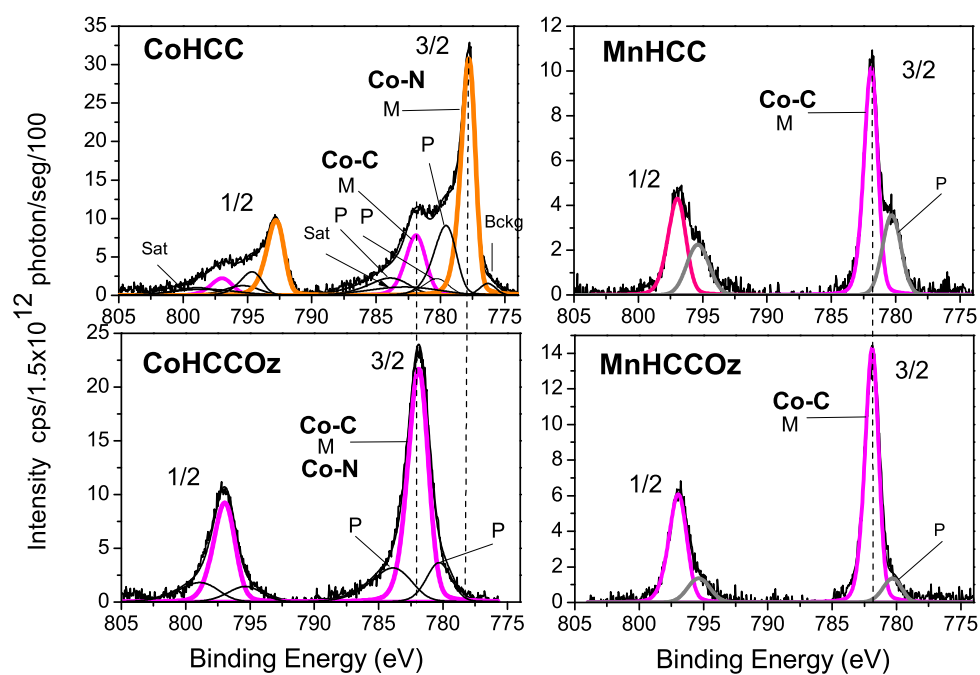


Figure C.4: The XPS deconvolution for Co 2p core levels in MnHCC and CoHCC as synthesized and ozonized samples

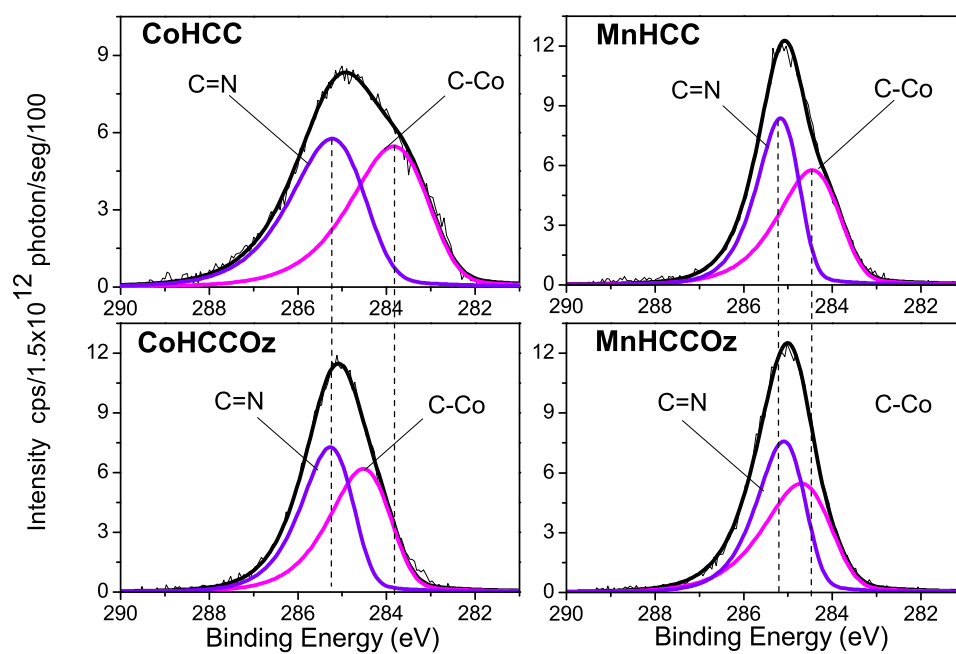


Figure C.5: The XPS deconvolution for C 1p core levels in MnHCC and CoHCC as synthesized and ozonized samples

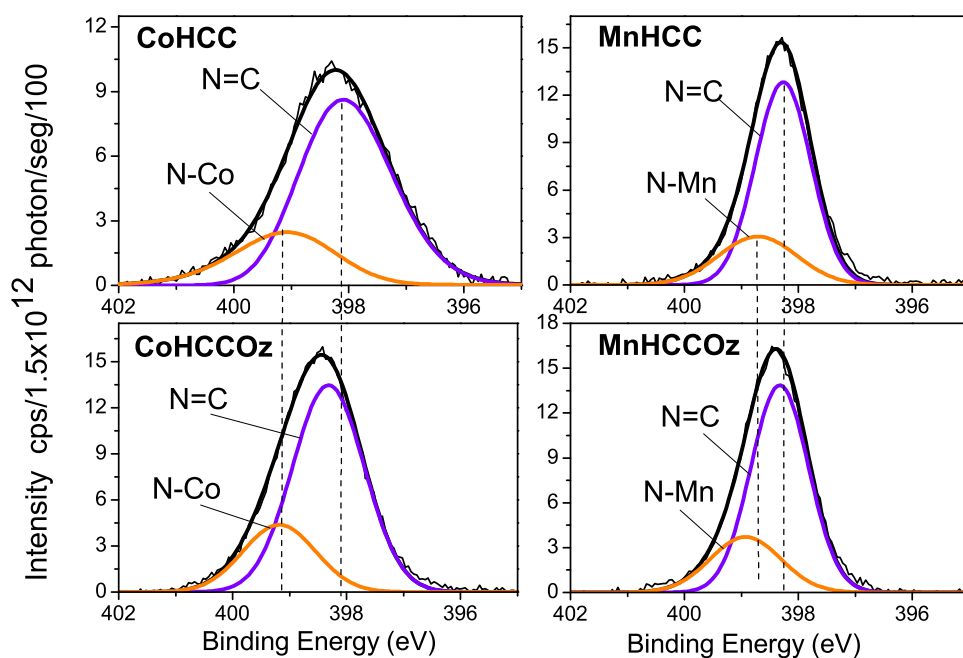


Figure C.6: The XPS deconvolution for N 1s core levels in MnHCC and CoHCC as synthesized and ozonized samples